Optical Thickness Retrievals of Subtropical Cirrus and Arctic Stratus from Ground-Based and Airborne Radiance Observations Using Imaging Spectrometers

Der Fakultät für Physik und Geowissenschaften

der Universität Leipzig

eingereichte

DISSERTATION

zur Erlangung des akademischen Grades

Doktor der Naturwissenschaften
(Dr. rer. nat.)

vorgelegt

von **Dipl.-Met. Michael Schäfer**

geboren am 27.02.1985 in Schönebeck/ Elbe, Sachsen-Anhalt

Leipzig, den 22.02.2016

Bibliographische Beschreibung:

Schäfer, Michael

Optical Thickness Retrievals of Subtropical Cirrus and Arctic Stratus from Ground-Based and Airborne Radiance Observations Using Imaging Spectrometers

Universität Leipzig, Dissertation

121 S., 127 Lit., 49 Abb., 16 Tab.

Referat:

Im folgenden wird die Entwicklung und Anwendung neuer Ableitungsverfahren von Wolkenparametern, basierend auf bodengebundener und flugzeuggetragener spektraler Strahldichtemessungen über heterogenen Untergründen, vorgestellt und das Fernerkundungspotential abbildender Spektrometer evaluiert. Die spektralen Strahldichtefelder wurden während zweier internationaler Feldkampagnen im sichtbaren Wellenlängenbereich (400–970 nm) mit hoher räumlich Auflösung (< 10 m) gemessen. Bodengebundene Messungen wurden genutzt, um hohe Eiswolken zu beobachten und flugzeuggetragenen um arktischen Stratus zu beobachten. Aus den Messungen werden räumlich hochaufgelöste wolkenoptische Dicken abgeleitet und anschließend horizontale Wolkeninhomogenitäten untersucht. Die Ableitung der wolkenoptischen Dicke birgt je nach Messkonfiguration verschiedene Unsicherheiten. Eine Reduzierung der Unsicherheiten wird durch die Vorgabe einer Eiskristallform zur Verbesserung der Ableitung der optischen Dicke hoher Eiswolken erreicht. Diese werden unabhängig aus den winkelabhängigen, in das gemessene Strahldichtefeld eingeprägten Eigenschaften der Streuphasenfunktion, abgeleitet. Bei Vernachlässigung dieser Information und Wahl der falschen Eiskristallform, treten Fehler in der abgeleiteten optischen Dicke von bis zu 90 % auf. Bei der Fernerkundung von arktischem Stratus beeinflusst die sehr variable Bodenalbedo die Genauigkeit der Ableitung der optischen Dicke. Beim Übergang von Meereis zu Wasser, findet die Abnahme der reflektierten Strahldichte im bewölktem Fall nicht direkt über der Eiskante, sondern horizontal geglättet statt. Allgemein reduzieren Wolken die reflektierte Strahldichte über Eisflächen nahe Wasser, während sie über dem Wasser erhöht wird. Dies führt zur Überschätzung der wolkenoptischen Dicke über Wasserflächen nahe Eiskanten von bis zu 90 %. Dieser Effekt wird mit Hilfe von Beobachtungen und dreidimensionalen Strahlungstransferrechnungen untersucht und es wird gezeigt, dass sein Einfluss noch bis zu 2200 m Entfernung zur Eiskante wirkt (für Meeresalbedo 0.042 und Meereisalbedo 0.91 bei 645 nm Wellenlänge) und von den makrophysikalischen Wolken- und Meereiseigenschaften abhängt.

Die abgeleiteten Felder der optischen Dicke werden statistisch ausgewertet, um die Inhomogeneität der Wolken zu charakterisieren. Autokorrelationsfunktionen und Leistungsdichtespektren zeigen, dass Inhomogenitäten von Wolken mit vorranging richtungsabhängiger Struktur nicht mit einem allgemeingültigen Parameter beschrieben werden können. Es sind Inhomogenitätsmaße entlang und entgegen der jeweiligen Wolkenstrukturen nötig, um Fehler von bis zu 85 % zu vermeiden.

Bibliographic Description:

Abstract:

The development and application of new cloud retrieval methods from ground–based and airborne measurements of spectral radiance fields above heteorogeneous surfaces is introduced. The potential of imaging spectrometers in remote–sensing applications is evaluated. The analyzed spectral radiance fields were measured during two international field campaigns in the visible wavelength range (400–970 nm) with high spatial (< 10 m) resolution. Form ground–based measurements, high ice clouds were observed and from airborne measurements Arctic stratus. From the measurements, cloud optical thickness is retrieved with high spatial resolution and the horizontal cloud inhomogeneities are investigated. Depending on the measurement configuration, different uncertainties arise for the retrieval of the cloud optical thickness. A reduction of those uncertainties is derived by a specification of the ice crystal shape to improve the retrieval of the optical thickness of high ice clouds. The ice crystal shape is obtained independently from the angular information of the scattering phase function features, imprinted in the radiance fields. A performed sensitivity study reveals uncertainties of up to 90 %, when neglecting this information and applying a wrong crystal shape to the retrieval. For remote-sensing of Arctic stratus, the highly variable surface albedo influences the accuracy of the cloud optical thickness retrieval. In cloudy cases the transition of reflected radiance from open water to sea ice is not instantaneous but horizontally smoothed. In general, clouds reduce the reflected radiance above bright surfaces in the vicinity of open water, while it is enhanced above open sea. This results in an overestimation of to up to 90 % in retrievals of the optical thickness. This effect is investigated. Using observations and three-dimensional radiative transfer simulations, this effect is quantified to range to up to 2200 m distance to the sea-ice edge (for dark-ocean albedo of $\alpha_{\text{water}} = 0.042$ and sea-ice albedo of $\alpha_{\text{ice}} = 0.91$ at 645 nm wavelength) and to depend on macrophysical cloud and sea-ice properties.

The retrieved fields of cloud optical thickness are statistically investigated. Auto–correlation functions and power spectral density analysis reveal that in case of clouds with prevailing directional cloud structures, cloud inhomogeneities cannot be described by a universally valid parameter. They have to be defined along and across the prevailing cloud structures to avoid uncertainties up to 85 %.

Contents

1 Motivation and Objectives

The globally and annually averaged cloud cover is about $70\,\%$ (Rossow and Schiffer, 1999). Therefore, clouds need to be considered as an important regulator of the Earth's radiation budget (Loeb et al., 2009). Clouds scatter and absorb solar radiation in the wavelength range from 0.2 to $5\,\mu\text{m}$; they emit and absorb terrestrial radiation in the wavelength range from 5 to $100\,\mu\text{m}$. Therefore, the interaction of clouds with radiation needs to be investigated. Although clouds have been studied for several decades, they still pose many challenges in terms of their observation and representation in weather and climate models (Shonk et al., 2011). The latest report of the Intergovernmental Panel on Climate Change (IPCC, 2013) classifies cloud effects as one of the largest uncertainties in climate simulations, significantly contributing to uncertainties in the determination of the Earth's energy budget (Stocker et al., 2013). The large uncertainties arise from an insufficient representation of complex cloud structures (cloud inhomogeneities) and from cloud-radiation feedback processes that control the cloud evolution (Stephens, 2005; Shonk et al., 2011). Therefore, the representation of cloud inhomogeneities needs to be addressed (Shonk et al., 2011), as changing cloud properties have an important effect on the interaction of clouds with radiation (Slingo, 1990).

Serious limitations in the quantification of cloud optical properties such as the cloud optical thickness (τ) exist. High ice clouds (cirrus) and Arctic stratus reveal significant horizontal inhomogeneities of different origin and horizontal scale. Both cloud types can either warm or cool the climate system, depending on their optical and microphysical properties and the meteorological conditions. For example, Choi and Ho (2006) reported for tropical regions a warming net radiative effect of cirrus with a cirrus optical thickness (τ_{ci}) of less than 10, but a cooling effect for $\tau_{\text{ci}} > 10$. For Arctic stratus, Wendisch et al. (2013) showed that for low surface albedo (α_{surf}) and low solar zenith angle (θ_0), the cloud cools the sub-cloud layer. With increasing α_{surf} and increasing θ_0, the net cooling effect of the low–level cloud turns into a net warming (for $\alpha_{\text{surf}}(\theta_0 = 80°) > 0.15$, $\alpha_{\text{surf}}(\theta_0 = 60°) > 0.7$, for a low–level cloud with an optical thickness of $\tau_{\text{st}} = 10$ in a subarctic summer atmosphere). Thus, the radiative forcing of cirrus and Arctic stratus depends significantly on the cloud optical thickness and the surface albedo.

1.1 The Advantage of High Spatial Resolution

Clouds exhibit significant horizontal and vertical inhomogeneity. However, in most climate simulations and remote-sensing applications they are assumed as plane-parallel with homogeneous (fixed) particle size and shape (Francis et al., 1998; Iwabuchi and Hayasaka, 2002; Garrett et al., 2003). It is well-known that the traditional use of plane-parallel and

homogeneous clouds introduces biases into the modeled radiation budget (Shonk et al., 2011). Several studies investigated the influence of a plane-parallel assumption on cloud retrievals (e.g. Cahalan, 1994; Loeb and Davies, 1996; Marshak et al., 1998; Zinner et al., 2006; Varnai and Marshak, 2007). They found that the model biases are related to the degree of horizontal photon transport, which is ignored in radiative transfer schemes used in **g**eneral **c**irculation **m**odels (GCM). Multiple scattering due to three-dimensional (3D) microphysical cloud structures smooth the sampled radiation field. On small scales, this limits the accuracy of the **i**ndependent **p**ixel **a**pproximations (IPA) results. Cahalan (1994) and Marshak et al. (1995) revealed discrepancies for individual pixel radiances exceeding 50 %. For the top-of-atmosphere cloud radiative forcing (solar and terrestrial), Shonk and Hogan (2008) reported an overestimation of about 8 %.

3D Monte Carlo radiative transfer simulations account for the horizontal photon transport. However, they are costly in terms of computer time and memory (Huang and Liu, 2014). This renders Monte Carlo radiative transfer simulations as inappropriate for the application in operational or global models. Other approaches introduce **c**loud **o**verlap **s**chemes (COS), such as the maximum-random COS (Geleyn and Hollingsworth, 1979), the exponential-random COS (Hogan and Illingworth, 2000), or Triplecloud COS (Shonk and Hogan, 2008). Improvements compared to the use of plane-parallel homogeneous clouds were achieved, but results are still not as accurate as those derived by Monte Carlo simulations or measurements with high spatial resolution. Thus, since many cloud processes occur on small horizontal scales (e.g. cloud particle formation, turbulence), the uncertainties inherent in one-dimensional (1D) simulations still have to be improved. Therefore, Huang and Liu (2014) introduced an approach, which uses spatial auto-correlation functions of cloud extinction coefficients to physically capture the net effects of subgrid cloud interactions with radiation. With several orders less computational time, this approach is able to reproduce 3D Monte Carlo radiative transfer simulations with sufficient accuracy. However, the method requires spatial auto-correlation functions of cloud extinction coefficients with high spatial resolution, which substantiates the need for measurements of comparable resolution.

GCM or numerical weather forecast models such as that from the **E**uropean **C**entre for **M**edium-Range **W**eather **F**orecasts (ECMWF) require sub-grid scale parameterizations of e.g. cloud structures, **l**iquid **w**ater **c**ontent (LWC), and/or **i**ce **w**ater **c**ontent (IWC) distribution (Huang and Liu, 2014). Cloud structures including inhomogeneities show spatial features down to distances below the meter scale. Therefore, measurements with high spatial and temporal resolution have to be applied to obtain the parameterizations. The required measurements include cloud altitude (temperature), its geometry (vertical and horizontal extent), and cloud microphysical properties (e.g. LWC, IWC, droplet size, ice crystal size and shape distributions).

As proposed by Marshak et al. (1995), Oreopoulos et al. (2000), or Schroeder (2004), horizontal cloud inhomogeneities are usually investigated by scale analysis of cloud-top-reflectances. However, radiance measurements include the information of the scattering phase function, imprinted in the measured radiance field. To avoid artifacts in the scale analysis resulting from such features, parameters that account for them (e.g. τ) have to be analyzed.

1.2 Observation of Cloud Inhomogenieties by Remote Sensing

The necessary cloud parameters to investigate cloud inhomogeneities and to validate/improve models can be obtained by in situ measurements or by remote–sensing. In situ measurements benefit from high spatial and temporal resolution, but are restricted to small parts of the cloud only. Satellite–based remote–sensing covers large horizontal areas but often does not have sufficient vertical and horizontal resolution (Tab. 1.1); e.g. operational imagers, such as the **Mod**erate-Resolution **I**maging **S**pectroradiometer (MODIS, 250-1000 m, King et al., 2003) or the **A**dvanced **V**ery **H**igh **R**esolution **R**adiometers (AVHRR, 1 km resolution, Cracknell, 1997). Horizontal cloud structures smaller than the resolution cannot be resolved. An improvement of this situation is achieved by coupling satellite observations with ground–based/airborne in situ/remote–sensing measurements with increased temporal and spatial resolution. This combination is suitable to validate satellite products and to improve parameterizations, including cloud-radiative effects generated from horizontal cloud inhomogeneities. Frequently applied instruments for such applications are nadir-viewing point spectrometers such as the **S**olar **S**pectral **F**lux **R**adiometers (SSFR, Pilewskie et al., 2003) or the **S**pectral **M**odular **A**irborne **R**adiation measurement sys**T**em (SMART, Wendisch et al., 2001). These instruments provide radiation measurements with high spatial resolution (along track) within a field of view (FOV) of $< 2°$. Pointing spectrometers are supplemented by imaging spectrometers with usually lower spectral resolution. They usually measure in a FOV larger than 30°. Examples of imaging spectrometers are the **C**ompact **A**irborne **S**pectrographic **I**mager (CASI, Anger et al., 1994), the **spec**trometer of the **M**unich **A**erosol **C**loud **S**canner (specMACS, Ewald et al., 2015) or the imaging spectrometer AisaEAGLE applied for the current thesis.

Table 1.1: Category of remote-sensing techniques, instruments, and spatial resolution/coverage. The spectral instrumental characteristics are indicated by index B (bands) and M (multi-spectral).

Category	Instruments	Pixel Size (m)	Coverage
Imaging Spectrometer	CASI[M], specMACS[M], AisaEAGLE[M]	< 15	Local
Point Spectrometer	SSFR[M], SMART[M]	< 100	Local
Operational Imager	MODIS[B], AVHRR[B]	250-1000	Global

Figure 1.1 illustrates a cloud as observed from above with different spatial resolutions. It shows the advantage of high resolving imaging spectrometers (Fig. 1.1a) compared to nadir-viewing point spectrometers (Fig. 1.1b) and to operational imagers carried by satellites (Fig. 1.1c and d). Detailed investigations of horizontal cloud inhomogeneities are not feasible from MODIS and AVHRR measurements. From Fig. 1.1b, cloud structures are derived with high spatial resolution along track of the measurements, but due to the small FOV, 2D distributions of cloud structures are not represented adequately. From imaging spectrometers (Fig. 1.1a), both high spatial resolution and large 2D coverage of the investigated cloud can be resolved. Thus, imaging spectrometers are very useful to investigate small-scale cloud inhomogeneities over large areas. For example, using airborne remote-sensing spectral imaging sensors during the international field campaign SoRPIC (**So**lar **R**adiation and **P**hase dis-
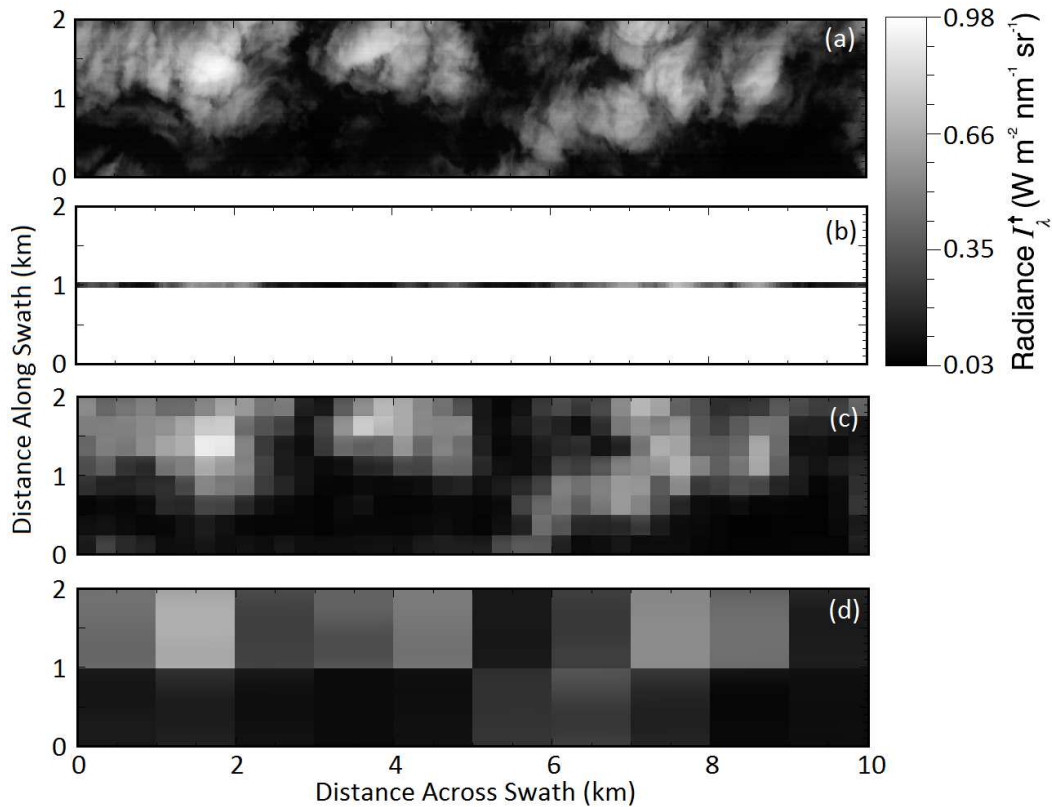
Figure 1.1: Radiance at 645 nm wavelength of a cloud scene, as observed with different ground-pixel size resolution of **(a)** 5 m (CASI, specMACS, AisaEAGLE), **(b)** 50 m (SSFR, SMART), **(c)** 250 m (MODIS), and **(d)** 1 km (MODIS, AVHRR).

crimination of Arct**I**c **C**louds), Bierwirth et al. (2013) showed that τ can be retrieved with a spatial resolution below 5 m. An even larger FOV can be achieved with commercial digital cameras (Ehrlich et al., 2012). However, they mostly provide measurements in three spectral wavelength bands only (red, green, blue; RGB). Therefore, they lack of necessary spectral resolution, which is needed to retrieve cloud parameters such as τ or r_{eff}.

1.3 Complications of Retrievals of Cirrus Properties

Satellite-based cirrus cloud climatology such as reported by Sassen and Campbell (2001), Sassen and Benson (2001), and Sassen and Comstock (2001) include cloud cover, cirrus optical thickness and crystal effective radius. Each change in one of those parameters modifies the magnitude of their radiative forcing. For example, current global circulation models assume a standard value of 25 µm for the ice crystal effective radius. For slightly smaller crystals, the cirrus would have a stronger cooling effect (Garrett et al., 2003). Furthermore, cirrus often shows spatial and temporal variability and is optically thin. This complicates the detection of cirrus by common remote-sensing techniques. The applicability of their data is limited by 3D radiative effects, but also by the number of wavelength bands and spatial resolution of the sensor. Numerous studies investigated cirrus radiative-effects from satellite

and ground–based observations as well as by means of numerical simulations (Liou, 1986; Lynch et al., 2002; Yang et al., 2007; Baran, 2012).

For optical thickness retrieval, the microphysical composition of the cloud (non-spherical ice crystals) adds a crucial complication. The representation of the scattering properties of cloud droplets is well known and is described by Mie-Theory (Mie, 1908; Bohren and Huffman, 1998). However, optical properties of ice crystals such as the extinction coefficient, scattering phase function, and single–scattering albedo differ significantly from those of liquid water droplets (Takano and Liou, 1989; Fu and Liou, 1993; Macke, 1993). The crystal shape can change the cloud radiative properties substantially, which may cause biases in satellite retrievals (based on reflected radiance, Eichler et al., 2009) and radiative energy budget estimates (related to irradiance, Wendisch et al., 2005, 2007). For the retrieval of τ_{ci} assumptions about the crystal shape and the corresponding scattering properties are made. However, the ice crystal shape is an important parameter influencing the radiative properties of ice clouds (e.g., Macke et al., 1998; Wendisch et al., 2005, 2007; Eichler et al., 2009). Eichler et al. (2009) showed that these assumptions can add an uncertainty of up to 70 % and 20 % in retrievals of τ and r_{eff}, respectively. With regard to cirrus solar radiative forcing, Wendisch et al. (2005) revealed uncertainties of up to 26 %. Progress in the parameterization of optical properties of ice crystals in GCM has been made (e.g., Kristjansson et al., 2000; Edwards et al., 2007) using an ensemble of ice crystal shapes including roughened surfaces. Recent studies by Baum et al. (2005a,b, 2007); Yang et al. (2005, 2012) and Yi et al. (2013) emphasize the parameterization of ice particle surface roughness, which results in a reduction of the asymmetry factor compared to smooth particles of the same size. Although progress is reported, difficulties in retrievals of cirrus properties are still significant, especially for optically thin cirrus (Comstock et al., 2007).

A method to determine the ice crystal shape was proposed by Chepfer et al. (2002). It is based on multiangle satellite measurements of cloud-top-reflectance and polarized bidirectional radiances in the visible wavelength range (Chepfer et al., 2001). Another method, based on imaging spectrometry was proposed by McFarlane and Marchand (2008). They developed a best-fit ice crystal scattering model that uses angular dependent measurements from coincident **M**ulti-angle **I**maging **S**pectro**R**adiometer (MISR) and MODIS reflectances. Sensitivity to particle shape is provided by the multi-angle information from MISR. McFarlane and Marchand (2008) were able to distinguish between ice crystal habits such as aggregates and plates.

To check the cirrus retrieval algorithms airborne versions of spectroradiometers above cirrus are applied, such as the **MODIS A**irborne **S**imulator (MAS). With extensive microphysical and solar radiation instruments as well as radiative transfer simulations, Schmidt et al. (2007) and Eichler et al. (2009) investigated the differences between retrieved and measured microphysical cloud properties. Schmidt et al. (2007) revealed gaps between the retrieved effective radius from MAS and simultaneous in situ measurements. This disagreement has not been resolved yet, partly because it has been difficult to collocate remote sensing above the clouds and concurrent in-cloud microphysical measurements. However, such observations are important to link satellite cloud observations of coarse resolution to spatially highly resolved measurements of cloud properties. Such experiments are rare, partly because instruments like

MAS are complex and expensive and are not available for frequent cloud observations. However, progress in performing collocated in situ and radiation measurements is reported. For example, Werner et al. (2014) successfully investigated shallow cumuli from collocated microphysical and remote-sensing measurements using helicopter-towed measurement platforms. Furthermore, Finger et al. (2015) introduced a measurement technique (related to spectral optical layer properties), based on an aircraft-towed measurement platform. Such towed platforms can also be used to validate satellite retrievals of coarse resolution. Finger et al. (2015) showed that such measurements are complex. The high flight speed requires a rope of several kilometers length to allocate the measurement platform a few hundred meter below the aircraft. As an alternative, measurements with ground-based imaging spectrometers provide information on cirrus inhomogeneities in terms of radiance, cirrus optical thickness, and cirrus crystal shape.

1.4 Current Limitations for Arctic Stratus Cloud Retrieval

Sea ice is characterized by a heterogeneous horizontal distribution. It has irregular surfaces and is usually broken into pieces, called floes (Rothrock and Thorndike, 1984). Openings in the ice surface (cracks, leads, and polynias) are common especially in the transition zone between sea ice and open water, accompanied by fields of scattered ice floes. The surface albedo contrast in such areas is extreme and partly occurs on small horizontal scales in a range of less than tenth of meters. For visible wavelengths the surface albedo of open water is low (0.042 at 645 nm; Bowker et al., 1985), while that of ice-covered ocean is high (0.91 at 645 nm; Bowker et al., 1985). These differences decrease in the near-infrared wavelength range ($\alpha_{\text{water}} = 0.01$ and $\alpha_{\text{snow}} = 0.04$ at 1.6 µm wavelength; Bowker et al., 1985).

Using AVHRR data from the polar-orbiting satellites NOAA-10 and NOAA-11 (**N**ational **O**ceanic and **A**tmospheric **A**dministration), Lindsay and Rothrock (1994) analyzed the albedo of 145 different 200 km² cells in the Arctic. The mean values for the cloud-free surface of individual cells ranged from 0.18 to 0.91 and were highly variable at monthly and annual time scales. The application of the retrieval by Bierwirth et al. (2013) is restricted to areas of open water. A variable Arctic surface albedo as quantified by Lindsay and Rothrock (1994) complicates the retrieval of cloud microphysical and optical properties using only visible wavelengths (Platnick, 2001; Platnick et al., 2004, 2003; Krijger et al., 2011). To overcome this limitation, near-infrared channels are used in addition in the retrieval algorithms. For MODIS the 1.6 µm band reflectance is applied as a surrogate for the traditional non-absorbing band in conjunction with a stronger absorbing 2.1 or 3.7 µm band (Platnick, 2001; Platnick et al., 2004, 2003). However, an accurate separation between sea ice and open water needs to be performed before the retrieval algorithms are applied. Operational algorithms (e.g. for MODIS), use NOAA's microwave-derived daily 0.25° **N**ear Real-Time **I**ce and **S**now **E**xtent (NISE; Armstrong and Vazquez-Cuervo, 2001; Platnick et al., 2003) to identify snow- or ice-covered scenes. For the typical scale of ice floes this pixel size is not sufficient.

Even when ice and ice-free areas are perfectly separated, 3D radiative effects can affect the cloud retrieval over ice-free pixels close to the ice edge. Lyapustin (2001) and

Lyapustin and Kaufman (2001) quantified the impact of the contrast of the surface albedo between open sea and adjacent sea-ice or snow on the retrieval of Arctic cloud properties. Adjacency effects are found to reduce the apparent surface contrast by decreasing the top-of-the-atmosphere reflectivity γ_λ over bright pixels and increasing the brightness of dark pixels, which becomes important for land remote-sensing applications developed for usage with both dark or bright targets.

Surface 3D radiative effects interfere with cloud 3D radiative effects due to cloud inhomogeneities. In the case of Arctic stratus, the individual cloud 3D effects are of minor importance. For a solar zenith angle $\theta_0 = 45°$, Zinner et al. (2010) found that the remote-sensing of stratocumulus was not biased by 3D effects, while that of scattered cumulus was sensitive to horizontal heterogeneities. This leads to the assumption that retrievals of cloud microphysical and optical properties can be treated by 1D simulations if the distance to ice-open water boundaries is sufficiently large. However, measurements in Arctic regions are mostly performed for solar zenith angles larger than 45°. In such cases, 3D radiative effects generated by the cloud structures become important. Using plane-parallel 1D simulations of clouds, Loeb and Davies (1996) stated that τ shows a systematic shift towards larger values with increasing θ_0. This dependence is weak ($\leq 10\%$) for thin clouds ($\tau \leq 6$) and $\theta_0 \leq 63°$. Grosvenor and Wood (2014) confirmed this statement. They investigated MODIS satellite retrieval biases of τ and reported that τ is almost constant between $\theta_0 = 50°$ and $\theta_0 \approx 65$–$70°$, but then increases rapidly by over 70% between the lowest and highest θ_0.

Jäkel et al. (2013) quantified the effect of local surface-albedo heterogeneity and aerosol parameters on the retrieved area-averaged surface albedo from airborne upward and downward irradiance measurements. For adjacent land and sea, Jäkel et al. (2013) defined a critical distance at which the retrieved area-averaged surface albedo deviates by 10% from the given local surface albedo. It was found that this critical distance ranges in the order of $2.4\,\mathrm{km}$ for a flight altitude of $2\,\mathrm{km}$ and is larger for albedo fields with higher surface albedo contrast. In the case of clouds with an optical thickness larger than that of aerosol particles, this effect is expected to increase significantly.

1.5 Objectives

In the following chapters the development and application of new cloud retrieval methods based on imaging spectrometer measurements from the ground and using airborne carriers is introduced. The potential of imaging spectrometers in remote–sensing applications is evaluated and demonstrated by two applications. The analyzed data are obtained from imaging spectrometer measurements in the visible wavelength range (400–970 nm) with high spatial ($< 10\,\mathrm{m}$) resolution (AisaEAGLE, Hanus et al., 2008; Schäfer et al., 2013, 2015). The data were collected during the two international field campaigns **C**louds, **A**erosol, **R**adiation, and tu**R**bulence in the trade w**I**nd regime over **BA**rbados (CARRIBA) on Barbados in April 2011, and **VER**tical **D**istribution of **I**ce in Arctic clouds (VERDI) in Inuvik, Canada in May 2012.

The data are used to retrieve fields of highly resolved cloud optical thickness to investigate the horizontal distribution of cloud inhomogeneities. Two different configurations have been applied to derive the fields of τ:

- For CARRIBA, ground-based measured downward solar radiance transmitted through cirrus, and

- For VERDI, airborne measured upward solar radiance reflected by Arctic stratus.

The investigation of the retrieved fields of τ with regard to the horizontal distribution of cloud inhomogeneities is performed by:

- A statistical evaluation using common inhomogeneity parameters, and

- A characterization of the spatial distribution using auto–correlation functions and power spectral density analysis.

Chapter 2 introduces the terminology applied in this thesis. In Chapter 3 the applied instrument (AisaEAGLE) is characterized. Its calibration and data evaluation procedures are described and exemplified. Chapter 4 introduces a new method to retrieve the cirrus optical thickness from spectral radiance data, which uses angular sampling of the phase function to obtain information about the particle shape. In Chapter 5, airborne observations of the spectral reflectivity of Arctic stratus are presented. A robust algorithm separating sea-ice and open-water surfaces under cloud cover is introduced and applied to the measurements. Observations and simulations of the 3D radiative effects are investigated with regard to their influence on 1D retrievals of τ and r_{eff}. In Chapter 6, the derived fields of τ are investigated regarding their inhomogeneity. Conclusions and an outlook are given in Chapter 7.

2 Definitions

This chapter introduces the nomenclature applied in this thesis. It introduces general radiometric quantities (Sect. 2.1) and cloud optical properties (Sect. 2.2). In Sect. 2.3 the radiative transfer equation (RTE) is described and in Sect. 2.4 the cloud microphysical properties. The definitions follow the textbooks of Bohren and Clothiaux (2006), Petty (2006), and Wendisch and Yang (2012).

2.1 Radiative Quantities

The spectral radiant energy flux Φ_λ characterizes the radiant energy E_{rad} that passes through an infinitesimal area element d^2A within a given time interval $t + \mathrm{d}t$ for a selected wavelength range $\lambda + \mathrm{d}\lambda$. Therefore, Φ_λ is defined by:

$$\Phi_\lambda = \frac{\mathrm{d}^2 E_{\mathrm{rad}}}{\mathrm{d}t\,\mathrm{d}\lambda}. \tag{2.1}$$

$\Phi_\lambda(t)$ carries the units $\mathrm{J\,s^{-1}\,nm^{-1}}$. It defines the power of radiant energy at a given time t. $\Phi_\lambda(t)$ can be expressed in the unit of $\mathrm{W\,nm^{-1}}$. Normalizing Φ_λ to the corresponding area element d^2A results in the spectral radiant energy flux density F_λ:

$$F_\lambda = \frac{\mathrm{d}^2 \Phi_\lambda}{\mathrm{d}^2 A} = \frac{\mathrm{d}^4 E_{\mathrm{rad}}}{\mathrm{d}^2 A\,\mathrm{d}t\,\mathrm{d}\lambda}. \tag{2.2}$$

F_λ is also called spectral irradiance and is given in units of $\mathrm{W\,m^{-2}\,nm^{-1}}$. F_λ describes the spectral radiant energy flux, which passes trough an unit area from all directions of a hemisphere. For atmospheric applications, the area element d^2A is considered horizontal; the orientation of the unit vector is perpendicular to d^2A and points in zenith direction.

Pointing into the direction of propagation $\widehat{s}$, E_{rad} within a solid angle element $\mathrm{d}^2\Omega$ is quantified by the spectral radiance $I_\lambda(\widehat{s})$:

$$I_\lambda(\widehat{s}) = \frac{\mathrm{d}^4 \Phi_\lambda}{\cos\theta\,\mathrm{d}^2 A\,\mathrm{d}^2\Omega} = \frac{\mathrm{d}^6 E_{\mathrm{rad}}}{\mathrm{d}t\,\mathrm{d}\lambda\,\cos\theta\,\mathrm{d}^2 A\,\mathrm{d}^2\Omega}. \tag{2.3}$$

The unit of $I_\lambda(\widehat{s})$ is $\mathrm{W\,m^{-2}\,nm^{-1}\,sr^{-1}}$. With regard to the position of the Sun and the direction $\widehat{s}$, the radiance is defined as upward $I_\lambda^\uparrow(\widehat{s})$ or downward $I_\lambda^\downarrow(\widehat{s})$. Figure 2.1 illustrates the geometry for the definition of $I_\lambda(\widehat{s})$.

In Fig. 2.1, the definition of a solid angle element $\mathrm{d}^2\Omega$ is used (solid angle is related to regular angle as area is related to length), which can be described with the directional angles
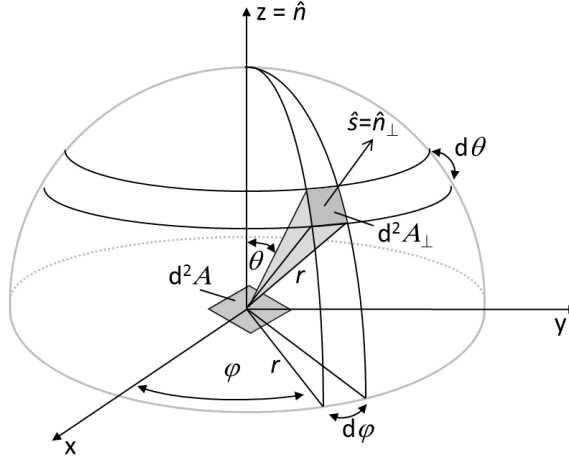
Figure 2.1: Illustration of the definition of radiances using a solid angle element described by the zenith angle θ and azimuth angle φ.

θ (zenith angle) and φ (azimuth angle). The area on the sphere marked by the depicted sector in Fig. 2.1 is defined by:

$$\mathrm{d}^2 A_\perp = r^2 \cdot \sin\theta \, \mathrm{d}\theta \, \mathrm{d}\varphi. \tag{2.4}$$

Using this equation and following the definition of a solid angle, the solid-angle element illustrated by the pyramid in Fig. 2.1 and observed from the origin of the coordinate system is given by:

$$\mathrm{d}^2\Omega = \frac{\mathrm{d}^2 A_\perp}{r^2} = \sin\theta \, \mathrm{d}\theta \, \mathrm{d}\varphi. \tag{2.5}$$

The solid-angle element $\mathrm{d}^2\Omega$ is given in units of sr (steradian). In the next step, a projection of $\mathrm{d}^2 A$ onto the perpendicular plane with regard to the direction of propagation $\widehat{s}$ is necessary:

$$\mathrm{d}^2 A_\perp = \cos\theta \cdot \mathrm{d}^2 A. \tag{2.6}$$

F_λ can be derived by integrating $I_\lambda(\widehat{s})$ over all angles within a hemisphere:

$$F_\lambda = \iint\limits_{2\pi} I_\lambda(\widehat{s}) \cdot \cos\theta \, \mathrm{d}^2\Omega = \int_0^{2\pi} \int_0^\pi I_\lambda(\theta, \varphi) \cdot \cos\theta \cdot \sin\theta \, \mathrm{d}\theta \, \mathrm{d}\varphi. \tag{2.7}$$

Assuming an anisotropic radiation field, the downward irradiance $F_\lambda^\downarrow$ is composed of a direct and diffuse component, whereas the upward irradiance $F_\lambda^\uparrow$ consists of a diffuse component only. Contrarily, assuming an isotropic radiation field, the radiance is independent of the orientation of $\widehat{s}$. In this case, the following relation can be derived:

$$F_\lambda = \pi \, \mathrm{sr} \cdot I_\lambda. \tag{2.8}$$

The spectral cloud albedo ρ_λ and spectral surface albedo α_λ are derived from the ratio of upward and downward spectral irradiance. Here, the spectral cloud albedo is related to the particular cloud top (ct), whereas the spectral surface albedo is related to the current surface level (surf).

$$\rho_\lambda(z_{\mathrm{ct}}) = \frac{F_\lambda^\uparrow(z_{\mathrm{ct}})}{F_\lambda^\downarrow(z_{\mathrm{ct}})} \tag{2.9}$$

$$\alpha_\lambda(z_{\mathrm{surf}}) = \frac{F_\lambda^\uparrow(z_{\mathrm{surf}})}{F_\lambda^\downarrow(z_{\mathrm{surf}})}. \tag{2.10}$$

Due to conservation of energy, the particular range of $\rho_\lambda(z_{\mathrm{ct}})$ and $\alpha_\lambda(z_{\mathrm{surf}})$ is limited to values between 0 and 1.

The spectral reflectivity γ_λ can be derived from the quantities F_λ and $I_\lambda(\hat{s})$. With regard to clouds, the spectral reflectivity γ_λ is related to the cloud top altitude z_{ct}. It is defined by the following equation:

$$\gamma_\lambda(z_{\mathrm{ct}}) = \frac{I_\lambda^\uparrow(\theta = \pi, z_{\mathrm{ct}})}{F_\lambda^\downarrow(z_{\mathrm{ct}})} \cdot \pi \, \mathrm{sr}. \tag{2.11}$$

In contrast to the spectral albedo (ρ_λ, α_λ), $\gamma_\lambda(z_{\mathrm{ct}})$ can have values larger than 1. However, in case of an isotropic radiation field, $\gamma_\lambda(z_{\mathrm{ct}})$ yields the same value as $\rho_\lambda(z_{\mathrm{ct}})$, compare Eq. (2.8).

2.2 Cloud Optical Properties

On its way from the top of atmosphere to the surface, solar radiation is scattered, absorbed and emitted by individual particles such as gas molecules, aerosol and cloud particles. To characterize such processes, single-scattering properties are defined (extinction cross section C_{ext}, single–scattering albedo $\tilde{\omega}$, and scattering phase function $\mathcal{P}$).

Liquid water droplets are spherical and Mie–theory yields analytic expressions for these quantities (Mie, 1908; Bohren and Huffman, 1998). The single–scattering properties of non–spherical particles (ice crystals and aerosol particles) cannot be described by an analytic solution and numerical methods have to be applied. Spectral single–scattering properties of different ice crystal shapes and sizes are published e.g. by Baum et al. (2005a,b), Yang et al. (2005), Baum et al. (2007).

2.2.1 Extinction Cross Section

Individual particles attenuate incident electromagnetic radiation, which is quantified by the extinction cross section C_{ext} (a function of the mass to cross–sectional area). It is defined by:

$$C_{\mathrm{ext}} = \frac{\Phi_{\mathrm{ext}}}{F_{\mathrm{inc}}}. \tag{2.12}$$

C_{ext} represents the extinguished radiant energy flux (Φ_{ext}) divided by the incident radiative flux density F_{inc}. The extinguished part of the solar radiation is composed of the scattered and absorbed part of the electromagnetic wave. Thus, the extinction cross section C_{ext} can also be derived by the sum of the scattering cross section C_{sca} and the absorption cross section C_{abs}:

$$C_{\text{ext}} = C_{\text{sca}} + C_{\text{abs}} = \frac{\Phi_{\text{sca}} + \Phi_{\text{abs}}}{F_{\text{inc}}}. \tag{2.13}$$

C_{abs} defines the probability of absorption and is related to the imaginary part of the refractive index. It is given in units of m^2.

2.2.2 Single–Scattering Albedo

The particles single–scattering albedo $\tilde{\omega}$ describes the ratio between the scattering and extinction of electromagnetic radiation. Therefore, it is a mass for the absorbed part of electromagnetic radiation. It is a dimensionless value related to the spectral complex index of refraction. The particle single–scattering albedo is defined by:

$$\tilde{\omega} = \frac{C_{\text{sca}}}{C_{\text{sca}} + C_{\text{abs}}}. \tag{2.14}$$

The magnitude of $\tilde{\omega}$ ranges between 0 (full absorption, no scattering) and 1 (no absorption, only scattering). As for C_{abs}, $\tilde{\omega}$ defines the probability of absorption and is related to the imaginary part of the refractive index $\tilde{n}_{\text{i}}$ (due to the dependence on C_{abs}).

In the visible and near infrared wavelength range below 1000 nm, liquid water droplets show no significant absorption features. Here, $\tilde{\omega}$ yields values almost equal to 1. Beginning at 1500 nm wavelength, liquid water shows increased absorption (decreased $\tilde{\omega}$). An additional feature at the near infrared wavelength range above 1000 nm is the dependence of $\tilde{\omega}$ on the cloud droplet size. $\tilde{\omega}$ decreases with increasing droplet size. Contrarily, this dependence is negligibly small at wavelengths below 1000 nm.

2.2.3 Scattering Phase Function

Solar radiation is scattered into different directions. The scattering phase function $\mathcal{P}(\vartheta, \varphi)$, which is a function of the particles shape, size and orientation, defines the angular probability distribution of the scattered radiation. With regard to μ as the cosine of the solar zenith angle ($\mu_0 = \cos\theta_0$), it is given as a function of the direction of the incident solar radiation (μ', φ') to all scattering directions (μ, φ). Thus, the scattering phase function $\mathcal{P}(\vartheta, \varphi)$, which is normalized to 4π, is given by:

$$\int_0^{2\pi} \int_{-1}^{1} \mathcal{P}([\mu', \varphi'], [\mu, \varphi]) \, \mathrm{d}\mu \, \mathrm{d}\varphi = 4\pi \, \text{sr}. \tag{2.15}$$

If the ice crystals are randomly oriented, or azimuthal averaging is performed, the magnitude of $\mathcal{P}$ reduces to the relation between the incident and scattered direction regarding the observed cross section (scattering plane). Using this relation, given by the scattering angle ϑ:

$$\cos \vartheta = \mu \cdot \mu' + \sqrt{1 - \mu^2} \cdot \sqrt{1 - \mu'^2}, \tag{2.16}$$

the scattering phase function is expressed as $\mathcal{P}(\cos \vartheta)$. Figure 2.2 illustrates $\mathcal{P}(\vartheta)$ for a single cloud droplet and ice crystals of different shapes.
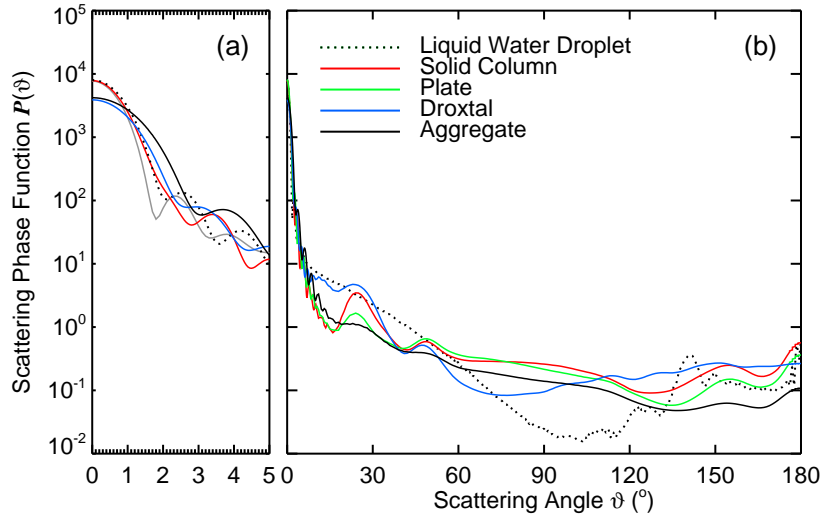

Figure 2.2: Scattering phase function $\mathcal{P}(\vartheta)$ as a function of scattering angles ϑ for a normal distribution of cloud droplets with average diameter of $20\,\mu m \pm 2\,\mu m$ and ice crystals (solid column, plate, droxtal, aggregate), each with a maximum diameter of $20\,\mu m$ at $530\,nm$ wavelength. The $\mathcal{P}(\vartheta)$ of ice crystals and cloud droplets are derived from a data base of scattering features, based on the code by (Yang et al., 2013).

Due to the varying size and shape of the selected cloud particles, the illustrated $\mathcal{P}(\vartheta)$ show significant differences. $\mathcal{P}(\vartheta)$ for ice crystals is smoother than $\mathcal{P}(\vartheta)$ for water droplets. This is a result of the randomly orientation of the ice crystals and/ or the azimuthal averaging of the ice crystals $\mathcal{P}(\vartheta, \varphi)$. $\mathcal{P}(\vartheta)$ of liquid water droplets shows fluctuations, the $\mathcal{P}(\vartheta)$ of the various ice crystals do not. This results from resonances in the solution of the Mie-Theory. Furthermore, the forward scattering peak of liquid water droplets is reduced. Contrarily, the $\mathcal{P}(\vartheta)$ of ice crystals exhibit a strong but narrow forward scattering peak near $\vartheta = 0°$. In the range of the sideward scattering, $\mathcal{P}(\vartheta)$ of liquid water droplets is characteristically lower than that of ice crystals. Further, the $\mathcal{P}(\vartheta)$ of the ice crystals show the characteristic halo structures at $\vartheta = 22°$ and $\vartheta = 46°$, while the cloud droplets show the typical cloud bow at $\vartheta \approx 140°$. Plates and solid columns (hexagonal ground area) exhibit the strongest forward scattering peak, while $\mathcal{P}(\vartheta)$ of aggregates shows the smoothest shape due to random orientation.

2.2.4 Cloud Optical Thickness

The cloud optical thickness τ is a volumetric cloud property. Volumetric cloud properties are derived by integrating over the single scattering properties, weighted by the number-size distribution $\mathrm{d}N/\mathrm{d}D(D)$ with the particle number concentration N of the cloud particles with diameter D (Wendisch et al., 2005).

The cloud optical thickness τ is derived via integration over the spectral volumetric extinction coefficient b_{ext} of a total cloud column from the cloud base z_{base} to the cloud top z_{top}:

$$\tau = \int_{z_{\mathrm{base}}}^{z_{\mathrm{top}}} b_{\mathrm{ext}}(z')\,\mathrm{d}z'. \tag{2.17}$$

b_{ext} in the unit of m^{-1} is defined as follows:

$$b_{\mathrm{ext}} = \int C_{\mathrm{ext}} \cdot \frac{\mathrm{d}N}{\mathrm{d}D'}(D')\,\mathrm{d}D'. \tag{2.18}$$

2.3 Radiative Transfer Equation

The Radiative Transfer Equation (RTE) describes the propagation of electromagnetic radiation in the atmosphere taking absorption, emission, and scattering processes into account. The RTE is determined by the spectral volumetric extinction coefficient b_{ext}, single–scattering albedo $\tilde{\omega}$, and scattering phase function $\mathcal{P}$.

Starting from the law of Beer, Lambert and Bouguer the attenuation of direct solar radiance $I_{\lambda,\mathrm{dir}}(\tau,\mu_0,\varphi_0)$ along a path through the atmosphere is characterized by:

$$I_{\lambda,\mathrm{dir}}(\tau,\mu_0,\varphi_0) = \frac{S_0}{4\pi\,\mathrm{sr}} \cdot \exp\left(-\frac{\tau}{\mu_0}\right), \tag{2.19}$$

S_0 represents the extraterrestrial irradiance at the top of the atmosphere. It is attenuated exponentially along its path through the atmosphere. Considering a solar zenith angle of $30°$ and a cloud with an optical thickness of $\tau = 10$, the transmitted fraction of the direct solar radiance through the cloud is in the range of about $0.1\,\%$. Thus, radiative transfer processes through clouds can only be described taking additionally into account the diffuse part of the solar radiance $I_{\lambda,\mathrm{diff}}$. Originally introduced by Chandrasekhar (1950), the 1D RTE is given by:

$$\mu\frac{\mathrm{d}I_{\lambda,\mathrm{diff}}(\tau,\mu,\varphi)}{\mathrm{d}\tau} = I_{\lambda,\mathrm{diff}} - (J_{\lambda,\mathrm{dir}} + J_{\lambda,\mathrm{diff}}). \tag{2.20}$$

It is valid for plane–parallel and horizontally homogeneous atmospheric conditions. The direction of propagation of $I_{\lambda,\mathrm{diff}}$ is given by μ and φ. The radiation scattered into the viewing direction is characterized by two source terms: a single scattering term $J_{\lambda,\mathrm{dir}}$ and

a multiple scattering term $J_{\lambda,\text{diff}}$. $J_{\lambda,\text{dir}}$ specifies the direct radiation, while $J_{\lambda,\text{diff}}$ specifies the diffuse radiation. The two terms are given by (Wendisch and Yang, 2012):

$$
\begin{aligned}
J_{\lambda,\text{dir}} &= \frac{\tilde{\omega}(\tau)}{4\pi\,\text{sr}} \cdot S_0 \cdot \exp\left(-\frac{\tau}{\mu_0}\right) \cdot \mathcal{P}(\tau, [-\mu_0, \varphi_0], [\mu, \varphi]) \\
J_{\lambda,\text{diff}} &= \frac{\tilde{\omega}(\tau)}{4\pi\,\text{sr}} \int_0^{2\pi} \int_{-1}^{1} I_{\lambda,\text{diff}}(\tau, \mu', \varphi') \cdot \mathcal{P}(\tau, [\mu', \varphi'], [\mu, \varphi])\,\mathrm{d}\mu'\,\mathrm{d}\varphi'.
\end{aligned}
\tag{2.21}
$$

The incoming solar radiation J_{dir} is attenuated according to the law of Beer, Lambert and Bouguer and scattered into the viewing direction. The source terms depend on absorption (as defined by the single–scattering albedo $\tilde{\omega}$) and scattering (as defined by the scattering phase function $\mathcal{P}$). Thus, J_{dir} contains information on the particular ice crystal shape. The diffuse part $J_{\lambda,\text{diff}}$ is also related to $\tilde{\omega}$ and $\mathcal{P}$, but additionally to the cloud optical thickness τ.

2.4 Cloud Microphysical Properties

The scattering phase function for the liquid cloud droplet illustrated in Fig. 2.2 is related to cloud droplets with a size of 20 μm. In reality, liquid water clouds consist of wide spectra of differently sized liquid water droplets. Therefore, the resulting scattering phase function is related to a number-size distribution. The effective cloud droplet radius r_{eff} in units of μm is defined to quantify an average size of cloud droplet populations. It represents the ratio of the third (volume) to the second moment (surface area) of the cloud droplet number size distribution $\mathrm{d}N/\mathrm{d}D(D)$. Here, D is the geometrical droplet diameter. It characterizes the mean droplet radius in an ensemble of cloud droplets, weighted by $\mathrm{d}N/\mathrm{d}D(D)$. The effective cloud droplet radius r_{eff} is given by:

$$
r_{\text{eff}} = \frac{1}{2} \frac{\int D'^3 \frac{\mathrm{d}N}{\mathrm{d}D'}(D')\,\mathrm{d}D'}{\int D'^2 \frac{\mathrm{d}N}{\mathrm{d}D'}(D')\,\mathrm{d}D'}.
\tag{2.22}
$$

Following Yang et al. (2000) and Key et al. (2002), r_{eff} can also be defined for ice crystals. To derive r_{eff} for an ice crystal, its maximum dimension $D_{\max}$, its volume V_D and its projected area A_D have to be determined. The definition of r_{eff} for ice crystals is then given as follows:

$$
r_{\text{eff}} = \frac{3}{4} \frac{\int V_{\text{D}}(D') \cdot \frac{\mathrm{d}N}{\mathrm{d}D'}(D')\,\mathrm{d}D'}{\int A_{\text{D}}(D') \cdot \frac{\mathrm{d}N}{\mathrm{d}D'}(D')\,\mathrm{d}D'}.
\tag{2.23}
$$

V_D and A_D are derived from calculating the diameter of a sphere, which consists of the same volume to surface ratio as the ice particle would have (Grenfell and Warren, 1999; Yang et al., 2000).

The liquid water content LWC defines the mass of liquid water in a cloud volume of $1\,\text{m}^3$. With the density of liquid water ϱ_{w}, it is defined as follows:

$$
\text{LWC} = \varrho_{\text{w}} \cdot \frac{4}{3} \cdot \pi \cdot \int \left(\frac{D'}{2}\right)^3 \cdot \frac{\mathrm{d}N}{\mathrm{d}D'}(D')\,\mathrm{d}D',
\tag{2.24}
$$

Following Brenguier et al. (2011), the LWC can be described for a vertically homogeneous cloud at an altitude between z_{base} and z_{top} by the use of the prior defined r_{eff} and τ:

$$\text{LWC} = \frac{2}{3} \cdot \int_{z_{\text{base}}}^{z_{\text{top}}} \frac{r_{\text{eff}} \cdot \tau \cdot \varrho_{\text{w}}}{z'} \, \mathrm{d}z'. \tag{2.25}$$

In reality, vertically homogeneous clouds are exceptional. Commonly, the droplet size increases from the cloud base to the cloud top. Wood and Hartmann (2006) showed that by using 5/9 instead of 2/3, Eq. (2.25) turns into the relation for such adiabatic clouds. The definition of the LWC can also be translated to ice clouds. Here, the ice water content IWC is defined as follows:

$$\text{IWC} = \varrho_{\text{i}} \cdot \int V_{\text{D}}(D') \cdot \frac{\mathrm{d}N}{\mathrm{d}D'}(D') \, \mathrm{d}D', \tag{2.26}$$

where ϱ_{i} gives the density of an ice crystal with the volume V_{D}.

3 Experimental

This chapter characterizes the technical parameters of the imaging spectrometer AisaEAGLE, which was used for the measurements presented in this thesis. The calibration procedure, data handling and necessary corrections are introduced in Sect. 3.1.1 to 3.2.6. Details of the observation geometry and the derivation of scattering angles from AisaEAGLE measurements are provided in Sect. 3.3. Parts of this chapter have been published in Schäfer et al. (2013, 2015).

3.1 Imaging Spectrometer AisaEAGLE

3.1.1 Specifications

The AisaEAGLE is a commercial imaging spectrometer, which is manufactured by Specim Ltd. in Finland (technical specifications summarized in Tab. 3.1, Hanus et al., 2008; Schäfer et al., 2013). It is an analytically detection and mapping instrument, originally designed for airborne applications. AisaEAGLE has been applied in various fields including forestry management, environmental investigations, target identification, water assessment, and land use planning.

The AisaEAGLE is a single-line sensor with 1024 spatial pixels. The instrument measures radiances in three dimensions: space, time and wavelength. The spatial and spectral dimensions are resolved by an optical assembly that displays the image onto a two-dimensional (2D) sensor chip. The third dimension, time, corresponds to the motion of the scene, which passes the sensor. An optical schematic for the path of the electromagnetic radiation detected by the AisaEAGLE is shown in Fig. 3.1.

The incoming solar radiation within the FOV of AisaEAGLE is collected by a lens and an entrance slit. Collimating optics direct the radiation to a grating (dispersing element), where it is dispersed into its spectral components. The spectral components are focused on the detector, which consists of a **c**harge-**c**oupled **d**evice (CCD) element for the spatial and spectral dimensions.

AisaEAGLE is applied to ground-based and airborne measurements. For airborne measurements (e.g., Bierwirth et al., 2013; Schäfer et al., 2015), the 2D image evolves from the sensor movement. During ground-based applications, the 2D image evolves from the cloud movement across the sensor line (Schäfer et al., 2013). If the sensor is aligned perpendicular to the heading of the aircraft or the direction of the cloud movement, 2D images of clouds with high spatial resolution (1024 spatial pixels within 37° FOV) are obtained. The FOV of the
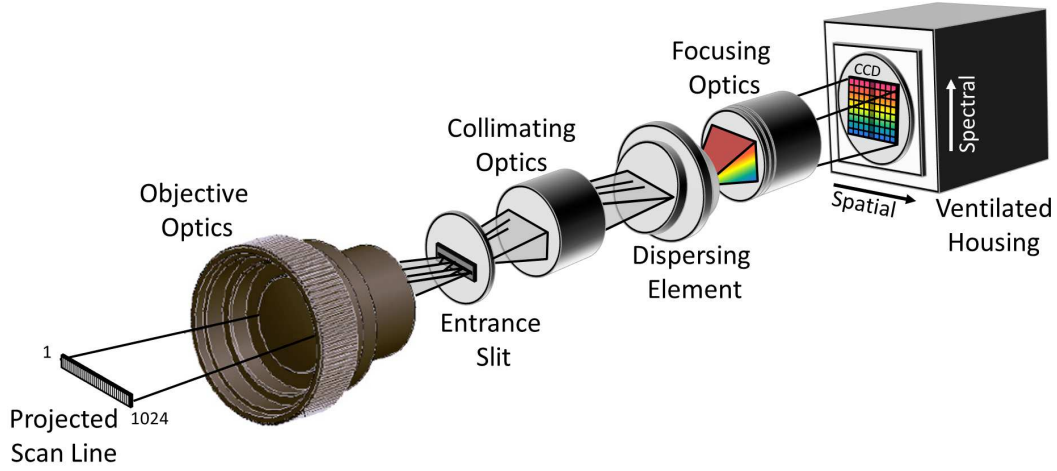
Figure 3.1: Optical scheme of an imaging spectrometer.

AisaEAGLE and the detected swath of the measured scene depends on the lens that is used for the measurements. The measurements presented in the following were performed with a 36.7° lens (18.09 mm focal length) and a 36.3° lens (18.30 mm focal length). Figure 3.2 shows the size of a single image pixel and the swath of the entire image as a function of the distance to the target for the 36.7° lens.
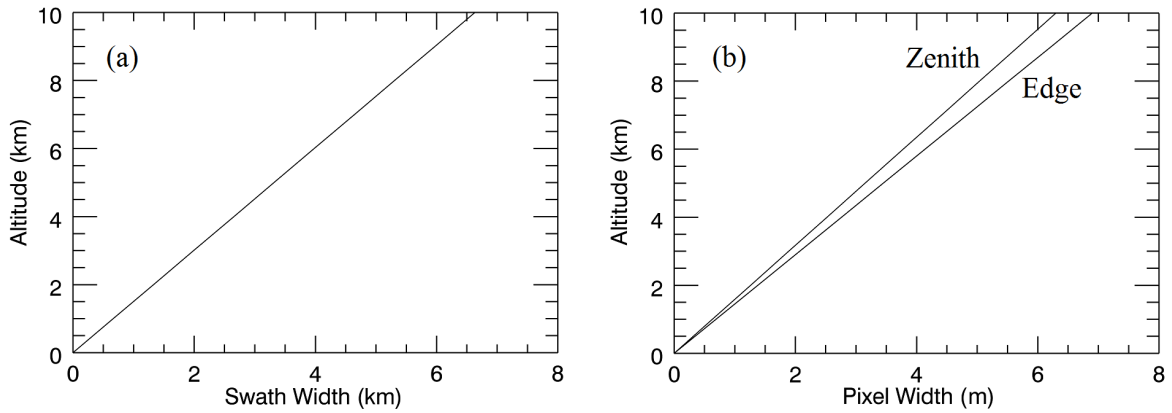
Figure 3.2: Characteristic **(a)** swath and **(b)** pixel width for AisaEAGLE using the 36.7° lens.

The swath s of a detected scene at a distance of Δz is derived by:

$$s = 2 \cdot \tan\left(\frac{1}{2}\text{FOV}\right) \cdot \Delta z. \tag{3.1}$$

The opening angle of each spatial pixel FOV_{pix} is obtained by the total FOV and the total number of spatial pixels n_{pix}.

$$\text{FOV}_{\text{pix}} = \frac{\text{FOV}}{n_{\text{pix}}} \tag{3.2}$$

The width of each spatial pixel s_{pix} is obtained from the combination of Eqs. (3.1) and (3.2), which leads to:

$$s_{\text{pix}} = [\tan(n_{\text{pix}} \cdot \text{FOV}_{\text{pix}}) - \tan((n_{\text{pix}} - 1) \cdot \text{FOV}_{\text{pix}})] \cdot \Delta z, \quad n_{\text{pix}} = -512, ..., -1, 1, ..., 512 \tag{3.3}$$

While the swath increases with distance to the cloud by the tangent of the opening angle, the pixel size depends on its position on the sensor line. The FOV of a pixel (the pixel width) in the center (viewing zenith) is smaller than that of a pixel at the edge. For example, a cloud at an altitude of 10 km yields an average pixel size of 6.6 m (6.3 m–6.9 m) with 6.7 km swath. To obtain 2D images, the temporal dimension of the spectral measurements translates to a spatial quantity: the length l_{pix} of the FOV of a pixel is the product of the perpendicular cloud drifting velocity v_{cloud} (ground-based application) or the aircraft speed v_{aircraft} (airborne application) and the selected integration time t_{int} for the measurement. Accounting for a non-perfect perpendicular orientation with the angle α between the flow direction of the cloud or heading of the aircraft and the orientation of the sensor line, l_{pix} is given by:

$$l_{\text{pix}} = |\sin \alpha| \cdot v_{\text{cloud, aircraft}} \cdot t_{\text{int}}. \tag{3.4}$$

The AisaEAGLE CCD element consists of 1024 spectral pixels for the hypothetic wavelength range from 100 to 1300 nm. However, due to the optical assembly, the effective spectral range of AisaEAGLE is decreased to 488 pixels ($n_{\text{pix}} = 279\text{–}766$) in the range of 400 to 970 nm (effective wavelength range). Spectral pixels below or above this range receive stray light from pixels within the effective wavelength range. This makes those pixels useless for data evaluation.

Since the spectral range of AisaEAGLE covers more than one octave, the range from 800–970 nm requires order sorting. This results from the spectrometer technique that is based on a transmission diffraction grating where the different wavelengths are diffracted to angle β according to the grating equation:

$$M \cdot \lambda = d(\sin\alpha + \sin\beta), \tag{3.5}$$

Here, M is the diffraction order (0, ± 1, ± 2, ...), λ is the wavelength, d is the groove spacing and α is the angle between incoming radiation and the grating. There is more than one wavelength that satisfies this equation for a particular set of α and β. In practice, this means that there are overlapping orders of spectra that go to the same place on the detector surface. To avoid this, AisaEAGLE has a second order depression using order blocking filters mounted near the detector.

Applying the full spatial and spectral (1.25 nm full width at half maximum, FWHM) resolution to the AisaEAGLE measurements, the frame rate (frames per second, FPS) is adjustable from 4 to 30 Hz, while for ground-based applications 4 to 10 Hz and for airborne applications 20 to 30 Hz were found to be sufficient. Depending on the frame rate, the integration time is adjustable between 0.1 and 200 ms; it is chosen with regard to the particular illumination of the scene to avoid a saturation of the sensor pixels.

3.1.2 Binning

The AisaEAGLE produces vast amounts of data. A rough approximation arrives at $75\,\mathrm{GB}$ of data per hour. This value can be reduced by lowering the spectral and/or the spatial resolution, so–called binning. Furthermore, this leads to an increased possible recording speed because pixels are physically joined in read–out, which reduces the process steps to read an image frame from the sensor. It is also possible to reduce the spectral range or resolution using band files, but that does not affect the recording speed as it does not reduce the amount of physical read-out steps. Figure 3.3 illustrates the binning procedure for spatial and spectral binning and a combination of both. The number of spatial pixels and spectral bands depends on the applied binning; e.g. a 2x2 binning results in 512 spatial pixels and 244 spectral bands. Accordingly, Eq. (3.2) and Eq. (3.3) have to be adjusted. The available FWHM, frame rate and number of spectral bands for the different binning configurations are listed in Tab. 3.1.
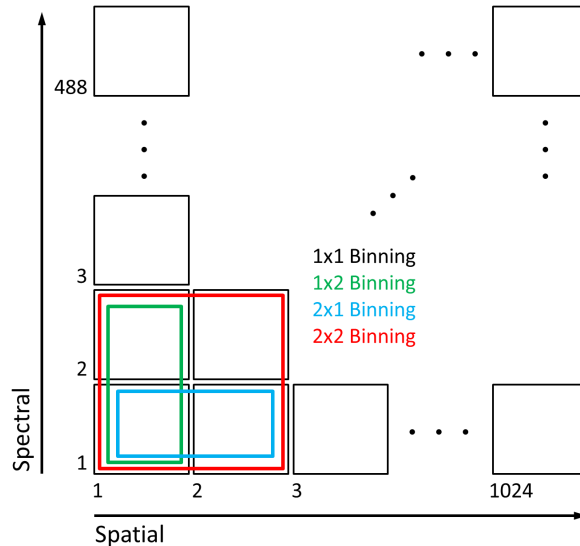
Figure 3.3: Scheme of AisaEAGLEs binning procedure for 1x1, 1x2, 2x1, and 2x2 binning.

Because of the increased possible recording speed the instrument allows the usage of higher frame rates. This is important especially for airborne observations. Due to the high speed of an aircraft, a too low frame rate causes gaps in the observed scene.

3.2 Calibrations and Data Handling

3.2.1 Radiometric Calibration

AisaEAGLE converts the detected photon counts into digital 12-bit numbers, which results in 0 to 4096 Analog-Digital-Units (ADU) per integration time. An absolute radiometric calibration is necessary to transform those numbers (Signal S) into radiances I_λ in units of

Table 3.1: Summarized specifications of the imaging spectrometer AisaEAGLE.

Parameter	Specification
Number of spatial pixels	1024
Number of spectral bands (total / effective)	1024 / 488
Spectral range λ	400–970 nm
Spectral resolution (depending on binning)	1.25–9.2 nm
Target resolution at 1000 m distance (center pixel)	0.68 m
Swath width	0.68 $\cdot$ distance
Slit width	30 µm
Focal Length	18.5 mm
FOV	37.7°
Image Rate (FPS)	4–160 Hz
SNR (depending on band configuration)	350:1–1400:1
Integration Time t_{int}	Adjustable to FPS
Output	12 bits digital

Spectral binning options	1–X	2–X	4–X	8–X
Number of spectral bands (effective)	488	244	122	60
Spectral resolution (FWHM)	1.25 nm	2.3 nm	4.6 nm	9.2 nm
Image rate, up to (FPS)	30 Hz	50 Hz	100 Hz	160 Hz

$\text{W m}^{-2}\,\text{nm}^{-1}\,\text{sr}^{-1}$. The manufacturer provides a data sheet with calibration factors. Because of the fixed mounting of the AisaEAGLE optics within a solid housing, those calibration factors are supposed to be temporally constant. Nevertheless, this stability is checked using a radiometric calibration in the laboratory, before and after the AisaEAGLE imaging spectrometer is transported to field observations. The radiometric calibration is performed with an integrating sphere, a certified radiance standard (uncertainty: $\pm 6\,\%$), traceable to the United States National Institute of Standards and Technology. The calibration setup using an integrating sphere is illustrated in Fig. 3.4.

The integrating sphere is hollow with a barium sulfate coating on the inner walls. Thus, the inside of the integrating sphere is assumed to be a Lambertian reflector. The spectral radiation is emitted into the sphere by a halogen lamp, which is installed at the side of the sphere and mounted within a ventilated housing. The spectral, diffuse radiation exits the sphere through an aperture at the front side. It is sampled by the AisaEAGLE inlet, which is positioned in a distance of about 1 cm in front of the aperture. Due to this distance, a black fabric is used to prevent from additional radiation, which might enter the optical path from outside the sphere. Furthermore, a baffle inside the sphere prevents from measuring the direct, not yet diffuse radiation of the lamp.

During operation, the integrating sphere emits diffuse radiation, which is well–calibrated in the wavelength range from 380 to 2500 nm. Thus, the integrating sphere provides sufficient
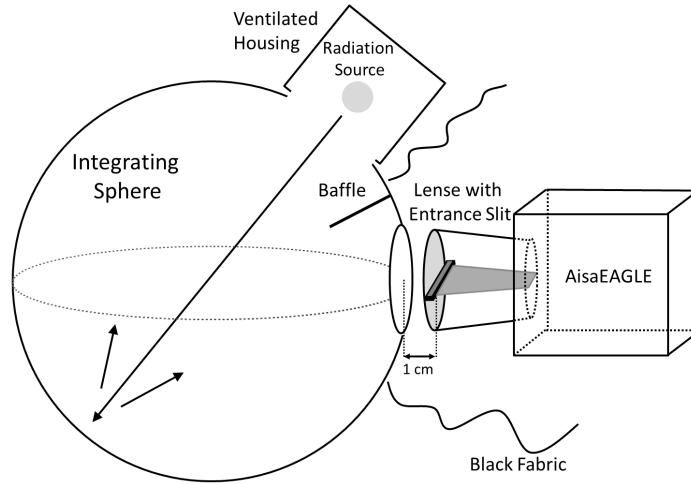
Figure 3.4: Scheme of the setup for the absolute radiometric calibration of the AisaEAGLE imaging spectrometer using an integrating sphere.

coverage of the AisaEAGLE effective wavelength range. The calibration factors in units of $\mathrm{W\,m^{-2}\,nm^{-1}\,sr^{-1}\,ADU^{-1}}$ for each spatial pixel are obtained from:

$$f_{\mathrm{c}}(\lambda, n_{\mathrm{pix}}) = \frac{S_{\mathrm{cal}}(\lambda)}{S_{\mathrm{meas}}(\lambda, n_{\mathrm{pix}})}, \tag{3.6}$$

where S_{cal} defines the calibrated output of the integrating sphere in $\mathrm{W\,m^{-2}\,nm^{-1}\,sr^{-1}}$ and S_{meas} defines the detected signal of each spatial and spectral pixel in ADU. Figure 3.5 illustrates the spectral calibration factors f_{c} derived from the absolute calibration of AisaEAGLE as a function of the spatial pixel number. The corresponding calibration uncertainty is exemplarily illustrated for the first and central spatial pixel in Fig. 3.6a and for three selected wavelengths in Fig. 3.6b. Those wavelengths are selected to cover both ends of the detectable wavelength range as well as the largest and lowest uncertainty ranges.
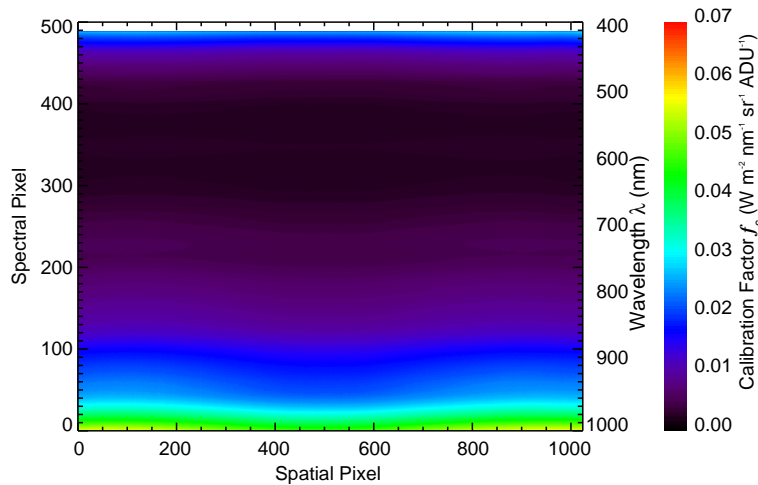

Figure 3.5: Calibration factors from the absolute radiometric calibration of AisaEAGLE.
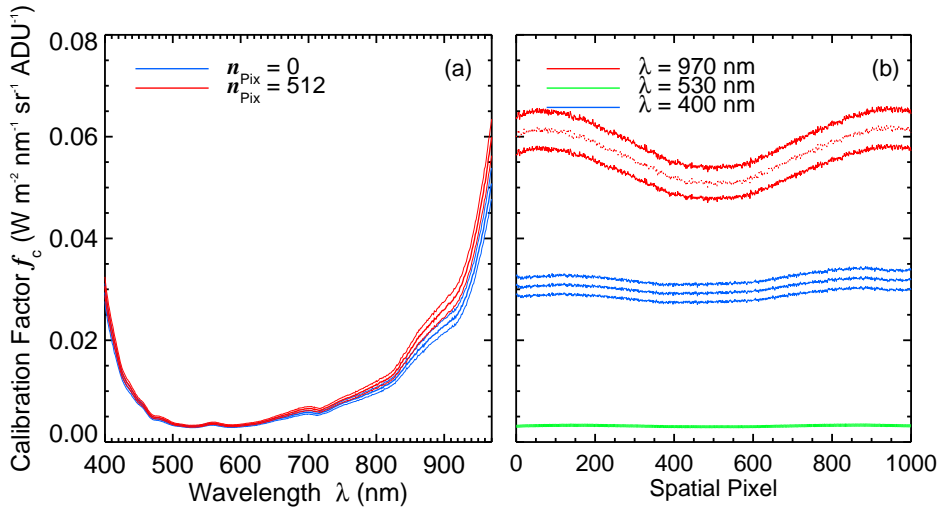
Figure 3.6: Calibration factors from the absolute radiometric calibration of AisaEAGLE. Average and calibration uncertainty **(a)** of first and central spatial pixel as a function of wavelength and **(b)** at 400 nm, 530 nm, and 970 nm wavelength as a function of the spatial pixel number.

The spectral calibration factors are largest at both ends of the detectable wavelength range and show a minimum at wavelengths between 500 and 600 nm. Largest values are found for the longest wavelengths. On the spatial axis, the calibration factors show a distinct minimum for the center pixels and two symmetrical maxima compared to the central pixel close to the edge of the sensor line. The significance of these maxima increases with increasing wavelength.

3.2.2 Dark Current

Another parameter that has to be considered during the calibration procedure and during the operational application is the dark current. It is a signal generated by the instrument itself, which has to be characterized and subtracted from the measurements. It originates from the thermal movement of the CCDs molecules, which leads to the formation of free charge carriers increasing the signal also in the unlighted state. The dark current is determined using a shutter inside the optical path of AisaEAGLE. In the operational mode, a dark measurement with a temporal duration of 3 s is performed subsequently of each scan. During the radiometric calibration, two separate measurements are performed. A measurement with opened shutter, illuminated detector (S_{lum}) and another one with closed shutter (S_{dark}). For both measurements, the same integration time is applied. Figure 3.7 illustrates the dark current of AisaEAGLE as a function of spectral bands and spatial pixel number. The dark measurements are averaged separately for each spatial pixel. The resulting value represents the dark current. It is subtracted from the dedicated illuminated measurements, before the calibration factors are calculated. This procedure makes the calibration factors independent of the dark current. Figure 3.7 reveals that the dark current from AisaEAGLE measurements yields no significant wavelength dependence over the detectable wavelength range. The measured dark current is almost constant at $50\,\text{ADU} \pm 3\,\text{ADU}$ (1.2 % of detection limit).
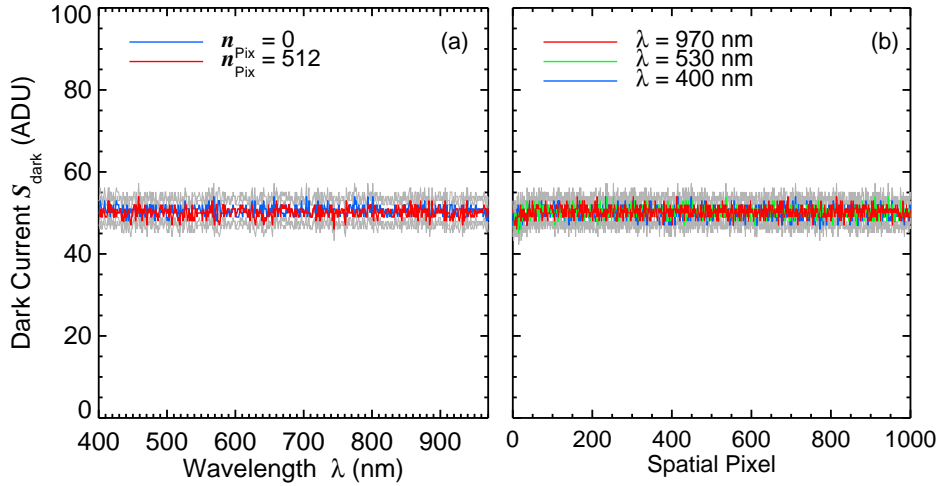
Figure 3.7: Dark current of AisaEAGLE. Average (colored solid lines) and uncertainty (gray-shaded area) **(a)** of first and central spatial pixel as a function of wavelength and **(b)** at 400 nm, 530 nm, and 970 nm wavelength as a function of the spatial pixel number.

Furthermore, a dependence on temperature and integration time was not established. The temperature dependence was tested with a comparison of dark current measurements at 5 and 20°. Therefore, this value is more a constant offset than a typical dark current, generated by the instruments temperature.

3.2.3 Linearity

Tests have proven a linear relation between the detected signal and the intensity of the radiation source, see Fig. 3.8a. It shows the saturation of the center spatial pixel for different wavelength as a function of the output of the integrating sphere. This saturation increases linearly with increasing intensity of the lamp; the linear fit matches the single measurement points. As a function of the integration time, Fig. 3.8b illustrates the pixel saturation (in %), which is the measured raw signal after dark current subtraction (%), normalized to the maximum saturation of the CCD and current output of the lamp. This pixel saturation increases linearly with increasing integration time. The linear fits match the single data points ($R^2 = 0.99$).

This linear relation allows a normalization of the calibration factors by the integration time. This simplifies the data evaluation to the subtraction of the particular measured dark current and multiplication of the measured signal by the normalized calibration factors. Therefore, the relation between the measured raw data and the calibrated radiances I_λ for each spatial and spectral pixel are given by:

$$I_\lambda(n_{\text{pix}}) = f_{\text{c}}(\lambda, n_{\text{pix}}) \cdot \frac{S_{\text{lum}}(\lambda, n_{\text{pix}}) - S_{\text{dark}}(\lambda, n_{\text{pix}})}{t_{\text{int}}}. \tag{3.7}$$
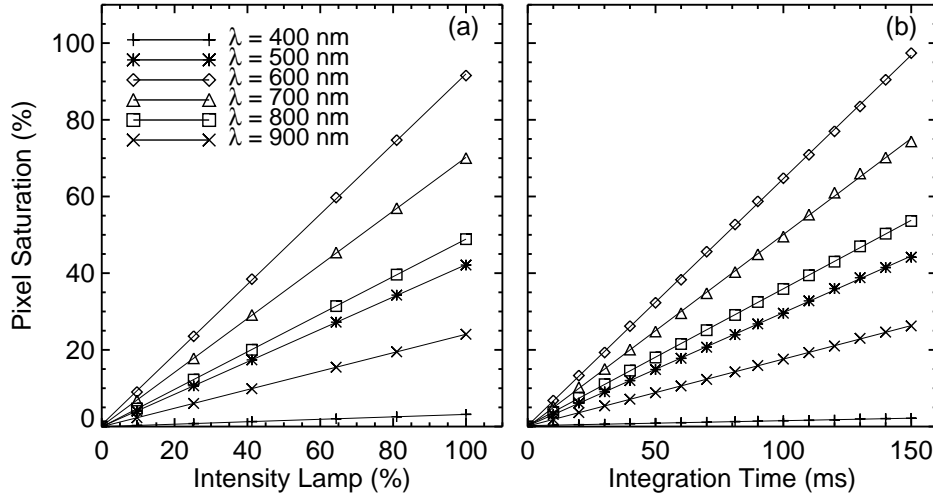
Figure 3.8: Measured raw signal after dark current subtraction (%), normalized to the maximum saturation of the CCD and current output of the lamp, as a function of the **(a)** intensity of the integrating sphere and **(b)** applied integration time. The data are exemplarily depicted for the center spatial pixel ($n_{\mathrm{pix}} = 512$) and the six selected wavelengths of $\lambda = 400; 500; 600; 700; 800; 900\,\mathrm{nm}$.

3.2.4 Spectral Calibration

The manufacturer provides a spectral calibration, mapping wavelengths to the spectral pixel number. A test was carried out in the laboratory using spectral lamps with defined emission lines. The applied Penray spectral lamps and spectral emission lines are listed in Tab. 3.2. The lamps are quite thin; it is difficult to fully cover the whole detector of the AisaEAGLE. Therefore, during the test of the wavelength calibration of AisaEAGLE, the spectral lamps were placed within an integration sphere to better illuminate the detector. A comparison of those pixels showing the largest amplitude with the wavelength calibration file that was provided by the manufacturer revealed sufficient agreement on all checked emission lines.

Table 3.2: Emission lines of spectral lamps applied for the wavelength calibration.

Lamp	Wavelength of Emission Lines (nm)
Argon	727.29 763.51 826.45 866.79 922.45 965.78
Mercury	404.66 435.83
Neon	621.73 692.95

3.2.5 Measurement Uncertainties

The measurement uncertainty of AisaEAGLE results from uncertainties in the absolute calibration and (less importantly) the measured signal. The uncertainty in the absolute calibration results from the uncertainty of the integrating sphere. The manufacturer specifies this uncertainty to be about $\pm 6\,\%$ for the wavelength range detected by the AisaEAGLE.

The uncertainty of the measured signal is related to its signal–to–noise (SNR) ratio. The manufacturer specifies the SNR of the AisaEAGLE to be in a range of 350:1 to 1400:1, depending on the band configuration (spatial and spectral binning). With a dynamic range of the single pixels from 0 to 4096 ADU, the uncertainty in the measured signal, which is generated by the SNR can be neglected compared to the uncertainty generated by the integration sphere. Depending on the band configuration, it exhibits maximum values of only 0.07 to 0.29 % (inversely proportional).

3.2.6 Smear correction

Since the AisaEAGLE detector is based on CCD technique, it is necessary to correct for the smear effect in calibration and measurement data. The smear effect occurs during the read-out process of the collected photoelectrons, which are shifted step by step from one spectral pixel to the neighbouring one into the direction of the read-out unit (Fig. 3.9). The read-out process is not infinitely fast. Due to the fact that radiation can still reach the sensor during read-out, the pixels are contaminated by an additional signal. The read-out process begins at the red end of the spectral range. Therefore, the additional signal (smear effect) is larger for shorter wavelengths, because the corresponding charges have to traverse the entire chip.
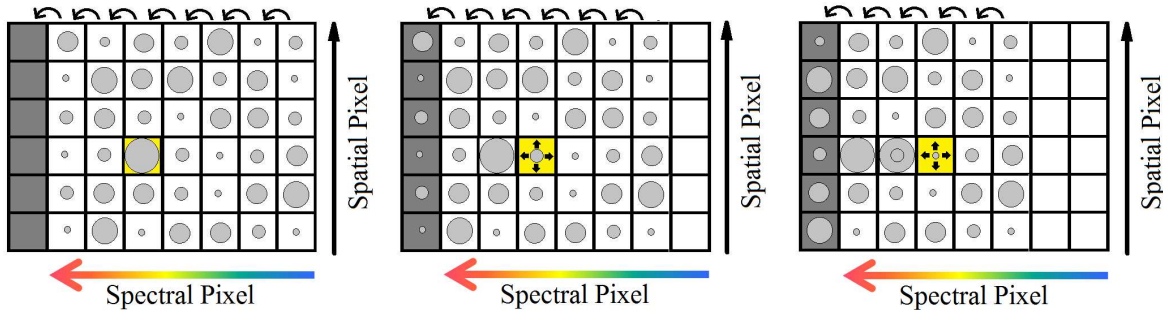
Figure 3.9: Illustration of the read-out process and the smear effect. The gray bar on the left side illustrates the read-out unit. The arrows indicate the shifting direction of the photoelectrons. The magnitude of the signal of each pixel is indicated by the size of the circles. The smear effect is illustrated for one spatial pixel, which is exposed to additional illumination at one spectral pixel (yellow) during the read-out process.

The measurements are corrected for the smear effect by applying the correction algorithm:

$$x_1 = y_1,$$
$$x_2 - S_\mathrm{c} \cdot y_1 = y_2,$$
$$x_3 - S_\mathrm{c} \cdot (y_1 + y_2) = y_3,$$
$$\cdots,$$
$$x_n - S_\mathrm{c} \cdot (\Sigma_{i=1}^{n} y_{i-1}) = y_n, \tag{3.8}$$

where x_i are the uncorrected and y_i are the corrected digital counts with the wavelength index $i = 1, \ldots, n$. The smear correction factor $S_\mathrm{c} = t_\mathrm{read\text{-}out} / t_\mathrm{int}$ is the ratio of the duration

of a read-out step ($t_{\text{read-out}} = 1.33\,\mu$s) to the total integration time. For the first read-out step no correction is necessary, since the counts from the first pixel are shifted directly into the read-out unit. During the whole read-out process, the illumination of all pixels is assumed to remain constant. Therefore, new charges are still generated while the original charges are already shifted towards the read-out unit. The original charge from a given pixel increases by the radiation that falls on the pixel the charge travels through. The increase is proportional to the smear correction factor S_c as well as the illumination of the pixels (see the fourth line of Fig. 3.9).

The smear effect must be taken into account for each measurement as well as for the calibration. Tests have shown that during atmospheric measurements the signal outside the effective wavelength range can be neglected for the smear correction (which significantly reduces the required data storage space). This is because solar spectral radiance is typically larger for shorter (400 nm) than for longer (900 nm) wavelengths. This does not hold for the calibration. The halogen calibration lamp of the integrating sphere is colder than the Sun and emits radiation with a maximum in the near-infrared range (1000 nm) and low values at shorter wavelengths (400 nm). Consequently, the wavelength pixels outside the effective wavelength range above 1000 nm receive a significant amount of radiation.
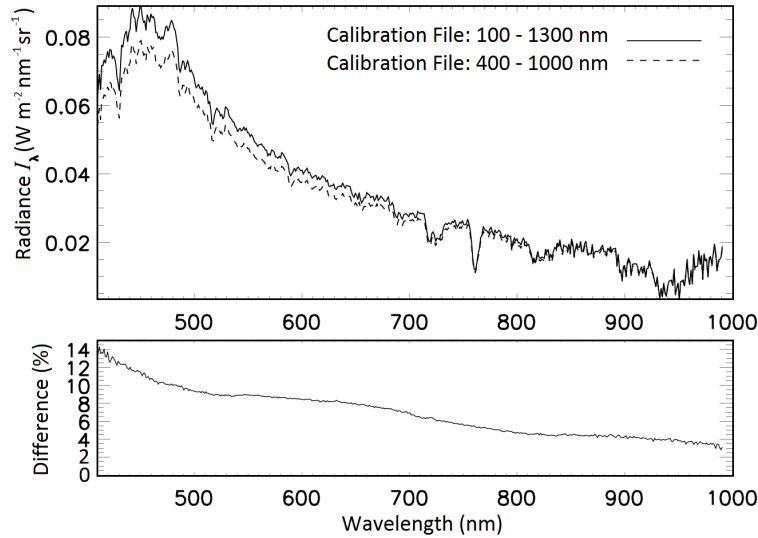
Figure 3.10: **(a)** Spectral radiance measured with AisaEAGLE, for smear corrections considering different wavelength intervals in the calibration: 100–1300 nm (solid line), 400–1000 nm (dashed line). **(b)** Differences between the spectral radiances shown in panel (a).

A comparison between calibration radiance measurements derived with and without including the wavelength pixels outside the effective wavelength range above 1000 nm is shown in Fig. 3.10. Significant differences are observed for wavelengths below 500 nm, which agrees with the theory of the smear effect. Differences range from 3 % at 970 nm wavelength to 13 % at 400 nm wavelength. Therefore, it is necessary to use the entire AisaEAGLE spectral range during calibration, even though it is not used during data evaluation.

3.3 Observation Geometries and Scattering Angle Derivation

Spectral radiance measurements with high spatial resolution obtained from the AisaEAGLE imaging spectrometer are used in this thesis to identify the shape of ice particles in cirrus. Since each spatial pixel refers to a specific viewing zenith angle θ, each spatial pixel receives scattered radiation from a different solid angle Ω. This can be referred to features of the scattering phase function. Figure 3.11 illustrates the measurement geometry needed to derive the scattering angles ϑ for each spatial pixel.
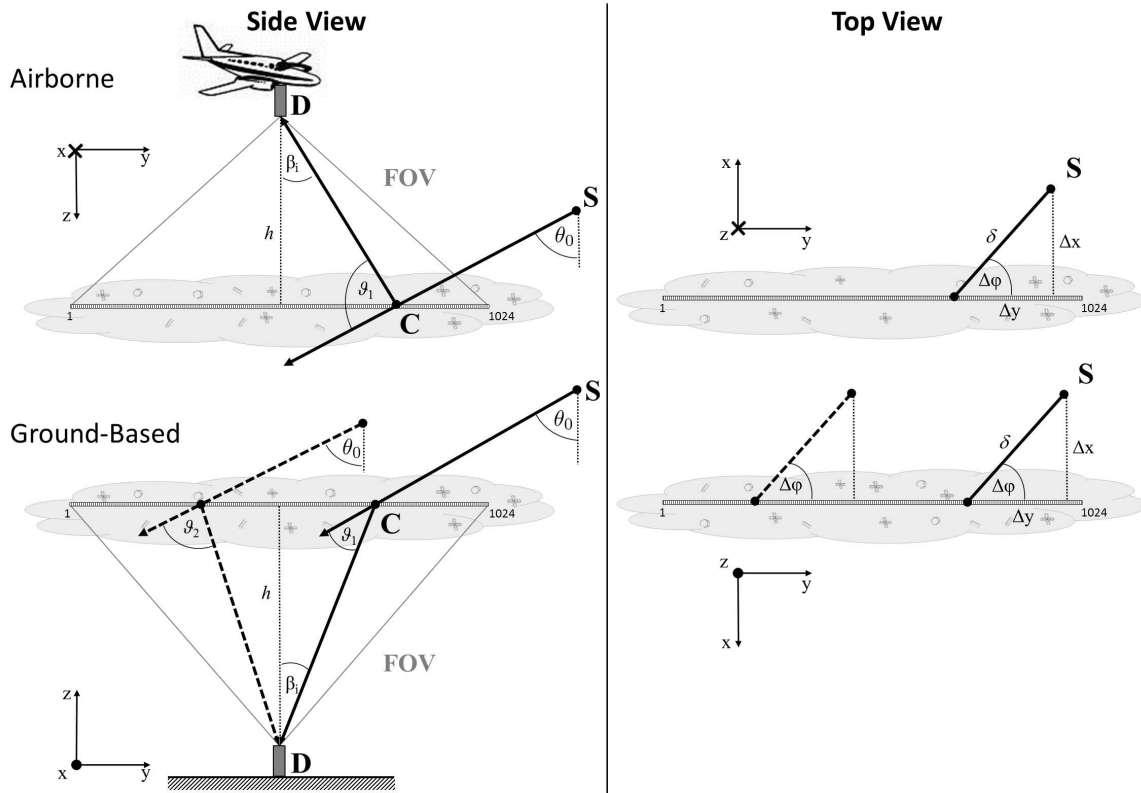
Figure 3.11: Illustration of the ground-based and airborne AisaEAGLE measurement geometry in a Cartesian coordinate system (x, y, z) with position of the Sun (S), a scattering cloud particle (C) and the AisaEAGLE detector (D). θ_0 is the solar zenith angle, φ_0 the solar azimuth angle, ϑ the scattering angle, and β_i the viewing angle of the corresponding pixel i.

According to Eq. (2.16), for airborne (AB) and ground–based (GB) applications, the scattering angle ϑ is calculated from the scalar product of the vector of the incoming solar radiation $(\overrightarrow{SC})$ and the vector of the radiation scattered into the sensor direction $(\overrightarrow{CD})$:

$$\vartheta = \arccos\left(\frac{\overrightarrow{SC} \cdot \overrightarrow{CD}}{|\overrightarrow{SC}| \cdot |\overrightarrow{CD}|} \right). \tag{3.9}$$

The applied coordinate system is related to the coordinate system of the sensor (mathematical positive). Thus, the orientation of the scattering plane is given by the orientation of the

AisaEAGLE sensor line. Related to ground–based observations this results in measurements of the transmitted radiance $I_\lambda^\downarrow$ and related to airborne observations in measurements of the reflected radiance $I_\lambda^\uparrow$. In contrast to Eq. (2.16), no azimuthal averaging is performed and the solar azimuth angle has to be considered as well. Regarding the Cartesian coordinate system of the sensor (Fig. 3.11), $\overrightarrow{SC}$ and $\overrightarrow{CD}$ yield the following:

$$\overrightarrow{SC}_{\mathrm{GB}} = \begin{pmatrix} \delta \cdot \sin\Delta\varphi \\ -\delta \cdot \cos\Delta\varphi \\ -\delta/\tan\theta_0 \end{pmatrix} \qquad \overrightarrow{CD}_{\mathrm{GB}} = \begin{pmatrix} 0 \\ -h \cdot \tan\beta_{\mathrm{i}} \\ -h \end{pmatrix}$$

$$\overrightarrow{SC}_{\mathrm{AB}} = \begin{pmatrix} -\delta \cdot \sin\Delta\varphi \\ -\delta \cdot \cos\Delta\varphi \\ \delta/\tan\theta_0 \end{pmatrix} \qquad \overrightarrow{CD}_{\mathrm{AB}} = \begin{pmatrix} 0 \\ -h \cdot \tan\beta_{\mathrm{i}} \\ -h \end{pmatrix} \qquad (3.10)$$

Here, δ is the vector between S and C projected onto the x-y-plane. The values of β_{i} are considered positive for pixels viewing into the direction of the Sun (solid arrows in Fig. 3.11) and negative for pixels viewing away from the Sun (dotted arrows in Fig. 3.11). $\Delta\varphi$ is the relative difference between the solar (φ) and the sensor (φ_{Sen}) azimuth angles. φ_{Sen} is given by the viewing azimuth angle of the spatial pixel number 1024.

Solving the scalar product of Eq. (3.9), using the definitions for the vectors $\overrightarrow{SC}_{\mathrm{GB}}$ and $\overrightarrow{CD}_{\mathrm{GB}}$ from Eq. (3.10), the scattering angle ϑ is obtained by:

$$\vartheta_{\mathrm{GB}} = \arccos\left(\frac{\delta h \cdot \cos\Delta\varphi \cdot \tan\beta_{\mathrm{i}} + \delta h/\tan\theta_0}{\sqrt{h^2\tan^2\beta_{\mathrm{i}} + h^2} \cdot \sqrt{\delta^2\sin^2\Delta\varphi + \delta^2\cos^2\Delta\varphi + \delta^2/\tan^2\theta_0}}\right)$$

$$= \arccos\left(\frac{\cos\Delta\varphi \cdot \tan\beta_{\mathrm{i}} + 1/\tan\theta_0}{\sqrt{1 + \tan^2\beta_{\mathrm{i}}} \cdot \sqrt{1 + 1/\tan^2\theta_0}}\right). \qquad (3.11)$$

Multiplying $\tan\theta_0/\tan\theta_0$ to Eq. (3.11) and using the following relations:

$$1 = \sin^2x + \cos^2x \qquad (3.12)$$

$$\sin x = \sqrt{1 - \cos^2x} = \frac{\tan x}{\sqrt{1 + \tan^2x}} \qquad (3.13)$$

$$\cos x = \sqrt{1 - \sin^2x} = \frac{1}{\sqrt{1 + \tan^2x}}, \qquad (3.14)$$

Eq. (3.11) simplifies to:

$$\vartheta_{\mathrm{GB}} = \arccos\left(\cos\varphi_0 \cdot \sin\theta_0 \cdot \sin\beta_{\mathrm{i}} + \cos\theta_0 \cdot \cos\beta_{\mathrm{i}}\right). \qquad (3.15)$$

Consequently, regarding airborne applications, the scalar product of Eq. (3.9) yields:

$$\vartheta_{\mathrm{AB}} = \arccos\left(\cos\varphi_0 \cdot \sin\theta_0 \cdot \sin\beta_{\mathrm{i}} - \cos\theta_0 \cdot \cos\beta_{\mathrm{i}}\right). \qquad (3.16)$$

The final Eq. (3.15) and (3.16) differ from Eq. (2.16) by the additional azimuthal dependence, which is given by the term $\cos\varphi_0$. Both Eqs. (3.15) and (3.16) imply that the largest coverage of the scattering angle range can be derived for an orientation of the AisaEAGLE sensor line along the direction of the solar azimuth ($\Delta\varphi = 0°$). For a perpendicular orientation ($\Delta\varphi = 90°$) of the sensor line with regard to the solar azimuth angle φ, the first term of Eq. (3.15) and Eq. (3.16) yields $\vartheta = 0°$. In this case, only a narrow range of scattering angles close to the particular solar zenith angle can be derived. Conversely, for an orientation of the AisaEAGLE sensor line along the solar azimuth angle φ ($\Delta\varphi = 0°$), the absolute range of the detectable scattering angles is equal to the FOV of the AisaEAGLE and the part of the scattering phase function that is covered by the measurements is defined by the solar zenith angle θ_0 (see Fig. 3.12b). For both extreme cases ($\Delta\varphi = 0°$, $\Delta\varphi = 90°$), Fig. 3.12 illustrates and Tab. 3.3 quantifies the detectable scattering angle range as a function of the solar zenith angle θ_0. The given values are representative for measurements with a $36.7°$ lens, as it was used for the ground-based measurements from the CARRIBA campaign, presented in Sect. 4.1. Here, in terms of comparability, the $36.7°$ lens is also applied for the listed airborne calculations, although during VERDI a $36.3°$ lens was applied.
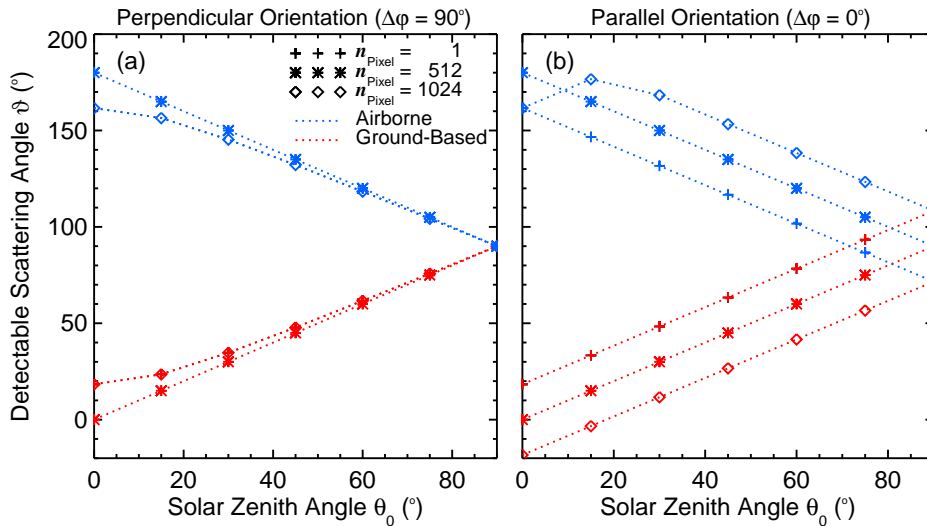
Figure 3.12: Scattering angle range that can be detected from ground-based and airborne AisaEAGLE measurements of the solar spectral radiance $I_\lambda^\downarrow$ and $I_\lambda^\uparrow$. The values are representative for a $36.7°$ lens and exemplarily depicted for the first, the central and the last spatial pixel, while the orientation of the AisaEAGLE sensor line is set **(a)** perpendicular ($\Delta\varphi = 90°$) and **(b)** parallel ($\Delta\varphi = 0°$) to the direction of the solar azimuth angle φ.

The values listed in Tab. 3.3 reveal that for the special case of $\theta_0 = 0°$, the detectable scattering angle range is equal for measurements perpendicular or parallel to the direction of the solar azimuth angle φ. However, for this special case the instruments inlet would have to be pointed exactly into the direction of the Sun (ground–based application). Those measurements would then very likely be overexposed unless the cloud optical thickness is not exceeding a value of $\tau = 10$. Due to the strong forward scattering peak of ice crystals, this threshold could be even to small for cirrus. However, a cirrus with an optical thickness in that range is rather rare. Therefore, the pointing direction of the instruments inlet needs

to be different from the Sun's position. Doing so, the detectable scattering angle range is rapidly decreasing for a perpendicular orientation of the sensor line ($\Delta\varphi = 90°$); a parallel orientation is advisable ($\Delta\varphi = 0°$).

Table 3.3: Scattering angle range that can be detected from AisaEAGLE measurements of solar spectral radiance $I_\lambda^\downarrow$ and $I_\lambda^\uparrow$. The values are representative for a 36.7° lens and exemplarily depicted for the first, the central and the last spatial pixel. The orientation of the sensor line is set perpendicular ($\Delta\varphi = 90°$) or parallel ($\Delta\varphi = 0°$) to the direction of the solar azimuth angle φ.

$\Delta\varphi(°)$	$\theta_0(°)$	$\vartheta_{\text{Pixel 1}}(°)$		$\vartheta_{\text{Pixel 512}}(°)$		$\vartheta_{\text{Pixel 1024}}(°)$		Total ϑ Range (°)	
		GB	AB	GB	AB	GB	AB	GB	AB
0	0	18.35	161.65	0	180	(-)18.35	161.65	36.7	18.35
0	15	33.35	146.65	15	165	(-)3.35	176.65	36.7	30.0
0	30	48.35	131.65	30	150	11.65	168.65	36.7	36.7
0	45	63.35	116.65	45	135	26.65	153.35	36.7	36.7
0	60	78.35	101.65	60	120	41.65	138.35	36.7	36.7
0	75	93.35	86.65	75	105	56.65	123.35	36.7	36.7
0	90	108.35	71.65	90	90	71.65	108.35	36.7	36.7
90	0	18.35	161.65	0	180	18.35	161.65	36.7	36.7
90	15	23.53	156.46	15	165	23.53	156.46	17.1	17.1
90	30	34.71	145.28	30	150	34.71	145.28	9.42	9.42
90	45	47.84	132.16	45	135	47.84	132.16	5.68	5.68
90	60	61.67	118.33	60	120	61.67	118.33	3.34	3.34
90	75	75.78	104.22	75	105	75.78	104.22	1.56	1.56
90	90	90.00	90.00	90	90	90.00	90.00	0.00	0.00

4 Subtropical Cirrus - Ground-Based Observations

To analyze cirrus inhomogeneities, fields of cirrus optical thickness τ_{ci} are used. In the following the approach to derive these fields of τ_{ci} from ground-based measurements of downward spectral radiance $(I_\lambda^\downarrow)$ fields is introduced. Those fields of $I_\lambda^\downarrow$ were collected with the AisaEAGLE imaging spectrometer during the CARRIBA campaign, which is introduced in Sect. 4.1. Based on this measurements, a new method is presented to retrieve τ_{ci}. Section 4.4 shows that by comparing measured and simulated $I_\lambda^\downarrow$ as a function of scattering angle ϑ, some evidence of the prevailing cirrus crystal shape is obtained. Subsequently, this shape is used to substantiate the retrieval of τ_{ci}, for which a first analysis regarding cloud inhomogeneities is applied in Sect. 4.5. The sensitivity of the retrieval method with respect to surface albedo, effective radius (r_{eff}), cloud altitude and ice crystal shape is quantified in Sect. 4.6. Parts of this chapter have been published in Schäfer et al. (2013).

4.1 CARRIBA (Clouds, Aerosol, Radiation, and tuRbulence in the trade wInd regime over BArbados)

In April 2011, the second campaign of the CARRIBA project was performed in Barbados. The measurements were characterized by consistent meteorological conditions in the trade wind regime with regular occurrence of high ice clouds (Malkus, 1954, 1956, 1958; Siebert et al., 2013; Werner et al., 2013). The aim of CARRIBA was to investigate microphysical and radiative processes within and next to shallow trade wind cumuli by helicopter-borne and ground-based observations (e.g. Siebert et al., 2013; Werner et al., 2013, 2014). However, also cirrus has frequently been observed by the ground-based instrumentation.

During CARRIBA, the imaging spectrometer AisaEAGLE was located in the **B**arbados **C**loud **O**bservatory (BCO; Stevens et al., 2015) of the Max Planck Institute for Meteorology (Hamburg, Germany) at Deebles Point (13.15° N, 59.42° W), a cape at the East coast of Barbados. Figure 4.1 shows a map with the location of the BCO and the setup of the station.

Measurements with a Raman LiDAR and a cloud radar as well as radiosonde data are available from the same site. Table 4.1 lists the instruments installed at the BCO and their most relevant specifications. In parallel to the AisaEAGLE radiance measurements, all-sky images were collected every 15 s to monitor the cloud situation (cloud coverage, cloud type, heading). Downward spectral radiance was measured under inhomogeneous cloud cover on 14 different days. Each day, two hours of data were collected in parallel to the helicopter flights.

Figure 4.1: Site of the AisaEAGLE radiance measurements during the CARRIBA campaign at Deebles Point on the east coast of Barbados.

Table 4.1: Instrumentation at the BCO during CARRIBA. Only those instruments and measured quantities are listed, which contributed to the data analysis within the scope of this thesis.

Instrument	Measured Quantity	Unit	Range
AisaEAGLE	Radiance	$W\,m^{-2}\,nm^{-1}\,sr^{-1}$	$\lambda = 400$–$970\,nm$
CANON Camera	RGB Radiance	$W\,m^{-2}\,nm^{-1}\,sr^{-1}$	$\lambda = (446,530,591)\,nm$
Raman LiDAR	Cloud Altitude	m	$z = 0$–$15\,km$
	Cloud Phase		Cloud Free, Liquid, Ice
Ceilometer	Cloud Base Altitude	m	$z = 0$–$15\,km$, $\Delta z = 15\,m$
Radiosonde	Air Pressure	hPa	
	Temperature	$^\circ C$	
	Relative Humidity	%	
	Wind Field	$m\,s^{-1}$, $^\circ$	

While trade wind cumuli were not always present, cirrus clouds were observed during each measurement. In the following, four measurement cases are evaluated with only cirrus clouds to exclude any radiative effects by low cumuli. During CARRIBA, a lens with an opening angle of AisaEAGLE of about 36.7° was mounted. With regard to the slow movement of the cirrus, a sufficient frame rate of 4 Hz was used. The integration time was chosen between 10 and 30 ms, depending on the illumination of the cloud scene.

4.2 Method to Retrieve Cirrus Optical Thickness

For the retrieval of τ_{ci} from the measured downward spectral radiance $I_\lambda^\downarrow$ transmitted through the cirrus, radiative transfer calculations are performed. The radiative transfer solver DISORT 2 (**DIS**crete **O**rdinate **R**adiative **T**ransfer) is applied. Input parameters such as cloud optical properties, aerosol content and spectral surface albedo are provided by the **lib**rary for **Rad**iative **tran**sfer calculations (*libRadtran*, Mayer and Kylling, 2005). The HEY parameterization (**H**ong **E**mde **Y**ang; Yang and Liou, 2000) is used to describe

the scattering properties of ice crystals. It uses pre-calculated ice cloud optical properties including full phase matrices generated with the models by Yang and Liou (2000).

The simulations are performed at 530 nm wavelength. This wavelength is chosen to match the wavelength of the LiDAR measurements at BCO. Since BCO is located at the far end of this cape, the measurement site is surrounded by water, rocks and grass. For simplification the surface albedo in the radiative transfer simulations is assumed to be only water, as derived by Wendisch et al. (2004), providing a value of 0.068. *libRadtran* supplies calculated Mie tables for rural, maritime, urban and tropospheric aerosol size distributions given in Shettle (1989). Because the measurements were performed in the vicinity of the coast, the maritime type is chosen as aerosol input for *libRadtran*. The cloud altitude and vertical extent is determined from the LiDAR measurements performed at BCO, see Fig. 4.2.
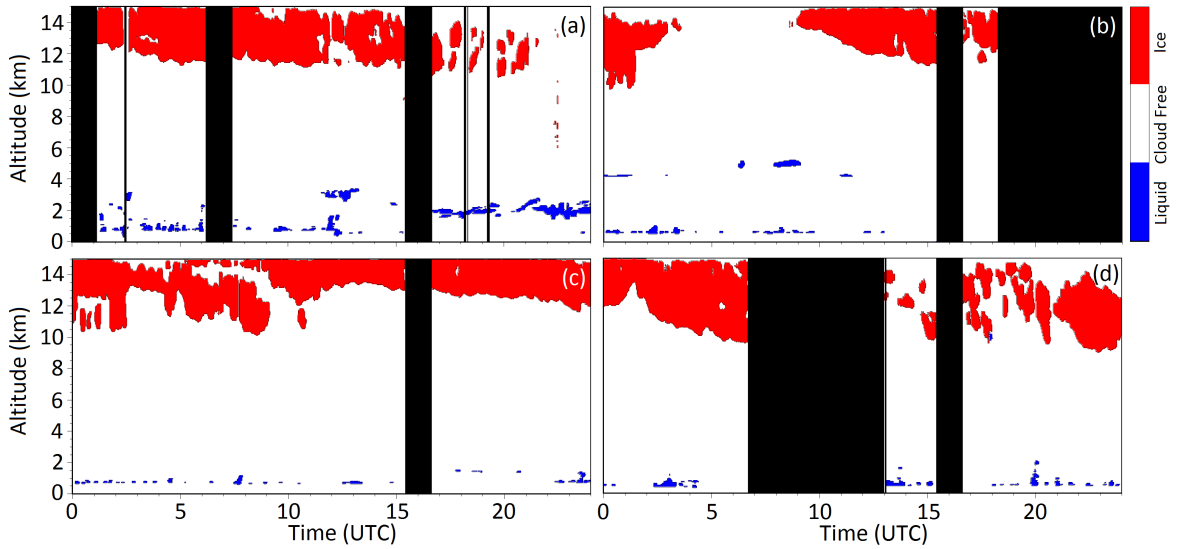

Figure 4.2: Cloud masks derived from LiDAR measurements at the BCO with 10 min temporal resolution for **(a)** 9 April 2011, **(b)** 16 April 2011, **(c)** 18 April 2011, and **(d)** 23 April 2011. Black colored areas mark data gaps. Separation in liquid water clouds (blue), ice clouds (red), and cloud free areas (white) with a vertical accuracy of 60–660 m depending on the altitude.

For the simulations, a fixed r_{eff} has to be defined as no direct retrieval from AisaEAGLE is possible. For this, a value of 20 μm is assumed. The assumed r_{eff} is taken from MODIS data (Collection 5) as estimate for the clouds in the area close to BCO. *libRadtran* adapts the IWC with respect to the prescribed r_{eff} and simulated τ_{ci} (Mayer, 2005). Therefore, a direct retrieval of the IWC is not possible, because the method is not sensitive to r_{eff}. Furthermore, the imaging measurements require an accurate description of the sensor geometry in the simulations as shown in Fig. 3.11. The sensor was aligned horizontally. The sensor azimuth angle was not measured directly but estimated from measurements during the time when the Sun's azimuthal position was in the direction of the sensor line. If both azimuth angles are equal, the measurements will be overexposed with a distinct maximum. The sensor azimuth angle is derived from the time of that maximum. The viewing zenith angle is given by the sensor FOV, which is $\beta = \pm 18°$. Related to this range, the downward solar radiance $I^{\downarrow}_{\lambda,cal}$ is calculated for angles with 0.3° steps.

Using these input parameters, downward solar radiance $I^{\downarrow}_{\lambda,\mathrm{cal}}$ is simulated as a function of τ_{ci}. The simulations are performed for the FOV of AisaEAGLE over the period of each measurement. Thus, a simulated grid (look–up table, LUT) of possible radiances and corresponding τ_{ci} is available for each time stamp of the measurement and each spatial pixel. The retrieved τ_{ci} is derived by linear interpolation of the simulated radiances from the LUT to the measured value for each spatial pixel.

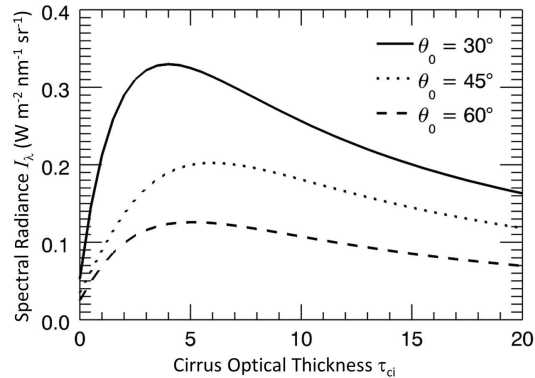**Figure 4.3:** Simulated radiance at $530\,\mathrm{nm}$ as a function of τ_{ci} for different solar zenith angles.

Figure 4.3 exemplifies radiance simulations for the solar zenith angles of 30, 45, and $60°$, a solar azimuth angle of $90°$, and a cirrus with ice crystals in the shape of solid columns. The base of the cirrus is at $11\,\mathrm{km}$ altitude. Figure 4.3 indicates that the retrieval of τ_{ci} is ambiguous. For example, at $\theta_0 = 30°$ a radiance of $0.2\,\mathrm{W\,m^{-2}\,nm^{-1}\,sr^{-1}}$ corresponds to τ_{ci} of either 1 or 15. Recently, Brückner et al. (2014) introduced a multispectral cloud retrieval method that avoids this ambiguity. Based on a method by McBride et al. (2011), it uses three ratios of transmitted radiance at visible and near-infrared wavelengths to create 3D LUT without ambiguity. However, currently the AisaEAGLE radiance measurements are restricted to the visible wavelength range. Thus, this method cannot be adopted yet. The ambiguity has to be considered using additional information of the estimated τ_{ci}. In the case of thin cirrus (τ_{ci} less than about 3–4), the retrieval results for low values of τ_{ci} must be used, for optically thicker cirrus the section for large τ_{ci} must be applied. Thus, independent knowledge of the expected range of τ_{ci} is important to avoid the ambiguity in the retrieval. During CARRIBA, this supplementary information was provided by all-sky images and LiDAR measurements. The all-sky images do not give a quantitative value of τ_{ci}, but they are evaluated qualitatively. An experienced observer is able to judge whether a given cloud has an optical thickness higher or lower than the maximum indicated in Fig. 4.3. All retrieved τ_{ci} presented within this study are in the range left of the maximum.

4.3 Measurement Cases

Four data sets from the CARRIBA project from different days are evaluated: 9, 16, 18 and 23 April 2011. These days showed persistent cirrus with no other clouds below. An overview of the main characteristics of the evaluated measurement periods is summarized in Tab. 4.2.

Table 4.2: Characteristics of the evaluated measurement periods.

Date	9 April	16 April	18 April	23 April
Label	C-01	C-02	C-03	C-04
Swath (km)	7.3	8.0	8.6	7.3
Length (km)	15.6	40.5	44.1	13.3
Start Time (UTC)	13:26	13:43	13:43	16:45
$\bar{\theta}_0$ (°)	36.7	28.6	28.5	14.5
Cirrus Heading	SW → NW	NW → SW	WSW → ESE	SSW → NNE
Appearance	inhomog.	homog.	homog.	inhomog.
Cloud Altitude (km)	11–15	12–15	13–15	11–14
$\bar{I}^{\downarrow} \pm \sigma_I$ (W m^{-2} nm^{-1} sr^{-1})	0.08 ± 0.02	0.11 ± 0.02	0.10 ± 0.03	0.16 ± 0.03
$\bar{\tau}_{\mathrm{ci}} \pm \sigma_\tau$	0.41 ± 0.17	0.28 ± 0.09	0.20 ± 0.03	0.05 ± 0.04
Covered ϑ Range (°)	35.1–47.1	32.6–37.9	21.2–48.2	12.2–36.3

Figure 4.4a–d show all-sky camera images from the beginning of the four cases. Within each image, the red arrow indicates the movement of the cirrus during the analyzed period. The heading is derived by comparing the position of clouds in the sequence of all-sky images (15 s time resolution). The blue box indicates the area covered by the AisaEAGLE radiance measurements, i.e. the area of cirrus, which is heading across the sensor line during the measurement period. Due to the fact that the AisaEAGLE was not orientated perfectly in perpendicular direction to the cirrus heading, the covered area is not a rectangle in most cases.
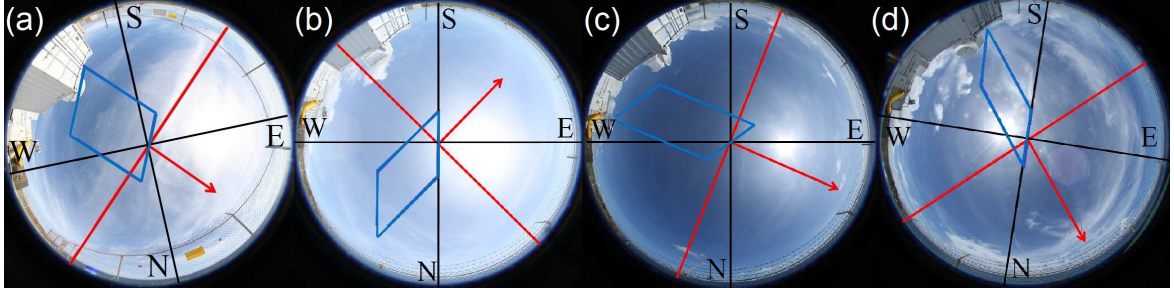

Figure 4.4: All-sky images from the beginning of the evaluated AisaEAGLE radiance measurements for **(a)** 9 April, **(b)** 16 April, **(c)** 18 April and **(d)** 23 April 2011 with the flow direction of the cirrus (red arrow) and FOV of the AisaEAGLE radiance measurements (blue). Orientation given by black lines and capital letters.

During all four measurement cases, τ_{ci} is estimated to be less than 3–4. That means that the ambiguity of Fig. 4.3 is avoided in all four cases. The cirrus field on 16 and 18 April was more homogeneous than that observed on 9 and 23 April. On 23 April, a 22° halo was identified on the all-sky images but unfortunately was not covered by the FOV of AisaEAGLE.

Fields of transmitted downward radiance $I_\lambda^{\downarrow}$ as measured by AisaEAGLE for the four cases are presented in Fig. 4.5. The radiance is given for 530 nm in 2D color-scale images for all 1024 spatial pixels on the abscissa and the time of measurement on the ordinate.
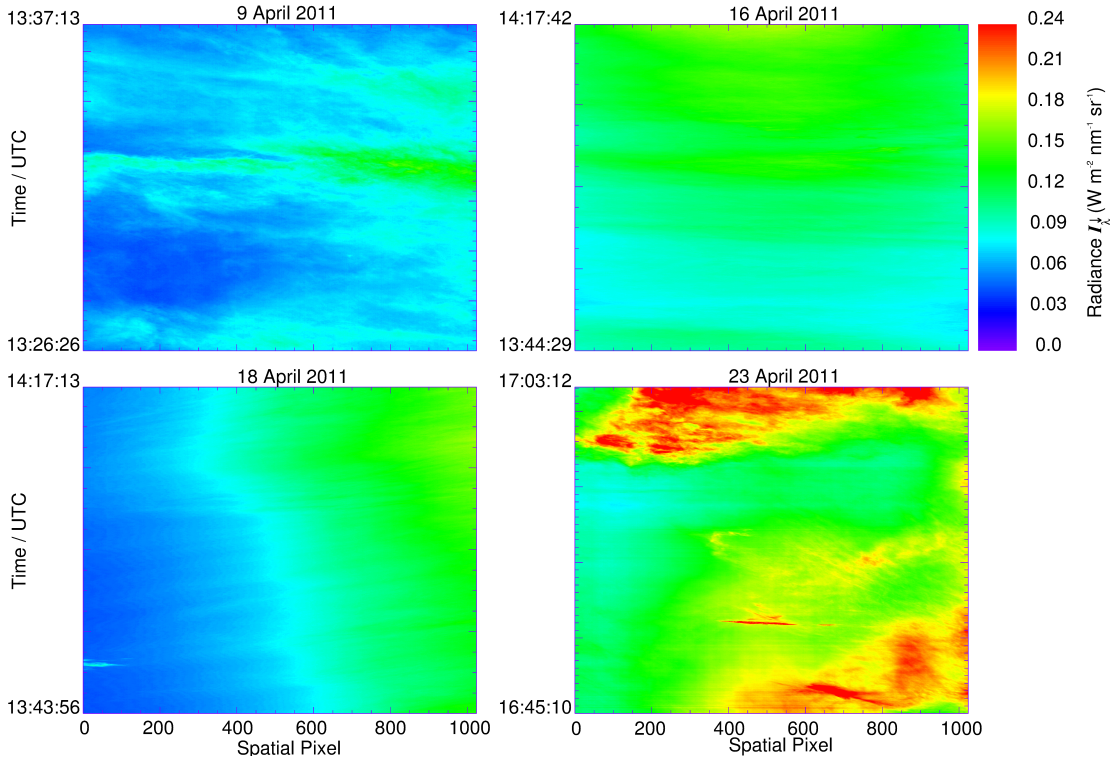
Figure 4.5: Two-dimensional images of the evaluated AisaEAGLE radiance measurements at 530 nm with the measured $I_\lambda^\downarrow$ (W m^{-2} nm^{-1} sr^{-1}) given in color scales.

The cloud structure seen in the all-sky camera images in Fig. 4.4a–d is imprinted in the radiance field. The average values $\bar{I}_\lambda^\downarrow$ of the measured radiance are given in Tab. 4.2. The highest value of $\bar{I}^\downarrow$ was observed on 23 April 2011 and the lowest on 9 April 2011.

Especially for 18 April 2011 it is evident that the image gets brighter from the left to the right side. During this day the sensor line of AisaEAGLE was orientated from North-West (pixel 1) to South-East (pixel 1024) while the Sun was in the East at the same time. This brightening is caused by enhanced scattering for small scattering angles, corresponding to the shape of the scattering phase function of ice crystals (see Fig. 4.6). Therefore, the radiative transfer calculations to retrieve τ_{ci} need to take into account the exact alignment of the sensor line and the exact position of the Sun. If the sensor orientation is carefully considered, the retrieval will account for this brightness effect caused by enhanced forward scattering by ice crystals.

Using the calculated scattering angles derived for each spatial pixel from Eq. (3.15), the $I_\lambda^\downarrow$ illustrated in Fig. 4.5 are now displayed as a function of scattering angle as shown in Fig. 4.7. The scattering angles are symmetrical for each pixel to the pixel closest to the Sun. If the Sun's azimuthal position is almost perpendicular to the sensor line, a minimum appears in the detected scattering angles per spatial pixel. In such cases, the plot of $I_\lambda^\downarrow$ as a function of the scattering angle would have overlapping sections. For clarity, one of those sections is assigned a negative sign in Fig. 4.5. Note that the images are not rectangular due to the movement of the Sun during the measurement period. The advantage of the
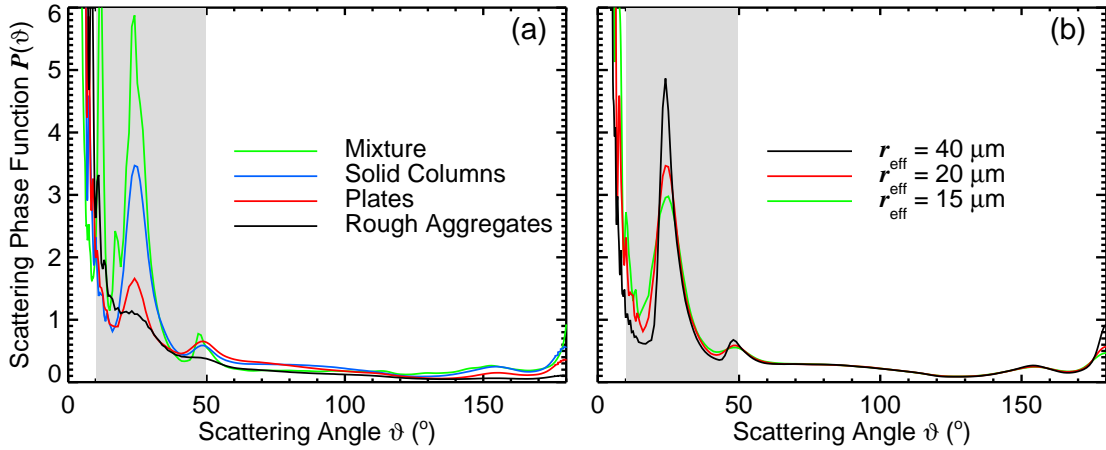
Figure 4.6: Scattering phase functions for **(a)** the different ice crystal shapes at 20 μm and **(b)** solid columns, calculated for the three effective radii for the retrieval in this study. The gray bar indicates the captured scattering angle range during the measurements.

illustration using scattering angles is that structures in the image related to the scattering phase function of the ice crystals occur in a fixed position throughout the time series, as can be seen for 18 April 2011. The radiance always increases with decreasing scattering angle, which is a typical characteristic of the forward scattering by cloud particles.

4.4 Retrieval of Ice Crystal Shape

The ice crystal shape is estimated from the directional distribution of radiance, considering the scattering phase function of different ice crystals. While on 9, 16 and 18 April no halo was visible, the 22° halo was observed on 23 April (compare Fig. 4.4). Thus, regular ice crystals like columns or plates must have been present on that day. For the first three cases, irregular ice crystals are more likely, because the crystals did not produce a halo. The directional scattering features are analyzed in detail with the AisaEAGLE measurements.

Figure 4.8 shows the average measured downward solar radiance $I_\lambda^\downarrow$ and its standard deviation as a function of the scattering angle ϑ for 18 April 2011. The standard deviation depends on the scattering angle and is calculated in intervals of $\Delta\vartheta = 0.3°$. Additionally, Fig. 4.8 includes simulations of downward solar radiance for different values of τ_{ci} and different ice crystal shapes. Figure 4.8a shows that for simulations assuming rough aggregates, no halo appears in the calculated radiance. However, for calculations with solid columns, plates as well as a mixture of ice crystals, the two halo regions are well defined in the simulation results. Furthermore, the best agreement between simulated and measured downward radiance $I_\lambda^\downarrow$ is found for rough aggregates. For this reason, the τ_{ci} for 18 April 2011 is retrieved by assuming rough aggregates for the ice crystal shape in Sect. 4.5.

A similar analysis for 23 April 2011 is presented in Fig. 4.9. Enhanced radiance is measured at scattering angles between 22 and 26°, which indicates the presence of a 22° halo. The halo is quite hard to identify in Fig. 4.7 due to the cirrus inhomogeneities and probably
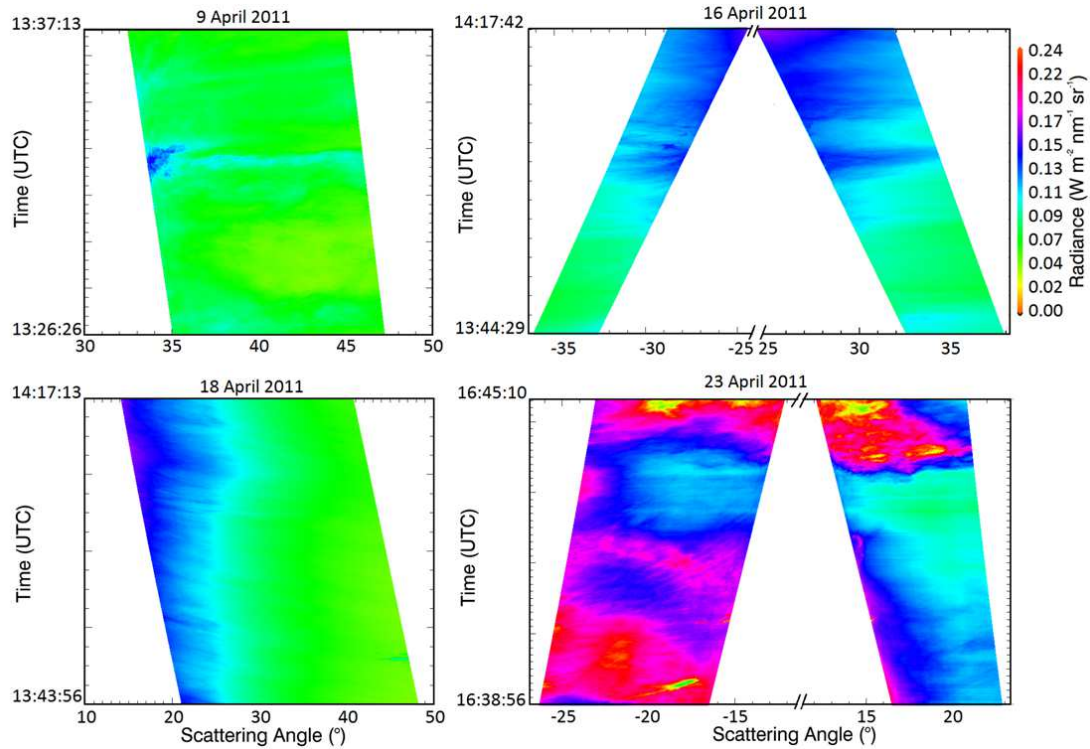
Figure 4.7: Time series of the measured downward solar radiance $I_\lambda^\downarrow$ during the four measurement cases as a function of scattering angle for each spatial pixel. The range of the abscissa of each image is fitted to the corresponding range of covered scattering angles.

a mixture of shapes. Therefore, the halo is quite weak. The averaged radiance displayed in Fig. 4.9 confirms this. The halo can be seen in the averaged data. However, due to the low τ_{ci} of 0.2, the maximum of the enhanced radiance within the halo region is relatively low. Concerning the ice crystal shape, best agreement is found for a mixture of different ice crystal shapes, while for aggregates the mismatch of the halo is obvious. A retrieval of the ice crystal shape is difficult because the cirrus was very inhomogeneous, as indicated by the high standard deviation. The variability of the radiances is about $\pm 0.03\,\mathrm{W\,m^{-2}\,nm^{-1}\,sr^{-1}}$, which corresponds to a deviation of $20\,\%$ to the mean value. Therefore, the radiance fluctuations cannot be related to the scattering phase function. Considering that the analyzed sequence on 23 April is short, with only about 6 minutes duration, it is more likely that changes of τ_{ci} account for the structure in the radiance. Therefore, in the following retrieval of the τ_{ci} for 23 April 2011, ice crystals in the shape of solid columns (default setting in *libRadtran*) are assumed.

For 9 and 16 April 2011 the retrieval of the ice crystal shape within the cirrus is not possible. Due to the geometry (wind direction, sensor alignment, solar position), only a narrow range (32–$47°$, 25–$37°$) of scattering angles outside the $22°$ halo range is observed and the clouds are too inhomogeneous. The detected scattering angles just cover the edge of the halo regions. Therefore, the radiative transfer calculations to retrieve the τ_{ci} in Sect. 4.5 are performed for solid columns. An estimate of uncertainties related to the shape assumption is provided in Sect. 4.6.
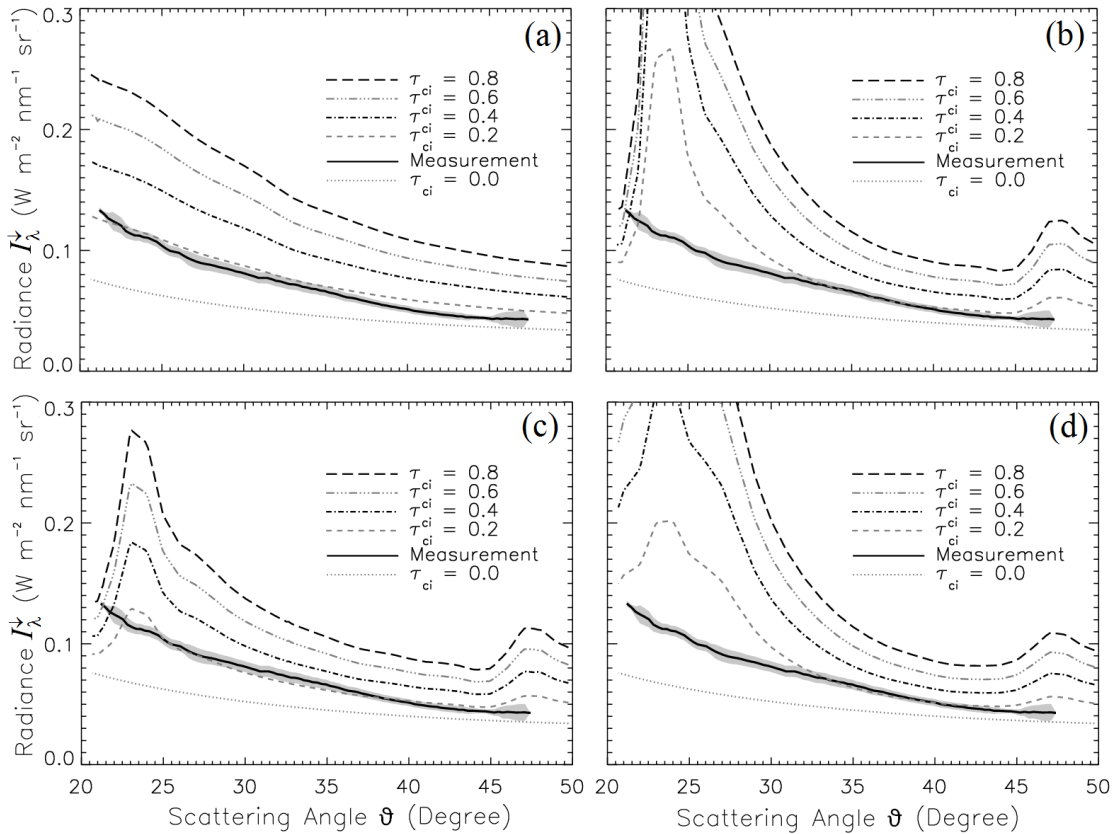
Figure 4.8: Measured and simulated $I_\lambda^\downarrow$ as a function of scattering angles. The standard deviation of the measurement is represented by the gray shade. Measurements are from 18 April 2011. The simulations were performed for different τ_{ci} and an assumed ice crystal shape of **(a)** rough aggregates, **(b)** solid columns, **(c)** plates, and **(d)** mixture.

4.5 Retrieval Results for Cirrus Optical Thickness

The τ_{ci} retrieved by the presented method are displayed in Fig. 4.10. The measurement time and the pixel number are converted into distances along and across the swath. For this, the altitude of the cloud base is used to derive the values for the abscissa. The average wind velocity in that altitude, derived from the **HY**brid **S**ingle-**P**article **L**agrangian **I**ntegrated **T**rajectory (HYSPLIT) model provided by the **A**ir **R**esources **L**aboratory (ARL) of NOAA, is used to convert the ordinate into a unit of distance. For 18 April 2011 the retrieved τ_{ci} indicates that the cloud is quite homogeneous. This confirms that the observed increase in radiance (Figs. 4.5 and 4.7) results from enhanced forward scattering of ice crystals and has been considered correctly by the model. For the other measurement cases, inhomogeneous cirrus is observed with large areas of cloudless regions in between.

Figure 4.11 shows frequency distributions of the retrieved τ_{ci}. They are normalized by the total of the retrieved τ_{ci} with a bin size of 0.01 in τ_{ci}. The largest τ_{ci} are found for 9 April 2011 (peak at $\tau_{ci} = 0.35$), the smallest for 23 April 2011 (peak at $\tau_{ci} = 0.05$). The frequency distributions for 16 and 18 April 2011 show peaks at τ_{ci} close to each other (peaks at $\tau_{ci} = 0.20/$
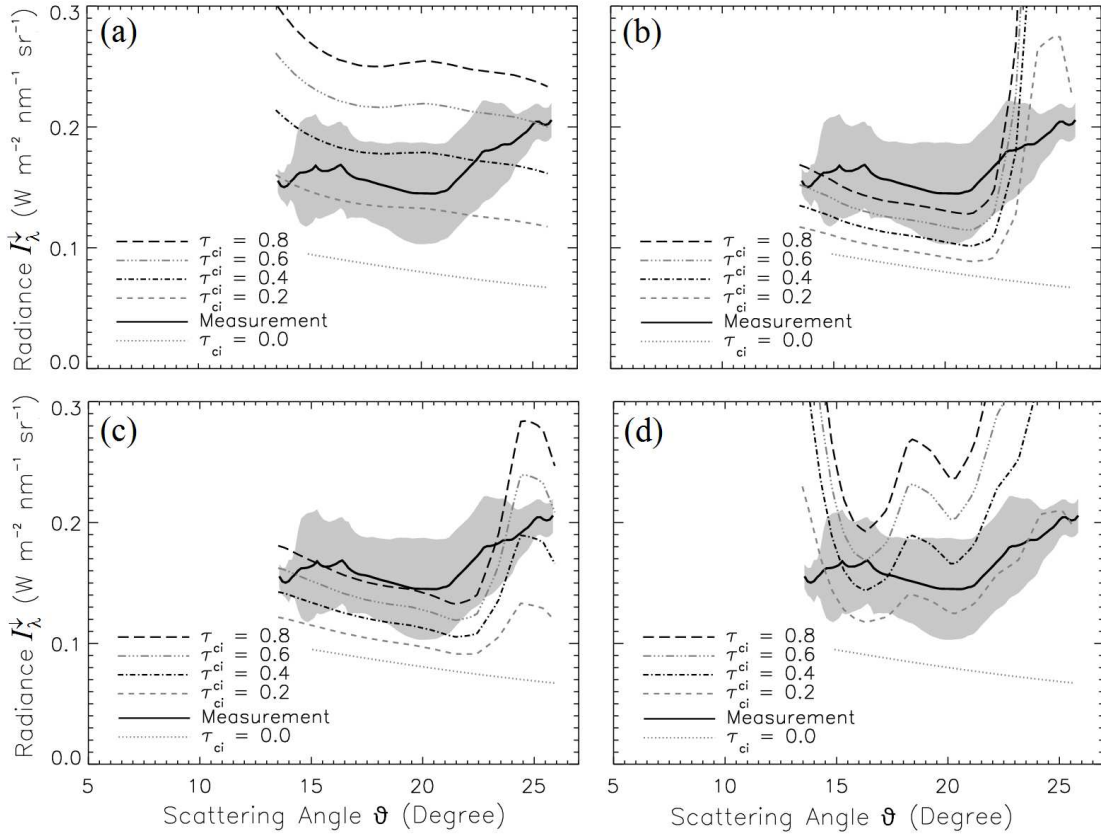
Figure 4.9: Measured and simulated $I_\lambda^\downarrow$ as a function of scattering angles. The standard deviation of the measurement is represented by the gray shade. Measurements are from 23 April 2011. The simulations were performed for different τ_{ci} and an assumed ice crystal shape of **(a)** rough aggregates, **(b)** solid columns, **(c)** plates, and **(d)** mixture.

0.25). Main differences are related to the number and width of the modes. The frequency distribution for 9 April 2011 is comparatively broad ($\tau_{ci} = 0.0$–1.0) and clearly has a bimodal shape (second smaller peak at $\tau_{ci} = 0.2$). The frequency distribution from 16 April 2011 is broad as well ($\tau_{ci} = 0.1$–0.7) with a tendential bimodal shape (second undefined peak at $\tau_{ci} = 0.15$). In contrast, the frequency distributions for 18 April 2011 and 23 April 2011 are narrow ($\tau_{ci} = 0.15$–0.3/ 0.0–0.25) and monomodal. Broader frequency distributions and bimodal shapes are an indication for inhomogeneous cloud structures.

The average and standard deviation of the retrieved τ_{ci} are a further indication for the inhomogeneity of a cloud situation. High standard deviations compared to the average values indicate a larger heterogeneity of the detected cloud situation. The particular values for each measurement case are listed in Tab. 4.2. Although the frequency distribution for 23 April 2011 shows a narrow peak compared to the other cases, the standard deviation reveals that this case was rather inhomogeneous, generated by the mix of cloudless and cloudy parts. Thus, in comparison, the cirrus on 16 and 18 April 2011 were more homogeneous than those on 9 and 23 April 2011. A more detailed analysis of the cirrus inhomogeneities including a statistical evaluation based on inhomogeneity parameters and an evaluation regarding their horizontal distribution is presented in Chapter 6.
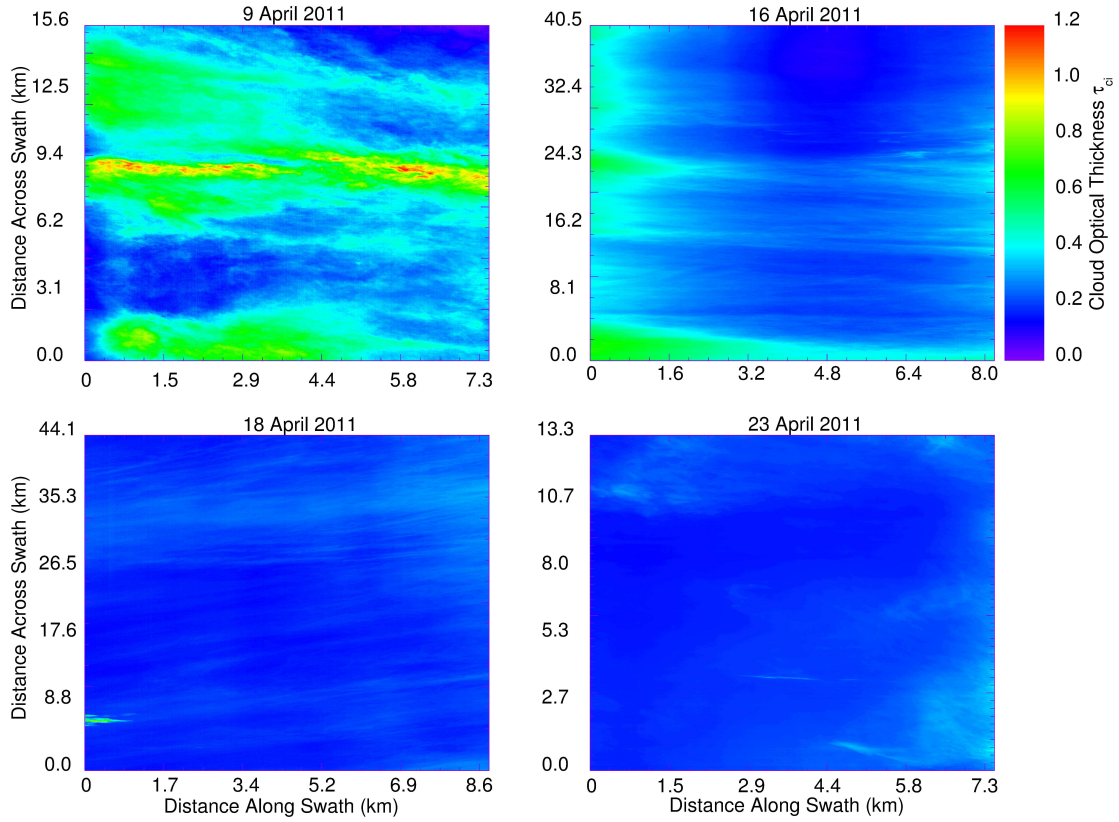
Figure 4.10: Time series of the retrieved τ_{ci} during the four measurement cases for each spatial pixel. Abscissa and ordinate values are different due to different measurement conditions.

4.6 Sensitivity Study

A sensitivity study is performed to quantify the retrieval uncertainties with regard to the assumptions made on the model input parameters. Uncertainties regarding the surface albedo, effective radius, cloud base altitude, and ice crystal shape are tested. Only one of those parameters is varied at one time and all other input parameters of the benchmark retrieval are kept constant. The benchmark case uses a surface albedo of water (0.068 at 530 nm wavelength), but AisaEAGLE was also surrounded by grass and sand and not just water. To quantify the resulting uncertainties, the retrieval is repeated for a surface albedo of grass and sand (0.073 and 0.314 at 530 nm wavelength; Feister and Grewe, 1995). The effective radius r_{eff} is assumed to be 20 µm in the benchmark retrieval. The sensitivity study is performed for 15 and 40 µm. This range is estimated from MODIS measurements for the time of the four measurement cases. The τ_{ci} was too low to be detectable by MODIS during the period of the presented measurements. Therefore, the surrounding regions of Barbados are used to derive the range of the effective radii. Another source of uncertainties is the cloud base altitude. For the sensitivity study the cloud is lifted 4 km upward and 4 km downward. For ground–based measurements and with no in situ observations available it is impossible to determine the preferred cirrus crystal shape. While solid columns are assumed in the benchmark retrieval, the sensitivity study is performed with plates and rough aggregates.
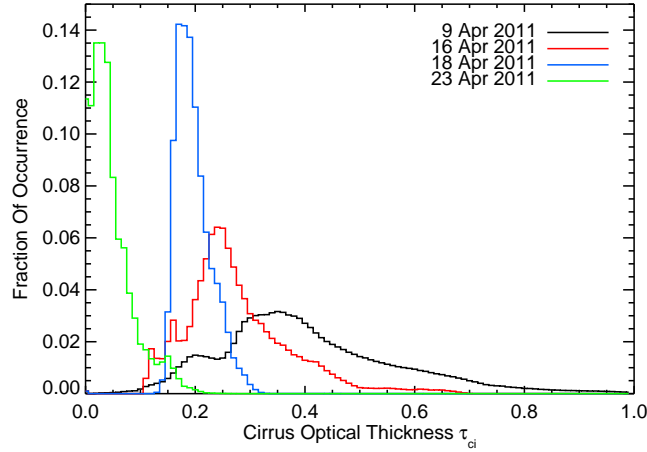
Figure 4.11: Normalized frequency distributions of τ_{ci} for each of the four measurement cases. The bin size is 0.01 units of τ_{ci}.

The sensitivity is expressed as the relative difference between the results, calculated using the average values of τ_{ci} (indicated by $\bar{\tau}_{ci}$):

$$\Delta \bar{\tau}_{ci} = 100\,\% \cdot \left(\frac{\bar{\tau}_{ci,BM} - \bar{\tau}_{ci}}{\bar{\tau}_{ci,BM}} \right) \tag{4.1}$$

Table 4.3 gives the different averages over the entire scene, Fig. 4.12 shows the uncertainties based on simulations. Radiances are simulated for τ_{ci} ranging from 0 to 0.5. The simulated radiances are then applied to the retrieval method where the benchmark properties are assumed. The differences between the benchmark retrieval and the sensitivity study vary in a range from less than one percent up to almost 90\,% as a function of the input parameters.

Table 4.3: Relative (%) and absolute difference of retrieved τ_{ci} in comparison to benchmark case.

	9 April		16 April		18 April		23 April	
	rel.	abs.	rel.	abs.	rel.	abs.	rel.	abs.
$\alpha_{surf} = 0.073$ (Grass)	2.6	0.01	0.4	0.00	0.6	0.00	0.25	0.00
$\alpha_{surf} = 0.314$ (Sand)	27.8	0.11	20.6	0.06	28.9	0.06	11.51	0.01
$r_{eff} = 15\,\mu m$	0.5	0.00	1.1	0.00	0.5	0.00	-0.54	-0.00
$r_{eff} = 40\,\mu m$	-4.9	-0.02	-3.9	-0.01	-0.9	-0.00	-0.06	-0.00
h_{cloud} (4 km Lower)	-0.45	-0.00	-0.28	-0.00	-0.14	-0.00	-0.06	-0.00
h_{cloud} (4 km Higher)	0.31	0.00	0.19	0.00	-0.05	0.00	0.05	0.00
Shape (Plates)	14.80	0.06	75.3	0.21	85.6	0.17	12.26	0.01
Shape (R. Aggr.)	23.3	0.09	26.1	0.07	33.1	0.07	17.11	0.01

Table 4.3 shows that for a surface albedo higher than the benchmark value, τ_{ci} will be overestimated. For a grass surface with a slightly larger albedo than water (0.073 compared to 0.068), the overestimation is still small. However, for simulations with a sand surface albedo (0.378), τ_{ci} shows a significant overestimation. With a maximum of almost 29\,% on
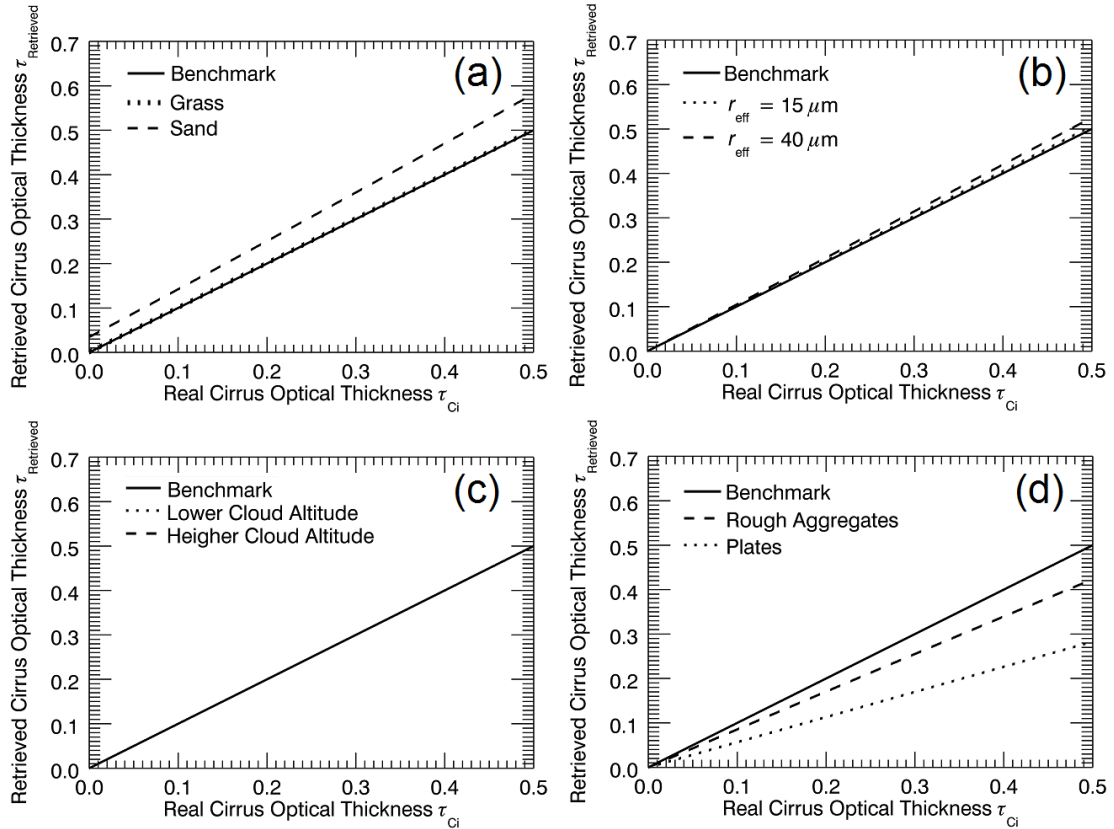
Figure 4.12: Retrieval results with regard to the sensitivity of **(a)** surface albedo, **(b)** effective radius, **(c)** cloud altitude, and **(d)** ice-crystal shape. Simulated for a solar zenith angle of $\theta_0 = 30°$, solar azimuth angle of $\varphi = 90°$, solid columns, 11–13 km cloud altitude, surface albedo of water and effective radius of $r_{\mathrm{eff}} = 20\,\mu\mathrm{m}$. The benchmark case represents the one-to-one line.

18 April 2011 and a minimum of around 12 % on 23 April 2011, the uncertainties are larger than those resulting from the measurement uncertainty. This indicates that the surface type has to be chosen correctly to enable accurate retrievals of τ_{ci}. Fig. 4.12a confirms this result. The retrieved τ_{ci} for the synthetic radiance above water and grass are almost identical. Compared to this, the retrieval result for a sand surface albedo shows larger values. The overestimation of up to 30 % seems to be relatively high; e.g. for very small τ_{ci} the percental difference can be quite large. However, the differences in the absolute values of τ_{ci} are only about ± 0.1 and lower. Furthermore, this sensitivity study represents an extreme case, as the grass at Deebles Point was patchy and rather dry, so the literature estimate for the sand surface albedo is on the high side.

The downward solar radiance $I_\lambda^\downarrow$ depends approximately linearly on the ice crystals r_{eff}. Here, a smaller r_{eff} yields an underestimation of the retrieved τ_{ci}. For larger r_{eff}, the retrieved τ_{ci} will be overestimated. From the differences listed in Tab. 4.3, linearity can be assumed. The absolute difference of $r_{\mathrm{eff}} = 40\,\mu\mathrm{m}$, referring to $r_{\mathrm{eff}} = 20\,\mu\mathrm{m}$, is four times higher than for $r_{\mathrm{eff}} = 15\,\mu\mathrm{m}$ referring to $r_{\mathrm{eff}} = 20\,\mu\mathrm{m}$. Approximately, this ratio is confirmed by the relative differences in Tab. 4.3. However, the relative differences are in a range below 5 % and the absolute values show no significant change. Comparing the scattering phase functions in

Fig. 4.6b reveals that they are quite similar at most detected scattering angles with the exception of the halo region and below $20\,°$. Since the differences between the scattering phase functions, calculated for different r_{eff}, appear mostly in the forward and backward scattering range but not in the captured scattering angle range, this explains the small variation found in the sensitivity study (Fig. 4.12b).

However, the contrast in the scattering intensity between $22°$ and the surrounding minima for the three r_{eff} in Fig. 4.6b is large. Thus, in the special case of solid columns as well as other hexagonal shapes, it is possible to estimate r_{eff} from the angular sampled spectral radiance data. Unfortunately, those regions of the scattering phase function were covered only twice during this study: on 18 April 2011 (with rough aggregates as the predominant ice-crystal shape) and on 23 April 2011 (highly inhomogeneous cirrus). Here, the r_{eff} cannot be retrieved: rough aggregates do not produce the $22°$ halo, and the cloud inhomogeneities on 23 April caused radiance fluctuations that exceeded the intensity of the $22°$ halo.

Regarding a varied cloud base altitude, no significant changes in the retrieved τ_{ci} are found. The differences for all four cases are below $1\,\%$. Therefore, possible uncertainties of the retrieved τ_{ci} due to the cloud base altitude can be neglected. This is reproducible from the retrieval results in Fig. 4.12c, which are congruent.

For the sensitivity test with regard to the cirrus crystal shape, Tab. 4.3 lists differences up to almost $90\,\%$. The retrieved τ_{ci} in Fig. 4.12d as well as the scattering phase functions in Fig. 4.6a confirm this statement. Compared to the other parameters, the retrieval results show larger differences to each other. This is related to differences in the scattering phase functions for the scattering angle range captured during the four measurement cases. In Fig. 4.12d the differences between the lines increase with increasing τ_{ci}. Using plates or rough aggregates instead of solid columns, τ_{ci} will be underestimated in both cases. The average of τ_{ci} is larger by up to 0.2. Compared to the average values of the detected τ_{ci} this is not negligible. Therefore, the ice-crystal shape is important to accurately retrieve the cirrus optical thickness from ground-based spectral radiance measurements.

Most of the scattering phase function features, which may help to identify the cirrus crystal shape, are related to the two halo peaks at $\vartheta = 22°$ and $\vartheta = 46°$. To investigate the scattering phase function in the range of the $22°$ halo, measurements at solar zenith angles θ_0 between 15 and $30°$ are advisable. To detect the $\vartheta = 46°$ halo, measurements at solar zenith angles θ_0 between 30 and $45°$ are most suitable (compare Tab. 3.3). To capture the largest possible scattering angle range around those features, the sensor line has to be placed along the direction of the solar azimuth angle φ_0.

5 Arctic Stratus - Airborne Observations

As Arctic stratus exhibits a different type of cloud, their microphysical and optical inhomogeneities are expected to differ significantly from those of cirrus. To investigate these inhomogeneities, fields of cloud optical thickness τ_{st} are retrieved from airborne upward radiance measurements of Arctic stratus. The data were collected with AisaEAGLE during the international field campaign VERDI, introduced in Sect. 5.1. The influence of the highly variable surface albedo introduces significant uncertainties to Arctic stratus cloud retrievals and has to be addressed. Based on airborne nadir reflectivity (γ_λ) measurements in the visible spectral range, Sect. 5.2 provides a method to discriminate sea ice and open water under cloudy conditions. In cloudy cases the transition of γ_λ from open water to sea ice is horizontally smoothed. In general, clouds reduce γ_λ above bright surfaces in the vicinity of open water, while γ_λ above open sea is enhanced. With the help of observations and 3D radiative transfer simulations, this effect and its horizontal range is quantified in Sect. 5.4. Furthermore, the influence of 3D radiative effects on the retrieved cloud optical properties is investigated in Sect. 5.5. For selected cases with regard to the findings from Sect. 5.3 to 5.5, Sect. 5.6 presents then the retrieval of τ_{st}. Parts of this chapter have been published in Schäfer et al. (2015).

5.1 VERDI (VERtical Distribution of Ice in Arctic clouds)

The international Arctic field campaign VERDI took place in Inuvik, Northwest Territories, Canada, in April and May 2012. The instruments (Tab. 5.1) were installed on Polar 5, an aircraft used for scientific research by the Alfred Wegener Institute Helmholtz Centre for Polar and Marine Research (AWI), Bremerhaven. During VERDI, Polar 5 was operated out of the Inuvik Mike Zubko Airport. Consistent with the Arctic cloud climatolgy presented by Shupe et al. (2011), the measurements during VERDI were characterized by persistent Arctic stratus and less occurrence of high ice clouds. Most flights were performed over the Beaufort Sea, partly covered by sea ice with open leads and polynias, which grew bigger towards the end of the campaign. Figure 5.1 summarizes all flight tracks during the VERDI campaign.

The measurement strategy during VERDI aimed at combining remote-sensing and in situ cloud observations. Therefore, the same clouds were subsequently sampled by a set of in situ (see Klingebiel et al., 2015) and remote-sensing instruments. The aircraft was equipped with an active and several passive remote-sensing systems. The active system was the Airborne Mobile Aerosol Lidar (AMALi; Stachlewska et al., 2010). It was operated in nadir viewing direction at 532 nm wavelength. Passive radiation measurements were carried out with the
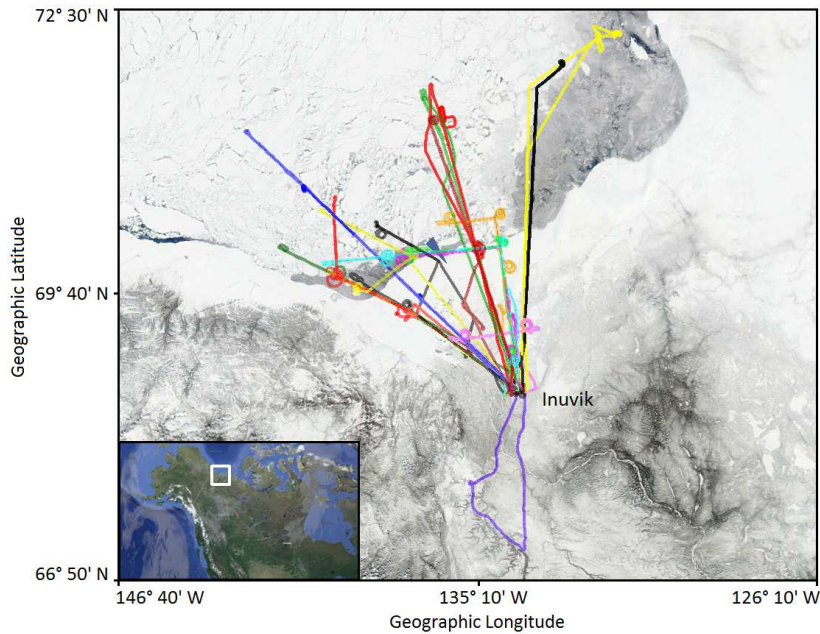
Figure 5.1: Flight tracks performed during the VERDI campaign and true-color MODIS image (Aqua; 250 m resolution) from 17 May 2012. Small inlet shows the location of the measurement area situated in north-west Canada.

imaging spectrometer AisaEAGLE, to investigate cloud inhomogeneities and to analyze the 2D radiative effects of ice edges in a cloudy atmosphere. A 2x2 binning was used to increase the frame rate to up to 30 Hz. With the remaining 512 spatial pixels, the single-line sensor provides a sufficiently high horizontal resolution to observe cloud inhomogeneities and ice edges in detail. The flight altitude during the remote-sensing legs was about 3 km above ground, which is about 2 km above cloud top for typical boundary layer clouds with cloud top altitudes at about 1 km. For this geometry, the width of one AisaEAGLE pixel at cloud top is 3.5 m and the length is 4.2 m at an exposure time of 10 ms and a flight speed of 65 m s^{-1}.

Further passive radiation measurements were carried out with the **S**pectral **M**odular **A**irborne **R**adiation measurement sys**T**em, initially designed for albedo measurements (SMART-Albedometer; Wendisch et al., 2001), and a Sun tracking photometer (Matsumoto et al., 1987). The SMART-Albedometer measures up-/downward spectral radiance I_λ and irradiance F_λ ($\lambda = 350$–2100, 2–16 nm FWHM). The Sun photometer covers aerosol optical thickness between $\lambda = 367$–1026 nm. The configuration was similar to that during the aircraft campaign SoRPIC described by Bierwirth et al. (2013). Drop sondes were used at selected waypoints to sample profiles of meteorological parameters (air pressure p, air temperature T, relative humidity RH) needed for the radiative transfer simulations to retrieve τ_{st}. Table 5.1 lists the instruments aboard Polar 5 and their relevant specifications.

The data from the AMALi and the drop sondes are used to determine the cloud-top altitude and geometrical thickness. The data from the SMART-Albedometer are used to validate the $I_\lambda^\uparrow$ measurements of AisaEAGLE. Furthermore, the SMART-Albedometer measurements of the downward irradiance $F_\lambda^\downarrow$ are used to transform the AisaEAGLE radiance $I_\lambda^\uparrow$ into the

Table 5.1: Instrumentation of the Polar–5 aircraft during the VERDI campaign. Only those instruments are listed, which contributed to the data analysis within the scope of this thesis.

Instrument	Measured Quantity	Unit	Range
AisaEAGLE	Radiance	$\mathrm{W\,m^{-2}\,nm^{-1}\,sr^{-1}}$	$\lambda = 400\text{–}1000\,\mathrm{nm}$
SMART - Albedometer	Radiance	$\mathrm{W\,m^{-2}\,nm^{-1}\,sr^{-1}}$	$\lambda = 350\text{–}2100\,\mathrm{nm}$
	Irradiance	$\mathrm{W\,m^{-2}\,nm^{-1}}$	$\lambda = 350\text{–}2100\,\mathrm{nm}$
AMALi	Extinction Coefficient	$\mathrm{m^{-1}}$	$\lambda = 355\,\mathrm{nm},\,532\,\mathrm{nm}$
	Cloud Top Altitude	m	$z = 0\text{-}3\,\mathrm{km}$
CANON Camera	RGB Radiance	$\mathrm{W\,m^{-2}\,nm^{-1}\,sr^{-1}}$	$\lambda = (446,530,591)\,\mathrm{nm}$
Sun Photometer	Aerosol Optical Depth	–	$\lambda = 367\text{–}1026\,\mathrm{nm}$
AVAPS Lite - Drop Sondes	Air Pressure	hPa	
	Temperature	°C	
	Relative Humidity	%	

nadir reflectivity γ_λ, which is a function of r_{eff} and τ_{st} (see Eq. (2.11)). The γ_λ are calculated at a wavelength of 645 nm, where scattering is dominant and shows a significant sensitivity to τ_{st} (Werner et al., 2013).

During all 15 flights throughout VERDI, 130 recordings (25 h, 11 min, 29 s) of reflected radiance from cloud-top and surface were collected with AisaEAGLE. 78 % of the observation time was spent above clouds. For 86 % of the cloud observations a cloud retrieval as described by Bierwirth et al. (2013) could not be applied as the surface albedo was high. Either snow-covered ice almost eliminated the contrast between cloud and surface, or a mixture of ice and open water made a cloud retrieval after Bierwirth et al. (2013) impossible. The latter occurred in 42 % of all observations and is analyzed in more detail to quantify the degree to which cloud retrievals are biased above heterogeneous surfaces.

5.2 Identification of Ice and Open Water

A typical scene showing a mixture of sea ice and open ocean surfaces covered by an optically thin stratus is presented in Fig. 5.2. The visible wavelength channels of the image provide no visible contrast between sea ice and cloud. This is why near-infrared channels are applied in MODIS cloud retrievals over sea ice. However, with AisaEAGLE the observations are limited to wavelengths below 1000 nm, where the contrast is weak (compare Fig. 5.5) and a retrieval of τ_{st} is not possible in those areas; it can only be performed above less reflecting water surfaces.

The limitation of AisaEAGLE in the case of bright surfaces is illustrated in Fig. 5.3 showing the calculated γ_λ at 645 nm wavelength for clouds with different values of τ_{st} over a dark ocean surface (blue lines) and a bright sea-ice surface (red lines). The calculations were
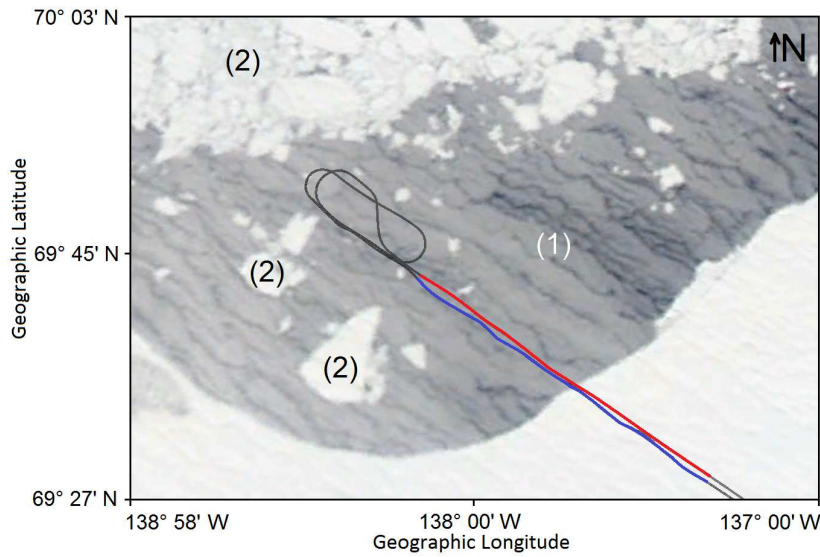
Figure 5.2: VERDI flight track and true-color MODIS image (Aqua; 250 m resolution) from 17 May 2012. Numbers (1) and (2) label open ocean and sea ice, respectively.

performed for different solar zenith angles θ_0 of 45, 60, and 75° (the range during VERDI measurements).

The upper panel shows that the separation of γ_λ for clouds of different τ_{st} above sea ice are not significant and far below the measurement uncertainties of most optical sensors. Therefore, a retrieval of τ_{st} based on 645 nm reflectivity is not possible. For the same clouds above a dark ocean surface, γ_λ is a strong function of τ_{st}, which is the basis of the cloud retrieval following the method by Nakajima and King (1990), Bierwirth et al. (2013), and Werner et al. (2013).

In order to select the dark-surface pixels for which a cloud retrieval is feasible, a sea-ice mask has to be derived. Figure 5.3 clearly shows that even for optically thick clouds γ_λ is significantly enhanced ($\geq 25\%$ at $\tau_{st} = 25$ and $\theta_0 = 60°$) above bright sea ice compared to a dark ocean surface. This gap can be used as a threshold to distinguish between measurements of clouds above the dark ocean surface and a bright sea ice surface. To define this threshold, it has to be considered that the differences between γ_λ measured above a dark ocean surface or a bright sea-ice surface is smaller for larger solar zenith angles and also decreases with increasing τ_{st} (lower panel of Fig. 5.3). However, the differences are still significant at large solar zenith angles of $\theta_0 = 60°$ and $\tau_{st} = 25$ (lower panel). For VERDI, where θ_0 was in the range of 55 to 75° for most of the observations, the particular threshold is defined as the center value between the two simulations:

$$\gamma_{\lambda,\text{thresh}} = \frac{\gamma_{\lambda,\text{ice}} + \gamma_{\lambda,\text{water}}}{2}. \tag{5.1}$$

To test this threshold, a section of a VERDI flight on 17 May 2012 (Fig. 5.2) was analyzed. The flight was divided into a leg A at 2920 m altitude above clouds (red in Fig. 5.2) and a leg B inside the cloud at 150 m altitude (blue in Fig. 5.2). The solar zenith angle was
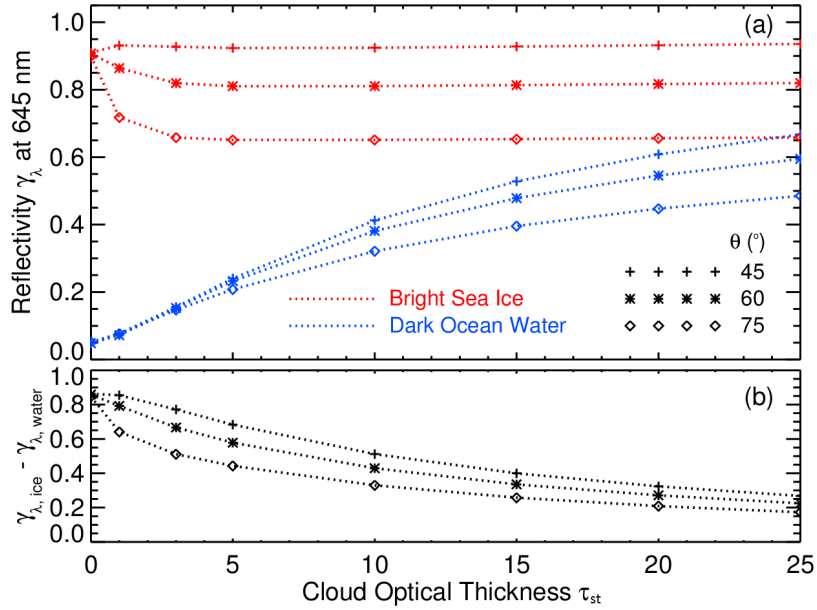
Figure 5.3: (a) Simulated γ_λ at 645 nm calculated for different τ_{st} ranging from 0 to 25 and cloud particles with a fixed r_{eff} of 15 µm. The calculations were performed for different θ_0 of 45, 60, and 75° over a highly reflecting ice surface and a dark ocean surface. (b) Difference between the simulated γ_λ over bright sea ice surface and dark ocean surface from (a).

$\theta_0 = 58°$. τ_{st} was obtained from AisaEAGLE measurements above open water far from the ice edge using the retrieval method presented by Bierwirth et al. (2013). An average value of $\tau_{st} = 5.3 \pm 0.5$ was derived, which agrees with the MODIS level-2 product showing values for τ_{st} between 0.02 and 15.5 ($\overline{\tau}_{st} = 3.6 \pm 2.5$) in the investigated area. In that case, the simulated $\gamma_{\lambda,ice} = 0.8$ and $\gamma_{\lambda,water} = 0.2$ from Fig. 5.3 give a threshold of $\gamma_{\lambda,thresh} = 0.5$.

Figure 5.4 shows a histogram of the measured γ_λ at 645 nm from leg A. There are two distinctly separated maxima, which correspond to measurements above bright sea ice and dark ocean. Either the minimum between the two maxima or the mean of those two most frequent values of γ_λ can be used as an alternative estimate of the threshold for the ice mask. In this particular case the threshold estimated from the frequency distribution is $\gamma_{\lambda,thresh} = 0.5$, which confirms the theoretical value derived from the radiative transfer simulations.

5.3 Quantification of 3D Radiative Effects from Measurements

Based on the thresholds, ice masks were created to identify measurements of clouds above sea ice for which the cloud retrieval by Bierwirth et al. (2013) cannot be applied. Figure 5.5 shows three examples of γ_λ derived from the nadir radiance and zenith irradiance measurements. Figures 5.5a and b show an extended ice edge, while Fig. 5.5c and d illustrate an accumulated ice floe field, observed on 17 May 2012 around 17:00 UTC ($\theta_0 = 58°$). As obtained from simultaneously performed AMALi measurements and data from the closest drop
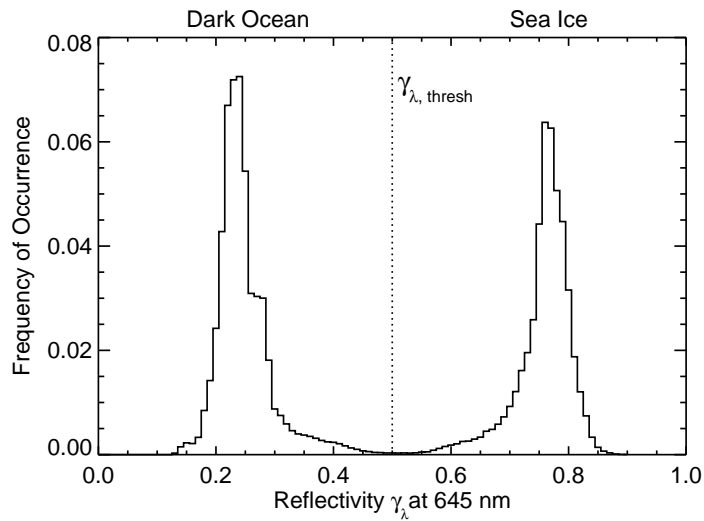
Figure 5.4: Fraction of occurrence of the measured γ_λ at 645 nm, given in the example of Fig. 5.5a. The bin size is 0.01.

sonde (Fig. 5.6), in both cases a cloud layer with cloud top at 200 m was observed between the ground and the aircraft. Figures 5.5e and f show ice floes without cloud cover, observed on 14 May 2012 at 21:00 UTC. The corresponding ice masks are shown on the right panel in Fig. 5.5. The pixels identified as sea ice are shown as red areas.

Figure 5.7 shows the frequency distributions for the three cases presented in Fig. 5.5 (solid black lines). All frequency distributions are normalized so that the maximum is 1. In each case, two maxima are separated by a distinct minimum, which defines the ice/water threshold value. For the cloudy cases in Fig. 5.7a and b the dark-surface peak is broadened asymmetrically towards higher γ_λ values, while the bright-surface peak is widened towards lower γ_λ values. For the clear-sky case in Fig. 5.7c, the peaks representing dark ocean and sea-ice surfaces are clearly separated.

To analyze the impact of the ice edge, frequency distributions for a selection of pixels far from the ice edge are included in Fig. 5.7 for each particular scene, separated into dark open-water pixels (dashed blue lines) and bright sea-ice pixels (dashed red lines). In Fig. 5.7a and b, the peaks of the selective frequency distributions are much sharper than the original peaks. For the clear-sky case in Fig. 5.7c, these selective frequency distributions are almost congruent with the single peaks of the entire frequency distribution. This means that in this case the ice edge has no impact on γ_λ of adjacent pixels, or in other words, there is no significant horizontal photon transport. Between the selected pixels far from the ice edge and the pixels directly over the ice edge are many pixels where γ_λ is enhanced (over open water) or reduced (over sea ice) compared to the values at the remote pixels. This particular enhancement and reduction of the measured γ_λ is most likely related to 3D radiative effects in clouds and the reflection between clouds and the surface. This influence of the ice edge on the pixels' reflectivity will most likely influence cloud retrievals based on 1D simulations in such scenes. To clarify this hypothesis, in the following those 3D effects are investigated by analyzing γ_λ with respect to the retrieved cloud optical properties. To characterize the magnitude
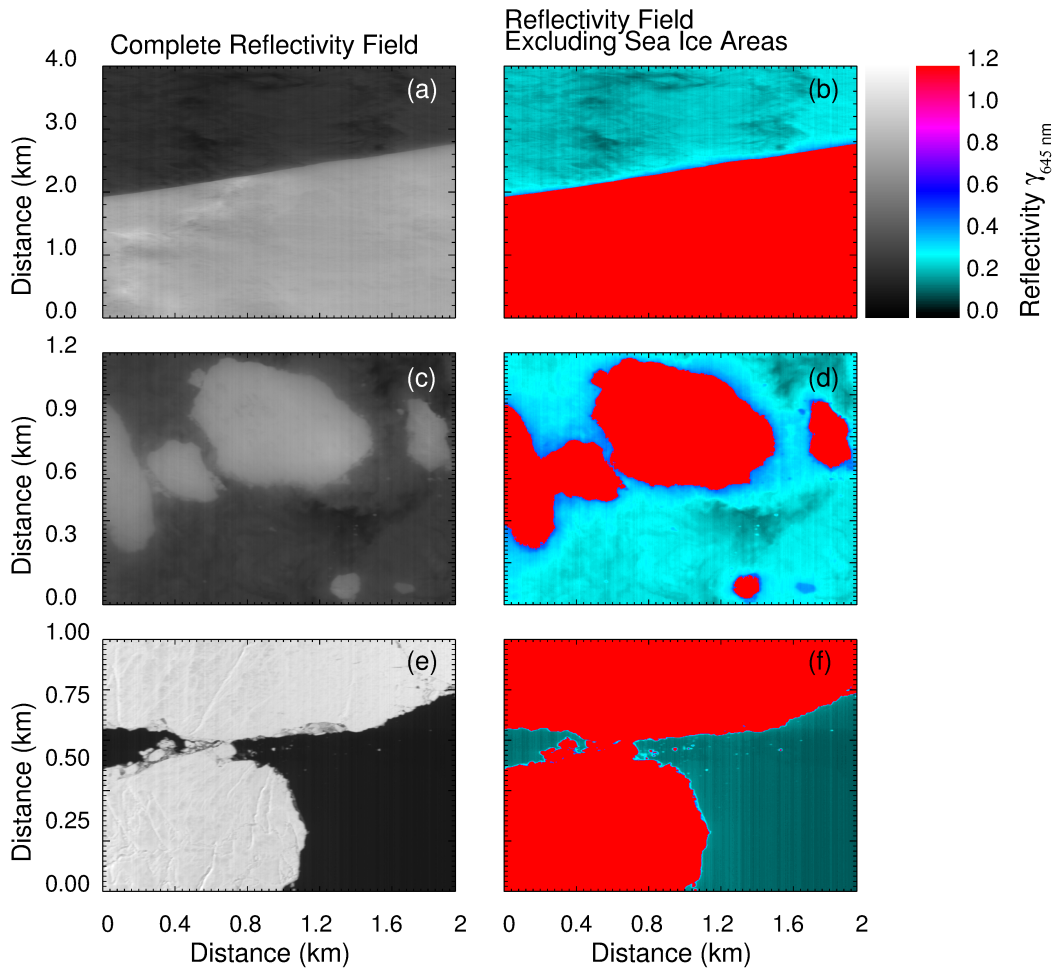
Figure 5.5: Left Side: Fields of γ_λ at 645 nm, measured with the imaging spectrometer AisaEAGLE. Right side: Same scenes as on the left side in color-scale and with ice mask overlay. The measurements were performed on 17 May 2012 during the international field campaign VERDI and show **(a), (b)** an overpass over a straight ice edge during cloudy conditions, **(c), (d)** an overpass over scattered ice floes during cloudy conditions, and **(e), (f)** an overpass over larger ice floes during cloudless conditions.

of the enhancement or reduction of the measured γ_λ, 3D radiative transfer simulations are performed in Sect. 5.4 and used to identify the most important parameters that control 3D effects. Afterwards, a 1D cloud retrieval is performed in Sect. 5.5 to quantify the influence of the 3D effects on the retrieved τ_{st} and r_{eff}.

Figure 5.8 illustrates the measured γ_λ (solid lines) and its standard deviation (dotted lines) as a function of the distance to the ice edge for the three scenes presented in Fig. 5.5. The maximum values measured over sea ice and dark ocean water differ between the cloudy and cloudless cases. This results from the different time of measurement and from the different patterns of the hemispherical-directional reflectance function (HDRF), which can be observed in nadir viewing direction over clouds and sea ice. In nadir viewing direction, the HDRF of clouds shows a minimum and increases with increasing observation angle. In contrast, the HDRF of sea ice shows approximately the same values for lower (nadir) and larger
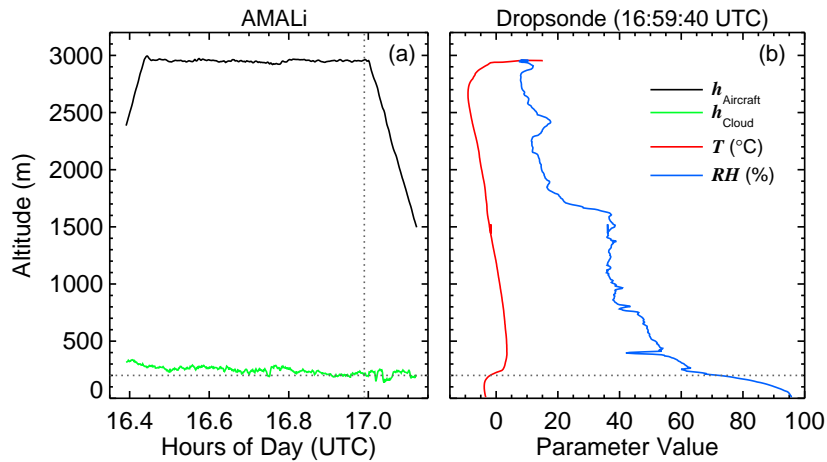
Figure 5.6: **(a)** Flight altitude h_{Aircraft} (black) and cloud top altitude h_{cloud} (green) derived from AMALi measurements aboard Polar 5 on 17 May 2012 with 5 s temporal resolution and 7.5 m vertical resolution. **(b)** Profiles of temperature T (red) and relative humidity RH measured with a drop sonde launched at 16:59:40 UTC. Dotted lines serve as reference lines and mark the cloud top altitude of $h_{\text{cloud}} = 200\,\text{m}$ and the start time of the drop sonde.

(limb) observation angles (Ehrlich et al., 2012). Compared to cloudy cases, this results in observations of larger γ_λ.

Furthermore, Fig. 5.8 shows that for the cloudy cases presented in Fig. 5.5a and c (red and blue in Fig. 5.8), close to the detected sea ice areas, a slight enhancement of γ_λ was measured over the open sea; while over the ice-covered area, γ_λ is reduced (indicated by arrows in Fig. 5.8). This results most likely from 3D radiative effects in clouds and the interaction between clouds and the surface. In this chapter, only the latter case is considered, namely, the 3D radiative effects related to the pathway of the photons between cloud and surface. Horizontal photon transport in the layer between surface and cloud smoothes the abrupt decrease of the surface albedo from large values above sea ice to low values above the open water. For measurements without clouds (Fig. 5.5f, green in Fig. 5.8) similar areas with enhanced γ_λ above the water close to the ice edge were not found.

The hypothesis linking the 3D radiative effect to the enhancement of γ_λ is illustrated in Fig. 5.9. The incident radiation ($F_0 \cdot \cos(\theta)$) impinges on the cloud, where scattering and absorption processes take place. Part of the incident radiation is transmitted through the cloud and scattered into the direction of the ice edge (bold black arrow). Sea ice acts similarly to a Lambertian reflector and reflects the incoming radiation almost uniformly in all directions (isotropic, gray arrows). The reflected radiation penetrates the cloud at a certain altitude (red or blue arrows), where parts of it are scattered into the observation direction. Without sea ice in the vicinity of the measurements, the reflected radiance would be influenced only by the cloud and dark ocean water. With sea ice in the vicinity, the measured nadir radiance $I_\lambda^\uparrow$ above the cloud parcel is enhanced due to the additional radiation reflected by the sea ice into the direction of the last scattering point in the cloud. This effect is significant only for cloudy cases, because of the weak scattering efficiency of the clear atmosphere compared to that of clouds. Comparing this effect for clouds of different
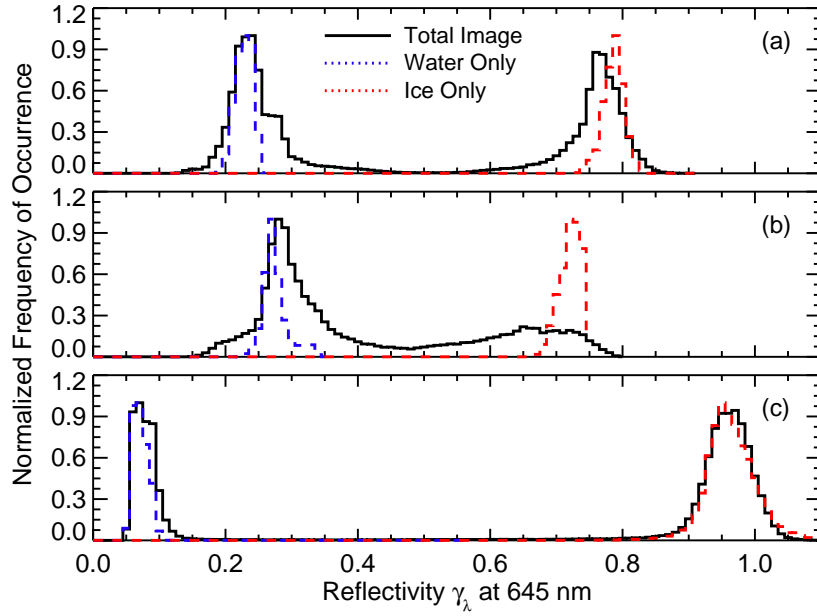
Figure 5.7: Normalized distributions of the frequency of occurrence of γ_λ measured during the three cases presented in Fig. 5.5. Additionally included are the frequency distributions over sea ice and dark ocean water only.

altitude (Fig. 5.9), the horizontal photon path of the reflected radiation is extended for clouds of higher altitude (compare for cloud A (red) and cloud B (blue)). Hence, the range of the 3D effect increases with cloud altitude.

For the case of the straight ice edge (Fig. 5.5a), the distances presented in Fig. 5.8 are almost in line with the flight track, which was perpendicular to the ice edge. With a frame rate of 30 Hz and an aircraft speed of $65\,\mathrm{m\,s^{-1}}$ this results in 700 measurements along the 1418 m for each of the 512 spatial pixels. The mean γ_λ measured along the flight path is illustrated as a solid red line in Fig. 5.8. In general, γ_λ decreases by about two thirds from $\gamma_\lambda = 0.75$ above bright sea ice to about $\gamma_\lambda = 0.25$ above dark ocean surface. The decrease does not occur sharply at the ice edge, but gradually starts at about 400 m distance from the ice edge and ends at 400 m distance from the ice edge over open water. In the cloudless case, the asymptotic values above sea ice and water are reached much closer to the ice edge at about 50 m.

Two distances are defined relative to the ice edge to quantify the enhancement effect. The first distance ΔL_{HPT} is introduced to quantify the range of horizontal photon transport. It characterizes the distance at which the transition from high $\gamma_{\lambda,\mathrm{ice}}$ to low $\gamma_{\lambda,\mathrm{water}}$ is $1/e^3$ of the initial difference between the mean γ_λ above ice ($\overline{\gamma}_{\lambda,\mathrm{ice}}$) and the mean γ_λ above open water ($\overline{\gamma}_{\lambda,\mathrm{water}}$):

$$\gamma_{\lambda,\mathrm{water}}(\Delta L_{\mathrm{HPT}}) = \overline{\gamma}_{\lambda,\mathrm{water}} + \frac{1}{e^3} \cdot \Delta \mathrm{IPA}, \qquad (5.2)$$
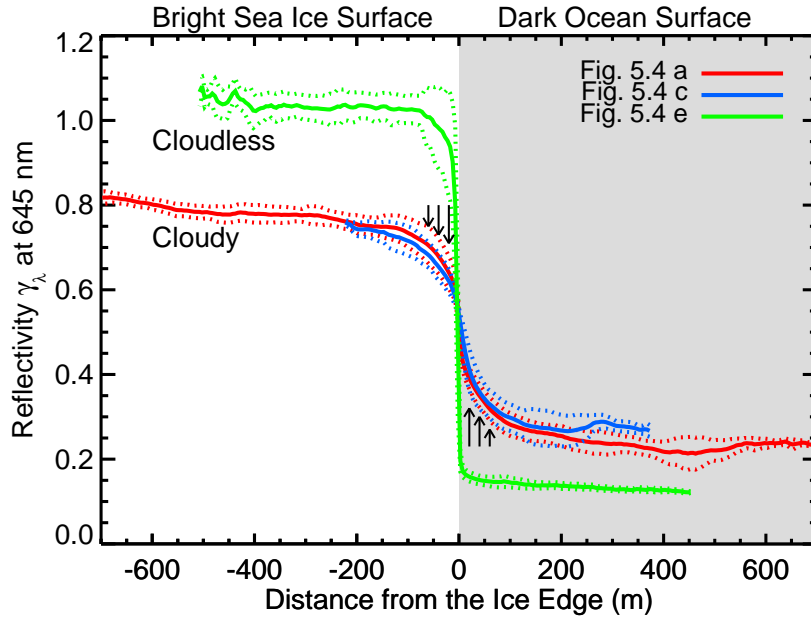
Figure 5.8: Averaged γ_λ (solid lines) $\pm 6\,\%$ measurement uncertainty of γ_λ (dashed lines) at $645\,\text{nm}$ wavelength, measured perpendicular to the ice edges shown in Fig. 5.5. Arrows indicate the particular enhancement or reduction of γ_λ close to the detected ice edges.

with $\Delta \text{IPA} = \overline{\gamma}_{\lambda,\text{ice}} - \overline{\gamma}_{\lambda,\text{water}}$. The threshold of $1/e^3$ ($\approx 5\,\%$) is chosen to make the results for ΔL_{HPT} comparable to the second distance, which is introduced in the following and related to the AisaEAGLE measurement uncertainty. Since ΔL_{HPT} is not related to the AisaEAGLE measurement uncertainty, $1/e^3$ instead of $6\,\%$ is chosen to avoid misunderstandings. By including ΔIPA, ΔL_{HPT} quantifies the range of horizontal photon transport independent of the difference of the surface albedo contrast. For the scene from Fig. 5.5a (see red line in Fig. 5.8), ΔL_{HPT} indicated by the enhancement of γ_λ over the water surface extends to a distance of $200\,\text{m}$ from the ice edge.

A second distance to the ice edge ΔL is defined for which $\gamma_{\lambda,\text{water}}$ is enhanced by $6\,\%$ of the average γ_λ above open water.

$$\gamma_{\lambda,\text{water}}(\Delta L) = \overline{\gamma}_{\lambda,\text{water}} + 0.06 \cdot \overline{\gamma}_{\lambda,\text{water}}. \tag{5.3}$$

The choice of the threshold results from the radiance measurement uncertainty ($\pm 6\,\%$) of the imaging spectrometer AisaEAGLE. Using this definition, ΔL is independent of γ_λ measured above the ice surface. It only accounts for the significance of the enhancement with respect to the measurement uncertainty. If the enhancement is higher than the measurement uncertainty, a cloud retrieval might be significantly biased. Therefore, ΔL is a measure for the horizontal extent within which the 3D effects bias the cloud retrieval in the vicinity of an ice edge. For the special case of the measured γ_λ in Fig. 5.8, $\Delta L = 300\,\text{m}$. Above open water, all measurements within that transition zone cannot be used for the cloud retrieval as the enhanced γ_λ will increasingly bias the retrieved τ_{st}.
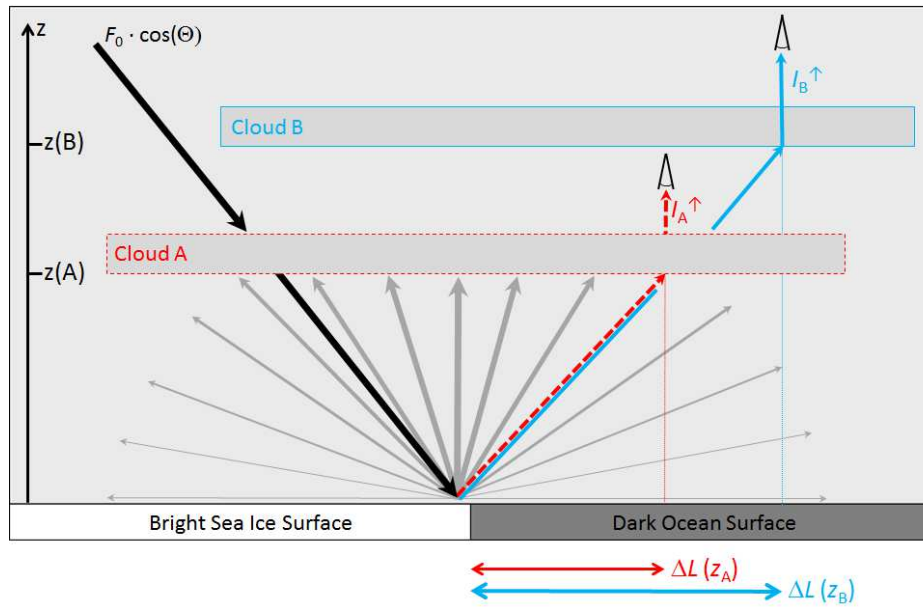
Figure 5.9: Sketch of the 3D radiative effects between clouds at two different altitudes and the surface in the vicinity of an ice edge. The arrows illustrate the pathway of the photons between source, cloud, surface, and sensor.

For the isolated ice floes of Fig. 5.5c, the values of the averaged γ_λ (solid blue line) in Fig. 5.8 are comparable to the values from the scenario in Fig. 5.5a. Furthermore, Fig. 5.8 shows a similar analysis (solid green line) for the cloud-free scenario on 14 May 2012 (Fig. 5.5f). Here, the decrease of γ_λ at the ice edge is significantly sharper than for the cloud-covered scenes. This indicates that in the cloudy scenes horizontal photon transport is taking place in the layer between the bright surface and cloud base, leading to a smoother transition between bright sea ice and dark ocean water.

5.4 Simulations

5.4.1 3D Radiative Transfer Model

To analyze the observations of 3D radiative effects at ice edges, a 3D radiative transfer model is applied. The simulations are used to determine ΔL and ΔL_{HPT} as a function of different cloud properties. It is expected that the interaction between clouds and sea-ice surface varies with varying τ_{st}, geometrical thickness, and cloud altitude. Furthermore, the simulations are used to clarify whether these 3D radiative effects result in an enhancement of the mean γ_λ for a certain area or if the enhancement is, on average, counterbalanced by the decrease of γ_λ above the sea ice. Different idealized sea-ice geometries are studied.

The radiative transfer simulations of the upward radiance $I_\lambda^\uparrow$ and downward irradiance $F_\lambda^\downarrow$ to derive γ_λ are performed with the open-source **M**onte **C**arlo **A**tmospheric **Ra**diative **T**ransfer **S**imulator (MCARaTS), which is a forward-propagating Monte Carlo photon-

transport model (Iwabuchi, 2006; Iwabuchi and Kobayashi, 2008). It traces individual photons on their path through the 3D atmosphere. To reduce the computational effort for radiance simulations, MCARaTS uses several variance-reduction techniques, such as a modified local-estimate method or a truncation approximation for highly anisotropic phase functions (Iwabuchi, 2006). The input for the radiative transfer model contains the optical properties of clouds, aerosol particles, trace gases (e.g. extinction coefficient, single-scattering albedo, phase function), and the 2D surface albedo. An albedo field of 20 km by 20 km with a pixel size of 50 m by 50 m (400 pixels in both horizontal dimensions) is created. Depending on the given sea-ice distribution, the albedo of individual pixels is set to 0.910 at 645 nm for sea ice or 0.042 at 645 nm for dark ocean water (Bowker et al., 1985). The pixel size of the 3D model is about ten times larger than that of AisaEAGLE. However, model results and measurements are still comparable as the investigated 3D effects occur in the range of a few hundred meters on either side of the ice edge. Accordingly, the AisaEAGLE data are averaged for comparing the model results with the measurements. 2.2×10^9 photons were used in each single model run, which resulted in a noise level of the 3D simulations of less than 1 %. This value is much lower than the measurement uncertainties of AisaEAGLE.

Other input parameters for the model are adapted to the measurement conditions on 17 May 2012 around 17:00 UTC with a solar zenith angle of $\theta_0 = 58°$ and the solar azimuth angle of $\varphi_0 = 113°$. The extraterrestrial solar spectrum was taken from Gueymard (2004). The output altitude for $I_\lambda^\uparrow$ and $F_\lambda^\downarrow$ is 2920 m (10 000 ft flight altitude). With regard to the measured scenes (Fig. 5.5a and c), a horizontally and vertically homogeneous liquid water cloud was assumed between 0 and 200 m altitude. Besides reference simulations for clear-sky conditions, the cloud optical thickness was varied between $\tau_\mathrm{st} = 1$ and $\tau_\mathrm{st} = 10$ as observed by MODIS in the surroundings of the measurement area. Based on in situ observations (**C**loud **D**roplet **P**robe, CDP, Klingebiel et al., 2015), the effective radius of the liquid water droplets was set to $r_\mathrm{eff} = 15\,\mu\mathrm{m}$. The microphysical properties of the liquid water clouds are converted to optical properties by Mie calculations. Furthermore, profiles of the atmospheric pressure, temperature, density, and gases are taken from Anderson et al. (1986). Gas absorption was modelled by LOWTRAN (Low Resolution Transmission Model parameterization, Pierluissi and Peng, 1985), as adapted from SBDART (Santa Barbara DISORT Atmospheric Radiative Transfer, Ricchiazzi and Gautier, 1998).

Additionally, 1D simulations, which use the independent pixel approximation (IPA), are applied to the particular cases. The IPA simulations were performed with the same 3D model, but with a homogeneous surface albedo – either dark ocean water or bright sea ice. All other parameters remain the same as in the 3D simulations.

5.4.2 Case I: Infinitely Straight Ice Edge

An infinitely straight ice edge comparable to Fig. 5.5a is assumed. Figure 5.10 illustrates the results of the 1D (gray lines) and 3D (black lines) cases. Similar to the observations, γ_λ from the 3D simulations decreases above the bright sea ice, and increases above the dark ocean surface. The effect is larger the closer the pixel is located to the ice edge. In the clear-sky simulations this effect is small; 3D and IPA simulations are almost identical. This

indicates that the 3D effect is dominated by horizontal photon transport between sea ice and clouds and the scattering processes by the cloud particles into the nadir observation direction. Without clouds, the horizontal photon transport above the isotropically reflecting surface is of similar magnitude to the cloudy case. However, due to the weak scattering in the clear atmosphere compared to the scattering by cloud particles, this effect is only significant for cloudy cases.

Similar investigations are presented by Marshak et al. (2008) with respect to aerosol-cloud interactions. In the vicinity of clouds, they found that the radiance in cloudless columns is increased due to a cloud-induced enhancement of the Rayleigh scattering. In general, Fig. 5.10 shows that with increasing τ_{st} the slope of the decrease of γ_λ next to the ice edge is flattened. This is a result of the reduction in contrast between the dark ocean surface and bright sea-ice surface by the overlying clouds.
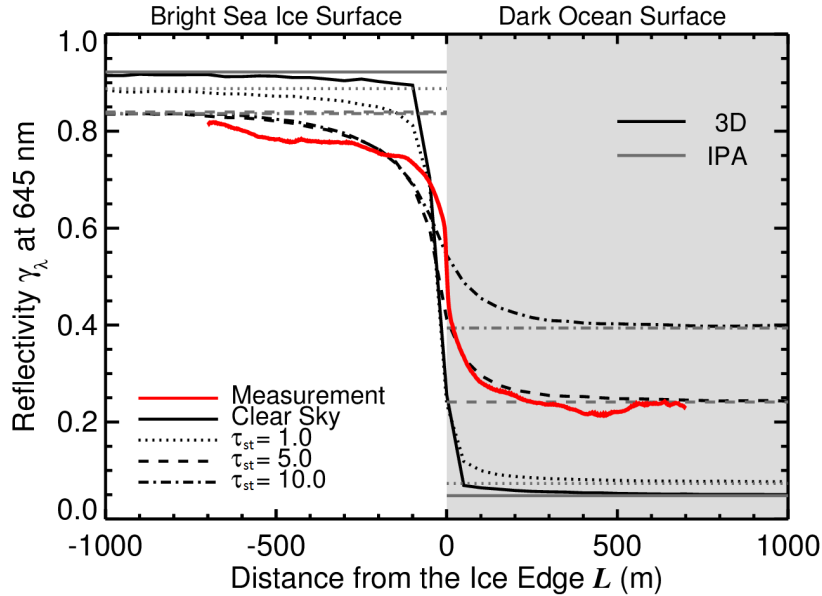

Figure 5.10: Simulated mean γ_λ across an ice edge for clear-sky conditions as well as for low-level clouds between 0 and 200 m altitude, $\tau_{st} = 1/5/10$, and $r_{eff} = 15\,\mu m$. The white area illustrates the bright sea ice, the gray area the dark ocean water. Included are the results of the 3D and IPA simulations, as well as the average of γ_λ, measured perpendicular to the ice edge in Fig. 5.5a.

To compare the results with the measurement example in Fig. 5.8, the distance ΔL_{HPT} defined by Eq. (5.2) is analyzed. The results are summarized in Tab. 5.2. $\overline{\gamma}_{\lambda,water}$ is set to the IPA values above water. For the cases presented in Fig. 5.10, ΔL_{HPT} increases with increasing τ_{st} from 100 m at $\tau_{st} = 1$ to 250 m at $\tau_{st} = 5$ and to 300 m at $\tau_{st} = 10$. This shows that the horizontal photon transport increases with τ_{st} due to increased scattering inside the cloud layer.

In contrast to ΔL_{HPT}, the distance ΔL (see Tab. 5.2) defined by Eq. (5.3) decreases from 600 m (at $\tau_{st} = 1.0$) to 400 m (at $\tau_{st} = 5.0$) and to 250 m (at $\tau_{st} = 10.0$). The decrease of ΔL suggests that the area in which γ_λ is enhanced and a cloud retrieval might be biased is smaller for optically thick clouds. This is related to the decrease in contrast between cloud

covered sea ice and cloud covered ocean if τ_{st} increases. The difference Δ(IPA) between $\gamma_{\lambda,ice}$ and $\gamma_{\lambda,water}$ decreases from $\gamma_\lambda = 0.87$ for the clear-sky case to $\gamma_\lambda = 0.44$ for $\tau_{st} = 10$, mainly due to the increasing reflection of incoming radiation by the cloud. If τ_{st} increases, $\gamma_{\lambda,water}$ increases, which results in a higher uncertainty range exceeding the γ_λ enhancement also in areas closer to the ice edge. Therefore, the γ_λ enhancement becomes less significant for a cloud retrieval compared to the measurement uncertainties. Since the aim is to retrieve τ_{st} above water areas enclosed by ice floes, in the following ΔL is used to quantify the 3D effects.

Additionally, the sensitivity of the results to the assumption of a constant r_{eff} was analyzed by running simulations with an r_{eff} of 10, 15, 20, and 30 μm (see Tab. 5.2). The results showed that ΔL is almost independent of r_{eff}. This indicates that a variation of r_{eff} does not need to be considered when estimating the 3D radiative effects described here.

Furthermore, simulations with variable values of the surface albedo were performed (see Tab. 5.2). Based on the measurement uncertainty of AisaEAGLE, the surface albedo of the dark ocean water and bright sea ice was varied by $\pm 6\%$. Over the dark ocean area, the simulations show almost identical results with differences far below 1% in γ_λ. Compared to the measurement uncertainties, those differences in the surface albedo are of less significance for ΔL. Indeed, the albedo has a larger effect over the sea-ice surface (up to 10%) due to the relative albedo change of 6%, which corresponds to an absolute change of ± 0.05 compared to 0.002 absolute change for the water surface. For the investigations presented here, the effect over the dark ocean area is relevant only.
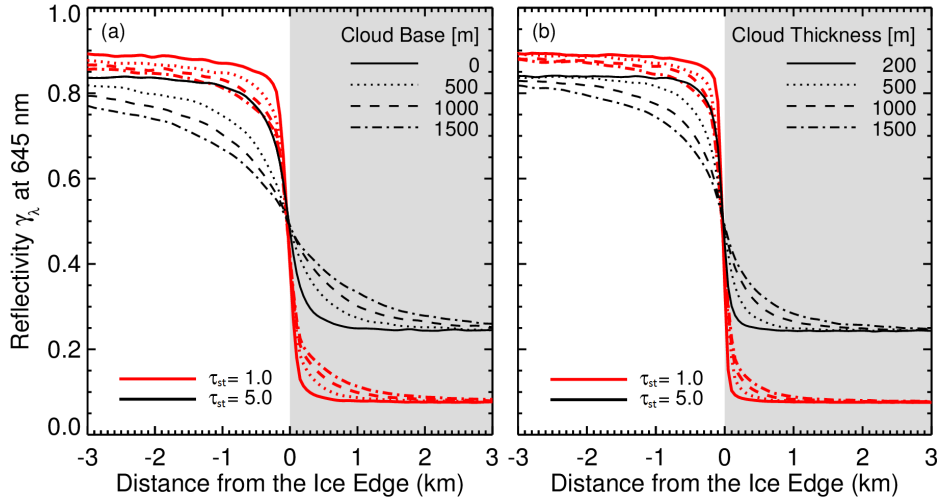
Figure 5.11: Simulated γ_λ for clouds at different altitudes and with different geometrical thickness for the passage from a highly reflecting ice-covered region to a darker region of open water. The white area illustrates the ice stripe. **(a)** Simulations for varying cloud base, given a fixed cloud geometrical thickness of 500 m. **(b)** Simulations for varying cloud geometrical thickness, given a fixed cloud base at 0 m.

Other important aspects, which influence the results, are the cloud altitude and cloud geometrical thickness. The horizontal photon transport resulting from the horizontal displacement of the location where a photon is isotropically scattered at the surface and the location in the

cloud where it is scattered afterwards into the viewing direction, changes if the cloud geometry changes. Figure 5.11 shows the simulated γ_λ for clouds of different altitude (Fig. 5.11a) and clouds of different geometrical thickness (Fig. 5.11b). Table 5.2 lists the corresponding ΔL. Increasing the cloud base of a cloud with a geometrical thickness of 500 m and $\tau_{st} = 1$ from $h_{cloud} = 0$ m to $h_{cloud} = 1500$ m, ΔL increases from 1000 to 4000 m. For $\tau_{st} = 5$, ΔL increases from 800 to 3200 m. Similarly, ΔL increases with increasing geometrical thickness. For $\tau_{st} = 1$, ΔL increases from 500 to 2200 m when the cloud geometrical thickness changes from 200 to 1500 m. For $\tau_{st} = 5$, ΔL increases from 300 to 2000 m. Compared to the influence of τ_{st}, the cloud altitude and cloud geometrical thickness have a similar impact on ΔL and cannot be neglected.
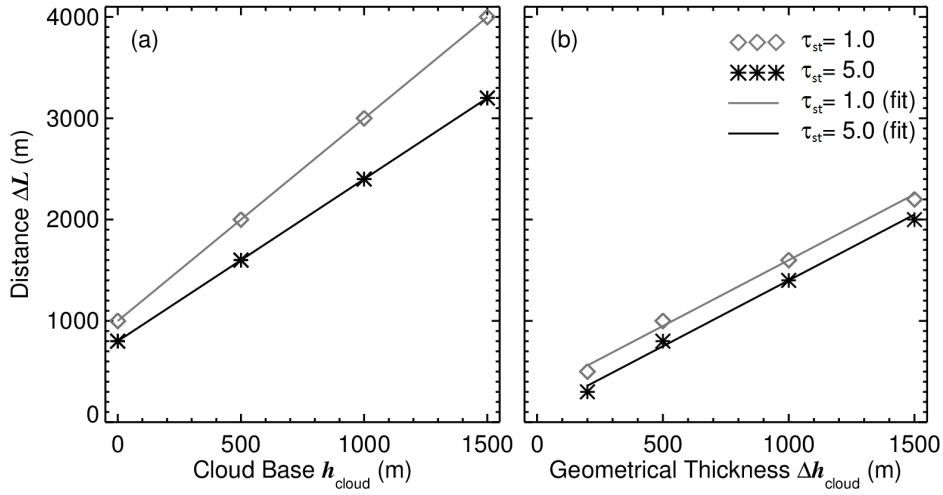

Figure 5.12: (a) Distance ΔL as a function of the cloud base altitude h_{cloud} for a cloud with a geometrical thickness of $\Delta h_{cloud} = 500$ m and different τ_{st}. (b) Distance ΔL as a function of the cloud geometrical thickness Δh_{cloud} for a low-level cloud with cloud base at $h_{cloud} = 0$ m and different τ_{st}.

For two model clouds with a geometrical thickness of 500 m and values of $\tau_{st} = 1$ and $\tau_{st} = 5$, Fig. 5.12a shows ΔL as a function of the cloud base altitude h_{cloud}. Similarly, Fig. 5.12b shows ΔL as a function of the cloud geometrical thickness Δh_{cloud} for low-level clouds with $\tau_{st} = 1$ and $\tau_{st} = 5$ and cloud base at 0 m. The increase of ΔL with increasing altitude of the cloud base (Fig. 5.12a) follows an almost linear function and can be parameterized by

$$\Delta L(h_{cloud}, \tau_{st}) = A_h(\tau_{st}) \cdot h_{cloud} + B_h(\tau_{st}). \tag{5.4}$$

For the parameters $A_h(\tau_{st})$ and $B_h(\tau_{st})$, the linear regression yields $A_h(\tau_{st}) = 2.00/1.6$ and $B_h(\tau_{st}) = 1000$ m/800 m for clouds with $\tau_{st} = 1/5$. This shows that the influence on ΔL is much larger for clouds at higher altitudes and lower τ_{st}. Comparing the results for $\tau_{st} = 1$ and $\tau_{st} = 5$ indicates that slope A decreases with increasing τ_{st}. This proves that the influence of cloud geometry on ΔL is decreasing with increasing τ_{st}.

Table 5.2: Summarized distances ΔL and ΔL_{HPT} of the presented case studies.

Cloud Optical Thickness τ_{st}	1	5	10	
ΔL_{HPT} ($h_{\mathrm{cloud}} = 0$–200 m, $r_{\mathrm{eff}} = 15\,\mu\mathrm{m}$) [m]	100	250	300	
ΔL ($h_{\mathrm{cloud}} = 0$–200 m, $r_{\mathrm{eff}} = 15\,\mu\mathrm{m}$) [m]	600	400	250	

Effective Radius r_{eff} [µm]	10	15	20	30
ΔL ($\tau_{\mathrm{st}} = 1$, $h_{\mathrm{cloud}} = 0$–200 m) [m]	600	600	600	600
ΔL ($\tau_{\mathrm{st}} = 5$, $h_{\mathrm{cloud}} = 0$–200 m) [m]	400	400	400	400

Surface Albedo α	+6 %	-6 %		
ΔL ($\tau_{\mathrm{st}} = 1$, $r_{\mathrm{eff}} = 15\,\mu\mathrm{m}$, $h_{\mathrm{cloud}} = 0$–200 m) [m]	600	600		
ΔL ($\tau_{\mathrm{st}} = 5$, $r_{\mathrm{eff}} = 15\,\mu\mathrm{m}$, $h_{\mathrm{cloud}} = 0$–200 m) [m]	400	400		

Cloud Base Altitude [m]	0–500	500–1000	1000–1500	1500–2000
ΔL ($\tau_{\mathrm{st}} = 1$) [m]	1000	2000	3000	4000
ΔL ($\tau_{\mathrm{st}} = 5$) [m]	800	1600	2400	3200

Cloud Geometrical Thickness [m]	0–200	0–500	0–1000	0–1500
ΔL ($\tau_{\mathrm{st}} = 1$) [m]	500	1000	1600	2200
ΔL ($\tau_{\mathrm{st}} = 5$) [m]	300	800	1400	2000

Similarly, ΔL increases almost linearly with increasing cloud geometrical thickness $\Delta h_{\mathrm{cloud}}$. This relation can be parameterized by

$$\Delta L(\Delta h_{\mathrm{cloud}}, \tau_{\mathrm{st}}) = A_{\Delta \mathrm{h}}(\tau_{\mathrm{st}}) \cdot \Delta h_{\mathrm{cloud}} + B_{\Delta \mathrm{h}}(\tau_{\mathrm{st}}). \tag{5.5}$$

The regression of the increase of ΔL with increasing cloud geometrical thickness yields $A_{\Delta \mathrm{h}}(\tau_{\mathrm{st}}) = 1.3/1.3$ and $B_{\Delta \mathrm{h}}(\tau_{\mathrm{st}}) = 300\,\mathrm{m}/100\,\mathrm{m}$ for clouds with $\tau_{\mathrm{st}} = 1/5$.

The cloud bases of all boundary layer clouds observed during VERDI ranged between 0 and 650 m, which is in agreement with the climatology presented by Shupe et al. (2011). To demonstrate the potential effects of clouds with higher cloud base, the following simulations cover two cloud cases, one similar to the observed cases from Fig. 5.5a–d with a cloud altitude of $h_{\mathrm{cloud}} = 0$–200 m and one with a cloud base at 500 m and a cloud top at 1000 m.

5.4.3 Case II: Single Circular Ice Floes

An infinitely straight ice edge as discussed in Sect. 5.4.2 does not represent reality in all aspects. Often, scattered ice floes of different size are observed (see Fig. 5.5c). In this case, a reduced 3D effect above open water due to the curvature of the ice edge is expected.

To analyze and quantify this reduction of 3D radiative effects, single circular ice floes of different size are simulated. The radius of the circular ice floe was varied from 100 to 1000 m in steps of 100 m and from 1 to 9 km in steps of 1 km. The center of the circular ice floe was placed in the middle of the model domain. For reasons of symmetry, a cross section through the center of the model domain was used for the data evaluation. Figure 5.13 shows the influence of the ice-floe size on ΔL.

As expected, ΔL is lower for small ice floe radii with larger curvature compared to the infinitely straight ice edge simulated in Sect. 5.4.2. For the assumed values of τ_{st}, ΔL increases with an increasing radius of the ice floe, asymptotically reaching a maximum value, which is identical to the results of the infinitely straight ice edge ($r = \infty$). This shows that all ice floes larger than about 6 km can be treated like the infinitely straight ice edge (for the given cloud and observation geometry).
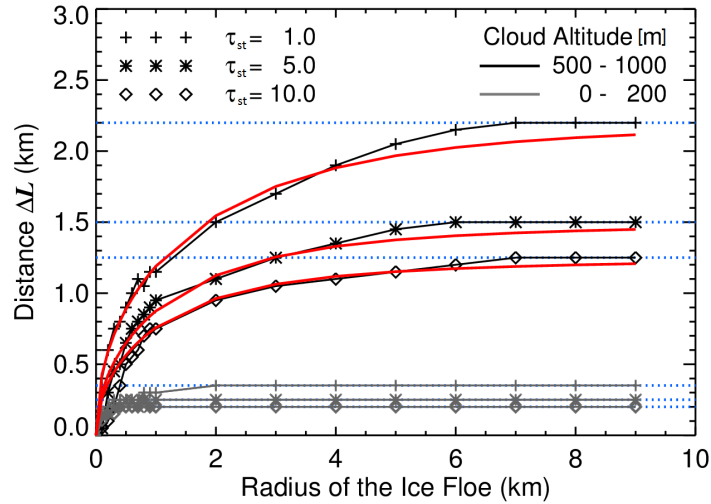

Figure 5.13: Simulations (gray and black lines) and parameterizations (red lines) of ΔL as a function of the ice-floe size, different τ_{st}, and different cloud altitudes. Asymptotic maximum values of ΔL are marked with dotted blue lines.

The reduction of ΔL for smaller ice floes can be explained by two effects. For ice floes with radii smaller than the distance ΔL of the infinitely straight ice edge, $r_{\text{floe}} < \Delta L(\tau_{\text{st}})$, the size of the ice area is too small for the γ_λ above the ice to reach the IPA γ_λ at any place. All areas of the ice floe are affected by 3D effects. On the other hand, the area of the ice floe is too small to fully affect the adjacent water area. The water area behind the ice floe limits its effect. For ice floes with a radius larger than ΔL, the IPA γ_λ will be reached at some point on the ice floe. Only the curvature of the floe reduces the 3D effect above open water. For any water point near the ice edge, the ice area located close to this point is reduced with increasing curvature. The curvature affects both small and large ice floes and lowers the 3D radiative effects slightly until the maximum effect, which is reached for an infinitely straight ice edge.

Combining these two effects and assuming an exponential relationship between ΔL and the ice-floe size r_{floe} (with regard to the shape of the lines in Fig. 5.13), the results presented in Fig. 5.13 are parameterized by:

$$\Delta L = \Delta L_{\max}(\tau_{\text{st}}) \cdot \left[1 - \frac{1}{3} \cdot \exp\left(-\frac{r_{\text{floe}}}{\Delta L_{\max}(\tau_{\text{st}})}\right) - \frac{2}{3} \cdot \exp\left(-\frac{r_{\text{floe}}^2}{C^2}\right)\right]. \qquad (5.6)$$

The distances for the infinitely straight ice edge, $\Delta L_{\max}(\tau_{\text{st}})$, are taken from Sect. 5.4.2. For the exponential parameter C, the fit yields $C = 1000$ m for clouds with $\tau_{\text{st}} = 1/5/10$. The parameterization is valid for ice floes with radii r_{floe} larger than 300 m. For those ice floes, the uncertainty is less than 5 %. For ice floes with radii r_{floe} less than 300 m, the uncertainty increases rapidly and reaches up to 100 %. This is due to the insufficient representation of the circular shape of the small ice floes by squared pixels with 50 m side length.

5.4.4 Case III: Groups of Ice Floes

In a next step, ice floes of different size have to be considered. The size of the ice floes, their shape and the distance to each other influence the 3D effects. To address these cases, four simulations with the same model setup as in Sects. 5.4.2 and 5.4.3, but with changed shape and number of the ice floes are performed. In total, four scenarios with ice floes represented by squares (total sea-ice area A_{x}, total ice-edge length l_{x}) were investigated to quantify the influence of A_{x} and l_{x} on the 3D effects.

In Scenario 1 (reference), an ice floe with a size of 5 km by 5 km ($A_1 = 25$ km^2, $l_1 = 20$ km) was placed in the center of the model domain (Fig. 5.14a). For Scenario 2 (Fig. 5.14b), the total sea-ice area was conserved ($A_2 = A_1 = 25$ km^2), however, the total ice-edge length was doubled ($l_2 = 2 \cdot l_1 = 40$ km). This was realized by four smaller ice floes (2.5 km by 2.5 km), separated by a distance of 5 km from each other. Scenario 3 (Fig. 5.14c) simulates two small ice floes (2.5 km by 2.5 km) for which the total ice-edge length has been conserved ($A_3 = 0.5 \cdot A_1 = 12.5$ km^2, $l_3 = l_1 = 20$ km). Scenario 4 (Fig. 5.14d) was designed to investigate the effect of the distance between the single ice floes. The two ice floes of Scenario 3 ($A_4 = 0.5 \cdot A_1 = 12.5$ km^2, $l_4 = l_1 = 20$ km) were copied, but placed next to each other.

As expected, in each scenario the contrast at the ice floe boundaries is reduced due to the 3D effects. To quantify the 3D radiative effect in the entire model domain, average and standard deviation of γ_λ are calculated separately for the total domain, for sea-ice areas, and for dark ocean areas (see Tab. 5.3). The average γ_λ is largest for Scenario 1 and smallest for Scenarios 3 and 4. This is not surprising since the area of the ice floes in Scenario 3 and 4 is half the area of the reference scenario. Compared to the IPA results, evidence of the 3D radiative effect is found in a slight reduction of the average γ_λ in all scenarios. This reduction originates from the absorption of the radiation that is scattered by the cloud base back into the direction of the dark ocean surface. This part of absorption is not considered in the IPA simulations, which leads to a lower scene average reflection in the 3D simulations. The standard deviations in the 3D simulations are also lower than in the IPA results, which
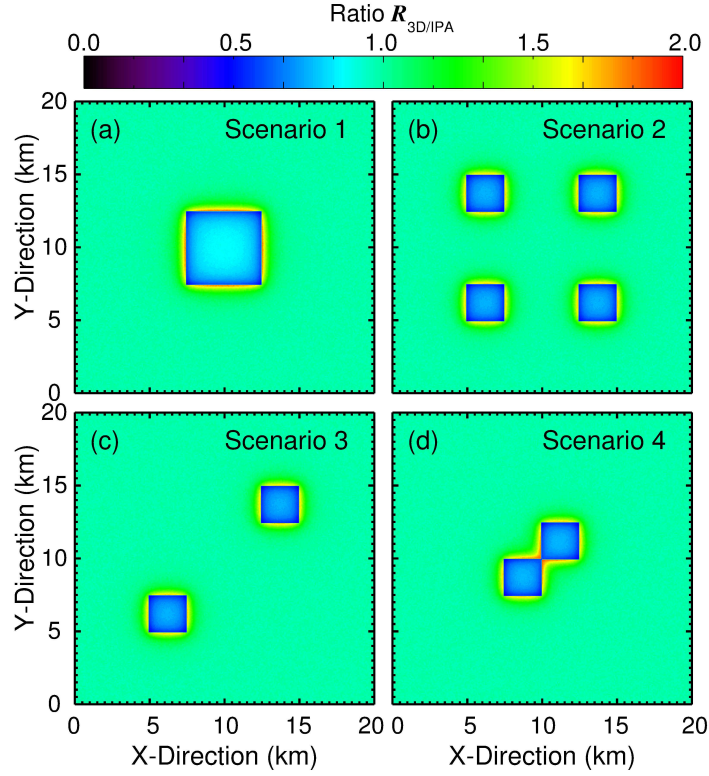
Figure 5.14: Ratio $R_{3D/IPA}$ of γ_λ of the 3D and IPA simulation at $\tau_{st} = 5$ and for a cloud between 500 and 1000 m altitude. Each panel displays one of the four scenarios.

corresponds to the smoothing at the ice edges. Furthermore, Tab. 5.3 reveals that the magnitude of $\gamma_{\lambda,water}$ and $\gamma_{\lambda,ice}$ is a function of the ratio between the sea-ice area and ice-edge length (A/l). With increasing ratio A/l, $\gamma_{\lambda,water}$ decreases and $\gamma_{\lambda,ice}$ increases. This is related to the lower probability that the sea-ice surface is directly connected to the dark ocean surface. Regarding $\gamma_{\lambda,total}$, no significant influence of A/l is found. Here, the magnitude of $\gamma_{\lambda,total}$ is mainly a function of the total sea-ice area compared to the total dark ocean area.

To quantify the 3D radiative effects, the ratios $R_{3D/IPA} = \gamma_{\lambda,3D}/\gamma_{\lambda,IPA}$ of the derived γ_λ from the 3D and IPA simulations are calculated. If both simulations are equal, the ratio is $R_{3D/IPA} = 1$. Compared to the IPA simulations, a ratio of $R_{3D/IPA} > 1$ represents an enhancement of γ_λ. Table 5.4 lists $R_{3D/IPA}$ for all simulated τ_{st} and h_{cloud}. Figure 5.14 displays the $R_{3D/IPA}$ for a cloud with $\tau_{st} = 5$ at $h_{cloud} = 500$–$1000\,\text{m}$, since the 3D effects are more evident for larger τ_{st} and higher cloud altitudes. Yet, the overall 3D effect is relatively small with $R_{3D/IPA}$ ranging from 0.965 to 0.984, but is still significantly higher than the noise level of the 3D simulations. The small values are caused by the large model domain and the relatively small ice fraction. Most pixels are ice-free and at a distance to the ice floes where 3D effects are negligible.

In Scenarios 1–3, the individual ice floes do not affect each other, as the distance between them is too large. Here, similar 3D effects are observed. The corners of the ice floes are smoothed out and the γ_λ field around the ice floe becomes more circular. This results in larger ΔL values at the center of the ice edges and in smaller ΔL values close to the corners.

Table 5.3: Average and standard deviation of the simulated γ_λ from the four presented scenarios for the whole surface albedo field ($\gamma_{\lambda,\text{total}}$), ice covered areas only ($\gamma_{\lambda,\text{ice}}$), and water covered areas only ($\gamma_{\lambda,\text{water}}$). Simulations performed for clouds with an optical thickness of $\tau_{\text{st}} = 1$ and $\tau_{\text{st}} = 5$.

Simulation	Scenario	$\gamma_{\lambda,\text{total}}$	$\gamma_{\lambda,\text{ice}}$	$\gamma_{\lambda,\text{water}}$
3D, $\tau_{\text{st}} = 1$	1	0.122 ± 0.171	0.782 ± 0.045	0.077 ± 0.012
	2	0.122 ± 0.163	0.737 ± 0.045	0.081 ± 0.020
	3	0.098 ± 0.118	0.737 ± 0.045	0.077 ± 0.012
	4	0.098 ± 0.118	0.741 ± 0.045	0.081 ± 0.024
IPA, $\tau_{\text{st}} = 1$	1	0.126 ± 0.200	0.896	0.073
	2	0.126 ± 0.200	0.896	0.073
	3	0.102 ± 0.147	0.896	0.073
	4	0.102 ± 0.147	0.896	0.073
3D, $\tau_{\text{st}} = 5$	1	0.274 ± 0.105	0.654 ± 0.081	0.250 ± 0.024
	2	0.270 ± 0.081	0.561 ± 0.065	0.254 ± 0.028
	3	0.254 ± 0.061	0.561 ± 0.065	0.250 ± 0.020
	4	0.254 ± 0.061	0.569 ± 0.065	0.250 ± 0.024
IPA, $\tau_{\text{st}} = 5$	1	0.279 ± 0.145	0.844	0.241
	2	0.279 ± 0.145	0.844	0.241
	3	0.258 ± 0.105	0.844	0.241
	4	0.258 ± 0.105	0.844	0.241

For the large ice floe of Scenario 1, $\Delta L = 1400\,\text{m}$ at the center of each side. In agreement with Fig. 5.13, ΔL for the small ice floes in Scenarios 2 and 3 is smaller ($1200\,\text{m}$). Along the normal line of the corners, ΔL is reduced to $900\,\text{m}$ for Scenario 1 and $700\,\text{m}$ for Scenarios 2 and 3. In Scenario 4, the ice floes cause a different pattern close to their point of contact. Here, ΔL is largest measured tangential to the connected corners and reaches $2000\,\text{m}$ as the 3D radiative effects of both floes add up for these points.

Fig. 5.15 shows frequency distributions of γ_λ for the four scenarios. Since the clouds are homogeneous in the simulations, the γ_λ in areas unaffected by 3D effects are identical to the γ_λ from the IPA simulation. For the open-water pixels, this causes a single peak at $\gamma_\lambda(\tau_{\text{st}} = 5) = 0.24$. For pixels above ice, no single peak corresponding to the IPA $\gamma_\lambda(\tau_{\text{st}} = 5) = 0.84$ is observed. This is due to the small size of the ice floes, above which the IPA γ_λ is not reached. All γ_λ values that are not included in the single water peak result from the 3D effects. Above ice, the distributions of Scenarios 2–4 are shifted to lower γ_λ compared to Scenario 1. This is because the diameter of the floes is even smaller than in Scenario 1. Thus, the large reflectivity values of Scenario 1 are not reached by Scenarios 2–4 (compare Fig. 5.13). Comparing the frequency distribution of Scenarios 1 and 2, Fig. 5.15a reveals the effect of the increased ice-edge length in Scenario 2. More pixels are affected by 3D effects and show values different from IPA. Furthermore, with four times the number of corners in Scenario 2, γ_λ above water is slightly shifted to lower values compared to the reference case. Similar effects can be observed in Scenario 3. In Scenario 4, the combined effect of both floes

Table 5.4: Ratio $R_{\mathrm{3D/IPA}}$ of γ_λ for the total scene area (R_{total}), for the sea-ice covered area (R_{ice}), and for the dark ocean covered area (R_{water}) of all scenarios from Sects. 5.4.4 and 5.4.5. The simulations for Scenario 1–4 are performed with clouds of $\tau_{\mathrm{st}} = 1$ and $\tau_{\mathrm{st}} = 5$ at an altitude of 0–200 and 500–1000 m. The simulation for the real case is performed with a cloud of $\tau_{\mathrm{st}} = 5$ at an altitude of 100–200 m.

0–200 m	$\tau_{\mathrm{st}} = 1$			$\tau_{\mathrm{st}} = 5$		
Scenario	R_{total}	R_{ice}	R_{water}	R_{total}	R_{ice}	R_{water}
1	0.997	0.961	1.030	0.995	0.951	1.007
2	0.991	0.941	1.043	0.991	0.917	1.016
3	1.000	0.940	1.030	0.995	0.917	1.007
4	1.001	0.942	1.048	0.995	0.918	1.012
Real Case	–	–	–	0.926	0.732	1.240

500–1000 m	$\tau_{\mathrm{st}} = 1$			$\tau_{\mathrm{st}} = 5$		
Scenario	R_{total}	R_{ice}	R_{water}	R_{total}	R_{ice}	R_{water}
1	0.974	0.875	1.072	0.974	0.775	1.032
2	0.965	0.825	1.128	0.965	0.665	1.060
3	0.984	0.823	1.067	0.979	0.665	1.028
4	0.984	0.829	1.094	0.981	0.675	1.039

leads to larger enhancements above ocean water than in Scenarios 2 and 3. In comparison to Scenario 3, the reduced distance between the ice floes in Scenario 4 leads to a shift of the frequency distribution over water to larger γ_λ values. Similar results can be observed for the frequency distribution over ice.

In order to identify the relevant effects, the ratios $R_{\mathrm{3D/IPA}}$ for ice-free (R_{water}) and ice-covered (R_{ice}) areas are calculated separately (Tab. 5.4). The reduction of γ_λ above ice is larger ($R_{\mathrm{ice}} = 0.823$–0.875) than the enhancement above water ($R_{\mathrm{water}} = 1.072$–$1.128$), which is partly a result of the larger water area. The small size of the ice floes leads to the stronger effects above sea ice, as the IPA γ_λ is not reached. Interestingly, with increasing τ_{st}, the deviations from IPA increase for the ice area but decrease for the dark ocean area. This effect is related to the asymmetry of enhancement and reduction for clouds of high τ_{st}, as shown in Fig. 5.10.

The average reduction over sea–ice areas (R_{ice}) is largest for Scenario 1. For all other scenarios, smaller values are obtained, with Scenarios 2 and 3 showing identical values. This indicates that the particular distance between the ice floes in Scenarios 2 and 3 is large enough to suppress influence of the single ice floes on each other. Scenario 4 gives the second largest R_{ice}. Compared to Scenario 1 and Scenario 3, this confirms that the distance between the ice floes has a significant influence on the enhancement of γ_λ over dark ocean water in the vicinity of ice edges.

R_{water} is almost equal for Scenarios 1 and 3, although the ice-covered area differs by a factor of two. For Scenario 2, with a doubled ice-edge length, this ratio is significantly larger. This leads to the conclusion that the ice-edge length has a significantly larger effect on the
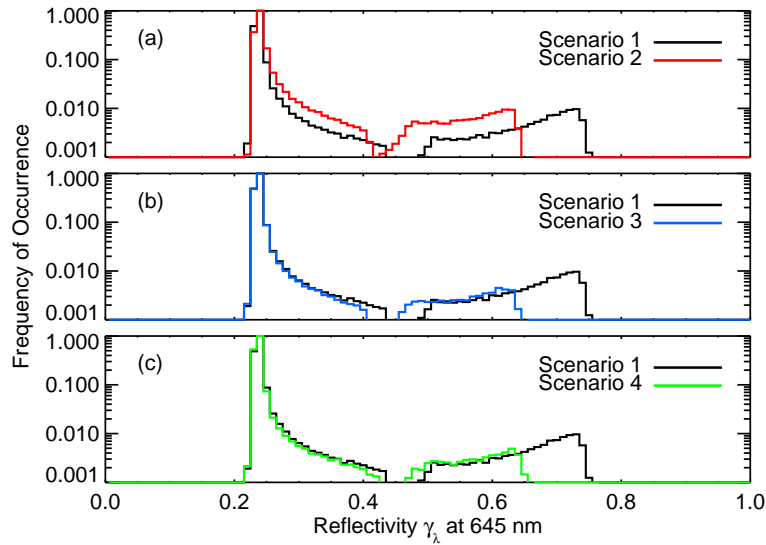
Figure 5.15: Single logarithmic frequency distributions of the simulated γ_λ from all four scenarios displayed in Fig. 5.14.

enhancement of γ_λ (over the water next to an ice edge) than the size of the area covered by sea ice.

5.4.5 Case IV: Realistic Sea-Ice Scenario

In order to combine several aspects of the 3D effects, γ_λ was simulated above an albedo field generated from the observation shown in Fig. 5.5c. The pixel size of the albedo map was adjusted to the pixel number and size of the AisaEAGLE measurements (488 by 601 pixels with 5 m pixel side length).

The albedo map was used in the simulations implementing a cloud of $\tau_{st} = 5$ and a fixed $r_{eff} = 15\,\mu m$, as derived from in situ measurements. With regard to the measurements of the AMALi aboard Polar 5 and the closest drop sonde (see Fig. 5.6), the cloud top altitude was set to 200 m.

The best agreement between measurement and simulation is derived for this specific case for a cloud base altitude of 100 m and a slightly adjusted surface albedo ($\alpha_{water} = 0.09$, $\alpha_{ice} = 0.83$). Figure 5.16 shows the frequency distributions of simulated and observed γ_λ.

The maxima of the ocean-water and sea-ice peaks are found at equal γ_λ. In regions over dark ocean water as well as over bright sea ice, the γ_λ of the observation show a broader distribution than the γ_λ of the simulation. Indeed, the magnitude of the simulated γ_λ peak above the sea-ice surface agrees well with the peak from the observation, while the difference above the dark ocean water is larger. The different magnitude and the broader distribution of the observed single peaks compared to the simulation result from simplifications in the simulations where a horizontally homogeneous cloud is assumed. Thus, variations of γ_λ due to cloud 3D effects are not included here. Only the surface 3D effects cause a broadening of the frequency distribution. However, while surface effects will fill up the gap between the two
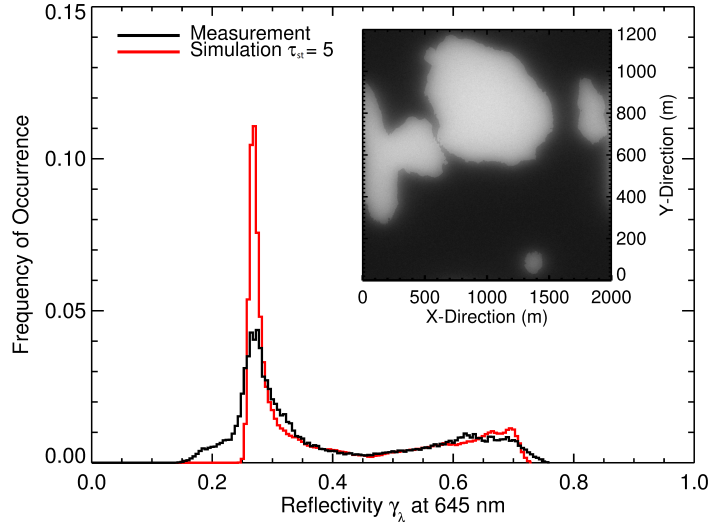
Figure 5.16: Frequency distributions of measurement and simulation. 3D simulation performed for the second measurement case, presented in Fig. 5.5 and Sect. 5.2. The bin size in γ_λ is 0.005.

peaks only, cloud inhomogeneities can also result in values smaller (over water) and higher (over sea ice) than the IPA simulations.

Table 5.4 shows the ratios $R_{\mathrm{3D/IPA}}$ between the results of the 3D and IPA simulation for the realistic sea-ice scenario. Compared to the idealized scenarios in Sect. 5.4.4, for the realistic sea-ice scenario the differences between the IPA and 3D simulations are larger above dark ocean water and smaller above bright sea ice. This behavior is related to the larger sea-ice fraction in the realistic sea-ice distribution, where water pixels are surrounded by a larger ice area compared to the isolated sea-ice floes of Sect. 5.4.4. On the one hand, it shows that the main characteristics of the ice-edge induced 3D radiative effects in clouds can be studied by using idealized surface albedo fields. On the other hand, in case of a real sea-ice distribution from measurements, it is also necessary to consider the real surface-albedo distribution for deriving ΔL and the overestimation in the retrieved τ_{st} and r_{eff}. No fixed values for ΔL or the overestimation can be given as a function of τ_{st} and cloud altitude only. The surface-albedo distribution plays a major role as well and has to be known.

5.5 Sensitivity of τ_{st} and r_{eff} derived from Synthetic Cloud Retrieval

All simulations in Sect. 5.4 showed that γ_λ over open water areas close to sea ice is enhanced if clouds are present. For a cloud retrieval following the strategy by Bierwirth et al. (2013), this enhancement suggests that τ_{st} will be overestimated in this area when a surface albedo of water is assumed. To quantify the magnitude of this overestimation, a synthetic cloud retrieval is investigated. It is based on simulations to investigate the uncertainties of retrieved r_{eff}, which cannot be derived from the current setup of AisaEAGLE measurements during VERDI. The limitation of AisaEAGLE to visible wavelengths restricts the retrieval to τ_{st}

(Bierwirth et al., 2013). However, near-infrared measurements might be available by use of additional imaging spectrometers. Therefore, this study addresses both quantities τ_{st} and r_{eff}.

The retrieval based on the best fit to the forward simulations is applied to the γ_λ field of a 3D simulation where the cloud optical properties are predetermined. An isolated ice floe with a radius of 6 km (Sect. 5.4.3) is chosen and a homogeneous cloud with $\tau_{st} = 10$ and $r_{eff} = 15\,\mu m$ is placed above it at an altitude of 500 to 1000 m. With a radius of 6 km the ice floe has an effect similar to that of an infinitely straight ice edge, which leads to the maximum range of 3D effects with the largest ΔL (see Fig. 5.13). The retrieval is performed over the dark ocean surface. The forward simulations of the γ_λ LUT are based on 1D simulations. τ_{st} and r_{eff} are varied in the range of 1–25 and 10–25 µm, respectively; see Fig. 5.17. The retrieval grid is constructed from the simulated γ_λ at 645 nm wavelength on the abscissa and the ratio of γ_λ at 1525 and 579 nm wavelength on the ordinate. This wavelength and the wavelength ratio is chosen in order to improve the retrieval method by Bierwirth et al. (2013).

The choice of wavelength follows the method presented by Werner et al. (2013). This method creates a retrieval grid with a more separated solution space for τ_{st} and r_{eff} than the classic two-wavelength method by Nakajima and King (1990) or Bierwirth et al. (2013). Furthermore, it effectively corrects the retrieval results for the influence of overlying cirrus and reduces the retrieval error for τ_{st} and r_{eff} caused by calibration uncertainties (Werner et al., 2013). For airborne investigations of τ_{st} and r_{eff} with large spatial coverage and high spatial resolution, this results in a higher accuracy of the retrieved cloud properties.
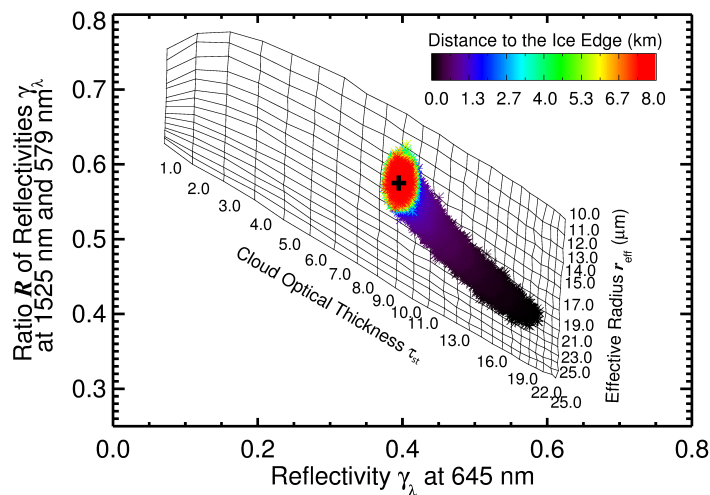

Figure 5.17: Retrieval grid using γ_λ at 645 nm and the ratio of γ_λ at $\lambda_1/\lambda_2 = 1525\,nm/579\,nm$. γ_λ of the 3D simulation are illustrated by color-coded dots as a function of distance to the ice-floe edge. The black cross marks the exact cloud properties $\tau_{st} = 10$ and $r_{eff} = 15\,\mu m$ used in the 3D simulation for the cloud at 500 to 1000 m altitude.

The γ_λ of the 3D simulation is plotted in Fig. 5.17 as dots color-coded with the distance to the ice edge. The exact result of a cloud with $\tau_{st} = 10$ and $r_{eff} = 15\,\mu m$ is marked with a black cross. The results imply a significant overestimation of τ_{st} and r_{eff} at distances below 2 km

from the ice edge (dark blue dots). The overestimation increases with decreasing distance to the ice edge. As expected, for distances larger than $2\,\mathrm{km}$ from the ice edge (light blue to red dots) the γ_λ is close to the IPA value (black cross). Small deviations are results of noise in the 3D simulations. For the range below $\Delta L = 2\,\mathrm{km}$, the mean τ_{st} and r_{eff} (solid lines) and their standard deviation (dotted lines) derived from the retrieval are shown as a function of the distance to the ice edge in Fig. 5.18.

The graph shows that the overestimation of τ_{st} increases to up to $90\,\%$ while r_{eff} is biased by up to $30\,\%$ close to the ice edge. Both values are valid only for the cloud used in the simulations ($\tau_{\mathrm{st}} = 10$ and $r_{\mathrm{eff}} = 15\,\mu\mathrm{m}$). For a smaller τ_{st}, the effect will be reduced. Furthermore, Fig. 5.18 shows that the overestimation of τ_{st} increases approximately exponentially starting at about $1.5\,\mathrm{km}$ distance, while the overestimation of r_{eff} increases more slowly and only reaches up to a distance of $1.0\,\mathrm{km}$.
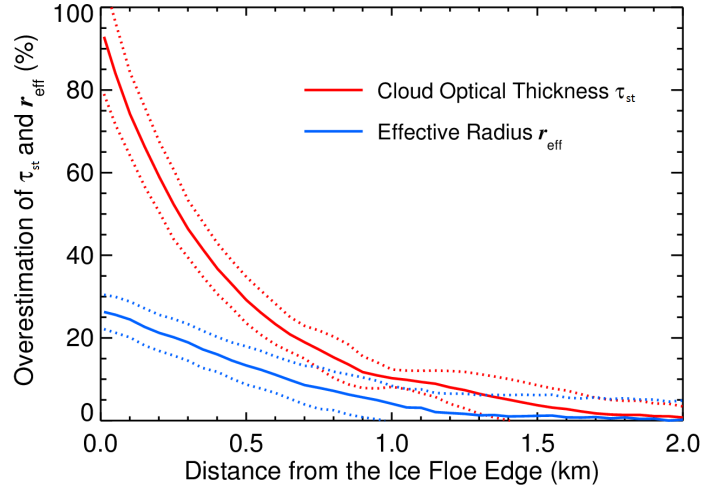
Figure 5.18: Overestimation (average and standard deviation) of τ_{st} and r_{eff} as a function of the distance to the edge of the ice floe. The model cloud at an altitude of 500 to $1000\,\mathrm{m}$ had $\tau_{\mathrm{st}} = 10$ and $r_{\mathrm{eff}} = 15\,\mu\mathrm{m}$.

This indicates that the magnitude of the 3D effects depends on the wavelength. In all simulations shown in Sect. 5.4.1, a wavelength of $645\,\mathrm{nm}$ is used for the retrieval of τ_{st}. However, the retrieval of r_{eff} also requires simulations at $1525\,\mathrm{nm}$ in the absorption band of liquid water. Therefore, the smaller magnitude and horizontal extent of the overestimation of r_{eff} compared to the magnitude and horizontal extent of the overestimation of τ_{st} suggest that the 3D effects will be smaller at absorbing wavelengths.

5.6 Cloud Optical Thickness Retrieval

With respect to the retrieval uncertainties caused by ice surfaces as discussed in Sect. 5.5, the following retrievals of τ_{st} are only performed over areas covered by dark ocean water and for a sufficiently large distance to the ice edges (larger than ΔL, as estimated from cloud

geometry and first guess of τ_{st}). From all flights, conducted during VERDI, ten segments (4 to 26 km long) of AisaEAGLE measurements are chosen, which allow a retrieval of τ_{st}.

As the AisaEAGLE imaging spectrometer is restricted to measurements in the visible wavelength range only, the r_{eff} is provided by the retrieval using the measurements of the SMART–Albedometer. Similar to the synthetic cloud retrieval presented in Sect. 5.5, radiance measured by SMART at wavelength of 645 nm and 1 525 nm are used to retrieve r_{eff} here. By the SMART–Albedometer, the r_{eff} is retrieved in nadir viewing direction only. For the retrieval of τ_{st} using AisaEAGLE, r_{eff} is assumed to be constant along the swath (all 488 spatial pixels in one line). Thus, variations of r_{eff} are only considered along the flight path. Uncertainties arising from a constant r_{eff} along the swath were quantified by Bierwirth et al. (2013) to be in a range less than the measurement uncertainty.

The measured fields of $I_\lambda^\uparrow$ are interpolated to LUT of simulated $I_\lambda^\uparrow$, obtained from *libRadtran* (Mayer, 2005). In comparison to the simulations for the CARRIBA campaign in Sect. 4.2, the radiative transfer calculations are initialized to represent the environmental parameters during the particular measurements. The relative geometry of the Sun and the observation geometry from the aircraft are obtained from the corresponding measurement time and a GPS/INS (**G**lobal **P**ositioning and **I**nertial **N**avigation **S**ystem) unit. The cloud-top altitude is obtained from AMALi measurements. The aerosol optical thickness (τ_{aer}) was observed by a Sun photometer on board of Polar 5. The OPAC Arctic aerosol type (**O**ptical **P**roperties of **A**erosols and **C**louds; Hess et al., 1998) is assumed in the calculations. The profiles of atmospheric gases are provided by *libRadtran* (subarctic winter; Anderson et al., 1986) and adapted by drop sonde profiles of T, p, and RH. A continuous transition from the standard to the drop–sonde profiles is derived by scaling the standard profiles. The surface albedo is set to values of open ocean, as the selected cases are performed over open ocean only. In situ measurements performed after the radiation measurements ruled out the existence of ice crystals for the investigated cases. Therefore, optical properties of cloud droplets are assumed and calculated from Mie theory.

Figure 5.19a shows an exemplarily field of retrieved τ_{st} (60 s measurement duration) from a measurement during the VERDI campaign on 14 May 2012 (Case V–01). The image is georeferenced with regard to the aircraft nadir direction. The FOV of the SMART–Albedometer is illustrated by the dark–blue (left boarder), red (nadir), and light–blue (right boarder) lines. With a flight altitude of 2920 m, a cloud–top altitude of 900 m and a measurement duration of 60 s at 30 Hz and 80 m s^{-1} flight speed, the covered swath was about 1 337 m, the flight path about 5 000 m long. Figure 5.19b illustrates the uncertainties of τ_{st} quantified by relative differences between retrieval assuming a $\pm 6\%$ measurement uncertainty of $I_\lambda^\uparrow$. For the bright cloud parts, the retrieval uncertainty rises up to 28.2 %. Figure 5.19c illustrates the corresponding frequency distribution of the retrieved field of τ_{st} presented in Fig. 5.19a. It shows a monomodal distribution with values of retrieved τ_{st} ranging from 5 to 16. The average of τ_{st} is 10.6 with a standard deviation of $\sigma_\tau = 1.6$.

In Tab. 5.5 statistical parameters of the ten retrieved fields of τ_{st}, including information on the measurement time, cloud top altitude (h_{ct}), field size (swath, length), and average and standard deviation of τ_{st} ($\bar{\tau}_{st} \pm \sigma_\tau$) are provided. The average swath of the covered fields has a size close to 1.3 km. The length varies from 4 km up to 26 km. Thus, sufficiently large
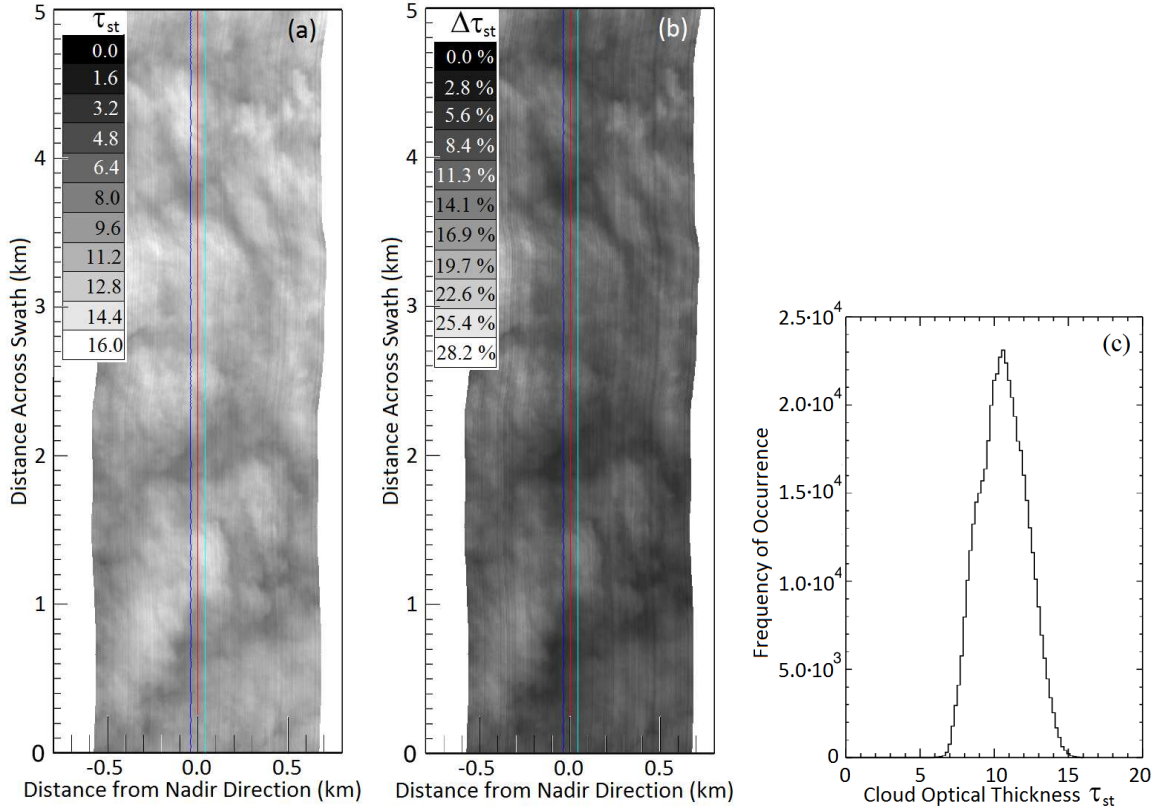
Figure 5.19: (a) Georeferenced field of τ_{st} of Arctic stratus. Cutout from measurement case V-01 with $60\,s$ measurement duration. **(b)** Relative uncertainty of τ_{st} field illustrated in (a), retrieved with radiance data varied by $\pm 6\,\%$. The dark–blue, red, and light–blue lines illustrate the FOV of the SMART–Albedometer. **(c)** Frequency distribution of retrieved τ_{st} from (a).

areas of the clouds are covered to provide a statistically firm analysis of τ_{st} and to investigate horizontal inhomogeneities in the fields of τ_{st} (provided in Chapter 6). The average of τ_{st} of all cases ranges between 3 and 14 with most $\bar{\tau}_{st}$ between 3 to 7. σ_τ reaches values from 15 to 34\% of $\bar{\tau}_{st}$.

The uncertainty of the simulations applied to the retrieval is estimated equally to the method presented in Eq. (4.1). It is defined by:

$$\Delta\bar{\tau}_{st} = 100\,\% \cdot \left(\frac{\bar{\tau}_{st,BM} - \bar{\tau}_{st}}{\bar{\tau}_{st,BM}} \right) \qquad (5.7)$$

For each simulated $\tau_{st,BM}$ from the benchmark retrieval, the simulations are repeated. In the second run, model input parameters are varied by their measurement uncertainty. $\Delta\bar{\tau}_{st}$ (in \%) quantifies the resulting differences compared to the benchmark case. Measurement uncertainties of the relative humidity and temperature profile are specified by the manufacturer Vaisala: $\pm 2\,\%$ for relative humidity and $\pm 0.2°C$ for temperature. The surface albedo is varied by $10\,\%$. According to the specifications of the Sun photometer, the aerosol optical

Table 5.5: Measurement period, cloud top altitude, swath, length, and average and standard deviation ($\bar{\tau}_{st} \pm \sigma_{\tau}$) of the retrieved fields of τ_{st} from suitable VERDI cases (V-01–V-10). The flight altitude is at 2920 m for each case.

Case	Day	Time (UTC)	$h_{ct}(m)$	Swath (m)	Length (m)	$\bar{\tau}_{st} \pm \sigma_{\tau}$
V-01	14 May 2012	20:31:47-20:36:31	900	1 337	21 277	9.93 ± 1.89
V-02	14 May 2012	20:38:04-20:42:09	850	1 368	20 825	7.82 ± 2.01
V-03	14 May 2012	20:53:26-20:58:30	850	1 368	26 848	3.82 ± 1.33
V-04	15 May 2012	18:41:53-18:43:58	1 000	1 273	10 503	14.34 ± 2.54
V-05	15 May 2012	21:05:10-21:09:24	930	1 317	20 215	6.35 ± 0.97
V-06	16 May 2012	19:10:56-19:15:56	1 000	1 273	23 103	6.52 ± 1.48
V-07	17 May 2012	16:53:23-16:56:06	250	1 750	12 743	3.04 ± 0.66
V-08	17 May 2012	17:00:59-17:06:15	1 000	1 273	25 653	5.48 ± 1.84
V-09	17 May 2012	17:09:28-17:10:38	2 250	477	5 463	7.07 ± 1.41
V-10	17 May 2012	18:49:26-18:50:16	230	1 763	4 103	4.15 ± 0.67

Table 5.6: Forward model errors $\Delta\bar{\tau}_{st}$ (in %) for different error sources: effective radius, surface albedo, aerosol optical thickness, temperature T, relative humidity RH.

Error Source	Variation	$\Delta\bar{\tau}_{st}$ (%)
Effective Radius r_{eff}	$\pm 9.5\%$	0.3–0.5
Surface Albedo α_{surf}	$\pm 10\%$	0.1–0.6
Aerosol Optical Thickness τ_{aer}	± 0.05	0.6–0.9
Temperature T	± 0.2 K	0.0–0.1
Relative Humidity RH	$\pm 2\%$	0.0–0.1

thickness is varied by ± 0.05. A further source of error is the uncertainty of the retrieved r_{eff}, provided by the SMART–Albedometer. Bierwirth et al. (2013) estimated an uncertainty of 9.5 % in the retrieved r_{eff}. For the uncertainty of the AisaEAGLE radiance measurements, a 6 % measurement error (related to the radiometric calibration) is assumed. The contribution of all error sources are summarized in Tab. 5.6. A comparison to the calibration uncertainty of 6 % shows that the calculated values of $\Delta\bar{\tau}_{st}$ are dominated by the measurement uncertainty of the AisaEAGLE radiance (compare Fig. 5.19b). All other error sources are below 1 %.

6 Directional Structure of Cloud Inhomogeneities

Retrieved fields of τ presented in Chapters 4 and 5 are analyzed to quantify horizontal inhomogeneities of two different cloud types; cirrus and Arctic stratus. The statistic evaluation of the horizontal inhomogeneity of those fields of τ uses 1D inhomogeneity parameters from the literature (Sect. 6.1), 2D auto–correlation functions (Sect. 6.2) and 2D Fourier analysis (Sect. 6.3).

6.1 Analysis with 1D Inhomogeneity Parameters

The standard deviation σ_τ of the τ fields for the four CARRIBA and ten VERDI measurement cases has been discussed in Sects. 4.5 and 5.6. However, σ_τ does not allow a comparison between different cases with different average cloud optical thickness $\bar{\tau}$. A cloud with higher $\bar{\tau}$ naturally can exhibit a higher standard deviation. Therefore, Davis et al. (1999) and Szczap et al. (2000) used a normalized inhomogeneity measure, the relative variability ρ_τ to quantify horizontal inhomogeneity of τ in clouds. It is described by the ratio of σ_τ and the average value of the corresponding sample:

$$\rho_\tau = \frac{\sigma_\tau}{\bar{\tau}}. \tag{6.1}$$

However, the fact that ρ_τ can exceed values of unity and is a function of the average value might lead to misinterpretations. Therefore, Davis et al. (1999) and Szczap et al. (2000) related the relative variability ρ_τ with the inhomogeneity parameter S_τ in the form:

$$S_\tau = \frac{\sqrt{\ln(\rho_\tau^2 + 1)}}{\ln 10}. \tag{6.2}$$

S_τ describes the standard deviation of the logarithmic mean of τ and quantifies the degree of cloud inhomogeneity. In case of a log-normal frequency distribution of τ it has a one-to-one relation to ρ_τ.

Oreopoulos and Cahalan (2005) investigated the inhomogeneity parameter χ_τ, first introduced by Cahalan (1994). χ_τ is defined by the ratio of the logarithmic and linear average of a distribution of τ:

$$\chi_\tau := \frac{\exp(\overline{\ln\tau})}{\bar{\tau}}, \tag{6.3}$$

χ_τ ranges between 0 and 1, with values close to 1 indicating horizontal homogeneity, and values close to 0 characterizing a cloud with high horizontal inhomogeneity. Oreopoulos and Cahalan (2005) state that the reflected solar flux is approximately a linear function of the logarithm of τ for a wide range (≈ 5 to ≈ 30, depending on θ_0) of τ. Thus, the logarithmically averaged τ provides a way to account for cloud inhomogeneity effects in plan-parallel radiative transfer calculations by including the nonlinear nature of the relation between τ and cloud albedo.

The three 1D inhomogeneity parameters ρ_τ, S_τ, and χ_τ are calculated for each retrieved field of τ_{ci} and τ_{st} from the CARRIBA and VERDI campaigns (see Tab. 6.1).

Table 6.1: Average and standard deviation ($\tau \pm \sigma_\tau$) and inhomogeneity parameters (ρ_τ, S_τ, χ_τ) calculated for retrieved fields of τ from CARRIBA (C-01–C-04) and VERDI (V-01–V-10).

Parameter	C-01	C-02	C-03	C-04
ρ_τ	0.40	0.35	0.17	0.91
S_τ	0.19	0.15	0.08	0.48
χ_τ	0.92	0.94	0.99	0.63

Parameter	V-01	V-02	V-03	V-04	V-05	V-06	V-07	V-08	V-09	V-10
ρ_τ	0.19	0.26	0.34	0.18	0.15	0.23	0.22	0.34	0.20	0.16
S_τ	0.08	0.11	0.20	0.08	0.07	0.11	0.11	0.15	0.09	0.08
χ_τ	0.98	0.97	0.92	0.98	0.99	0.97	0.97	0.95	0.98	0.99

The cirrus cases show ρ_τ in the range of 0.17–0.91, S_τ is in the range of 0.08–0.48. The largest values of ρ_τ and S_τ are found for 23 April 2011 (C-04), the lowest for 18 April 2011 (C-03). The values for ρ_τ and S_τ confirm the statement from Sect. 4.5 that the cirrus on 16 and 18 April 2011 was rather homogeneous and the cirrus on 9 and 23 April was rather inhomogeneous. For the ten Arctic stratus cases, ρ_τ and S_τ are in the range of 0.15–0.34 and 0.07–0.20, respectively. For stratocumulus Zuidema and Evans (1998) quantified the inhomogeneity of τ with $S_\tau = 0.1$–0.3. Iwabuchi (2000) and Iwabuchi and Hayasaka (2002) investigated the inhomogeneity of τ for overcast boundary layer clouds and found values of $S_\tau = 0.03$–0.3, which lead to $\rho_\tau = 0.07$–0.78. Thus, the derived values from CARRIBA and VERDI compare well with the values reported by Zuidema and Evans (1998), Iwabuchi (2000), and Iwabuchi and Hayasaka (2002). Out of all ten cases, ρ_τ and S_τ indicate case V–03 and V–08 to be more inhomogeneous than the other ones.

For CARRIBA, the values of χ_τ range from 0.63 to 0.99, indicating a rather inhomogeneous cirrus on 23 April 2011 (C-04) and rather homogeneous cirrus during the other days. In contrast to the results for ρ_τ and S_τ, χ_τ indicates the cirrus on 9 April 2011 as less inhomogeneous. The calculated values of χ_τ for the retrieved fields of τ_{st} from the VERDI campaign gives $\chi_\tau > 0.9$ in each case, with lowest values for case V-03 and V-08, which already were indicated by ρ_τ and S_τ to be more inhomogeneous than the other cases. Depending on cloud type, cloud phase, hemisphere, surface type, season, and time of day, Oreopoulos and Cahalan (2005) estimate the range of χ_τ from ≈ 0.65 to 0.8.

The comparison to the results from the literature and the results obtained in Chapters 4 and 5 shows that the derived 1D inhomogeneity parameters ρ_τ, S_τ, and χ_τ are suitable to characterize the general character of clouds with regard to their inhomogeneities. They are easy to calculate and are suitable to improve the results of simulations, which assume horizontal homogeneous clouds. However, ρ_τ, S_τ, and χ_τ do not provide a measure of the directional variability of the inhomogeneities, but different cloud types exhibit horizontal inhomogeneities of different size and orientation. For example, the observed clouds from the CARRIBA and VERDI campaigns are different in most aspects (e.g. cloud altitude, cloud structure, cloud phase, particle size and shape), but ρ_τ, S_τ, and χ_τ yield comparable values. Therefore, in order to investigate cloud inhomogeneities it is necessary to investigate not only the mean horizontal inhomogeneity but also its directional dependence (Hill et al., 2012).

6.2 Spatial 2D Auto-Correlation and De-Correlation Length

To quantify the directional inhomogeneities in the retrieved fields of τ, spatial 2D auto–correlation functions are calculated. The resulting auto–correlation coefficients P_τ describe the correlation of a τ field with itself, when it is spatially shifted against itself. Thus, spatial auto–correlation functions measure the degree of similarity between spatially distributed neighbouring samples. By nature, τ in close collocation show similar values, while cloud pixel at larger distances can significantly depend on the inhomogeneity of the sampled clouds.

The auto–correlation function $P_\tau(L_{xy})$ is calculated at fixed distances (lags) L_{xy}, which are derived as integer multiples of the equidistant measurement intervals x_i and y_j (Marshak et al., 1998). Here, with n and m equidistant measurement intervals x_i and y_j, $P_\tau(L_{xy})$ for 2D fields is calculated by:

$$P_\tau(L_{xy}) = P_\tau(-L_{xy}) = \frac{\sum\limits_{i,j+1}^{n,m} [\tau(x_i + L_x, y_j + L_y) - \bar{\tau}] \cdot [\tau(x_i, y_j) - \bar{\tau}]}{\sum\limits_{i,j+1}^{n,m} [\tau(x_i, y_j) - \bar{\tau}]^2}, \qquad (6.4)$$

$\tau(x_i, y_j)$ is the cloud optical thickness observed at the reference position and $\tau(x_i + L_x, y_j + L_y)$ the cloud optical thickness at lag L_{xy}. $P_\tau(L_{xy})$ yields values between -1 and 1, 1 representing a perfect positive correlation; a value of -1 is a perfect negative correlation and 0 indicates no correlation. The largest similarity between both samples is given for a spatial shift equal to zero (trivial solution). Here, $P_\tau(L_{xy})$ yields 1. To avoid ambiguous results with respect to positive and negative correlations, the squared auto-correlation function $P_\tau^2(L_{xy})$ is used, because it only yields values between 0 (no correlation) and 1 (perfect correlation).

Figures 6.1b and 6.1e show examples of $P_\tau^2(L_{xy})$, calculated for selected areas (500 by 500 Pixels, Fig.6.1a and b) of the fields of τ_{si} from case C-01 (in Fig.4.10a from 3.8 to 7.3 km along swath and from 0.0 to 3.5 km across swath) and C-03 (in Fig.4.10c from 5.0 to 8.5 km along swath and from 26.5 to 30.0 km across swath) with $L_{xy} = 250$. The magnitude of $P_\tau^2(L_{xy})$ ranges from 0 to 1 and is illustrated by the color coding. Based on the term $P_\tau(L_{xy}) = P_\tau(-L_{xy})$ in Eq. (6.4), the fields of $P_\tau^2(L_{xy})$ are symmetrically with respect to

the center of the images at $L_{xy} = 0$. Both cases show a different pattern of the decrease of $P_\tau^2(L_{xy})$ with increasing absolute value of L_{xy}. The magnitude of decrease depends on the horizontal structure of the cloud inhomogeneities. The $P_\tau^2(L_{xy})$ calculated from C-01 (Fig. 6.1b) show a regular shaped decrease, independent on the direction. In contrast, the $P_\tau^2(L_{xy})$ calculated from C-03 (Fig. 6.1e) show a directional dependence.
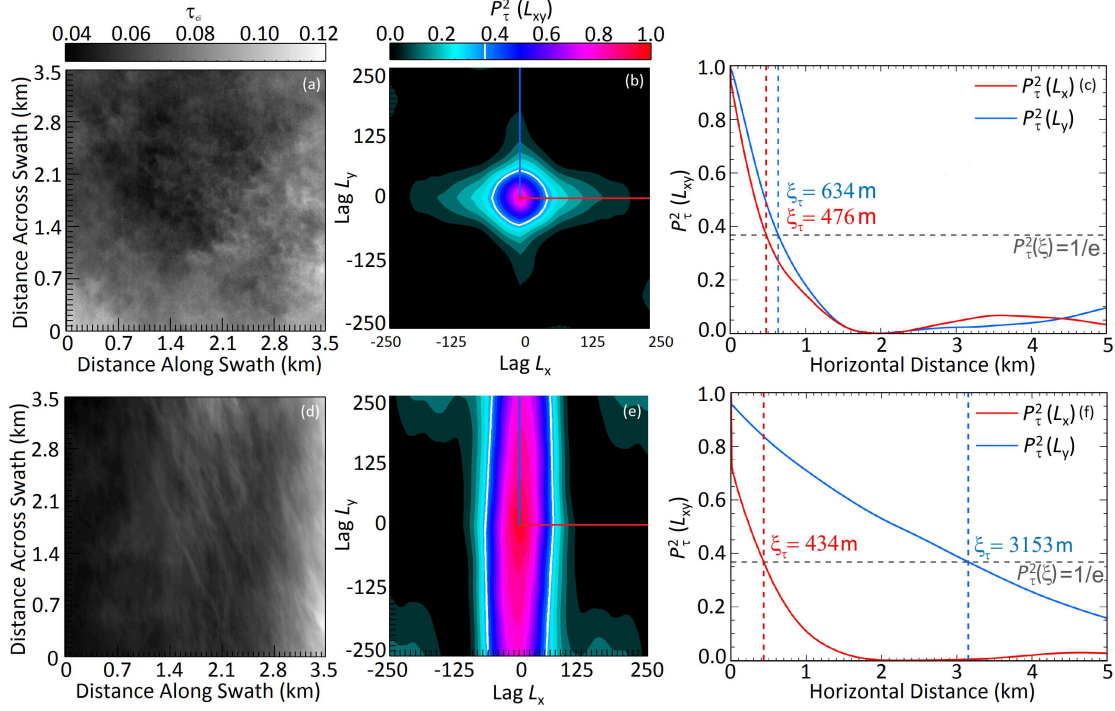

Figure 6.1: **(a)** Selected cloud scene (3.5 by 3.5 km) of field of τ_{ci} from case C-01. **(b)** Color coded 2D field of $P_\tau^2(L_{xy})$, calculated for field of τ_{ci} from (a). Blue and red line illustrate the lags, selected for the illustration in (c). White line illustrates ξ_τ at $P_\tau^2(L_{xy}) = 1/e$. **(c)** Average $P_\tau^2(L_{xy})$ (solid lines) and derived ξ_τ (dotted lines) along L_x (blue) and L_y (red) from (b). **(d)** Same as (a) for case C-03. **(e)** Same as (b) for selected τ_{ci} field shown in (c). **(f)** Same as (c) for $P_\tau^2(L_{xy})$ shown in (b).

The squared spatial auto–correlation function $P_\tau^2(L_{xy})$ are used to calculate the de–correlation length ξ_τ with:

$$P_\tau^2(\xi_\tau) = 1/e. \tag{6.5}$$

The de-correlation length quantifies the lag L_{xy}, at which $P_\tau^2(L_{xy})$ is decreased to a given value, usually $1/e$:

$$\xi_\tau = L_{xy}(P_\tau^2 = 1/e). \tag{6.6}$$

ξ_τ quantifies a length scale where individual cloud parcels are de-correlated and provides the size of typical cloud inhomogeneities; an increase in inhomogeneities yields a decrease in ξ_τ. In Fig. 6.1b, ξ_τ (at $P_\tau^2(L_{xy}) = 1/e$, indicated by white line) along lag L_x is similar to ξ_τ along lag L_y. In Fig. 6.1e, ξ_τ along lag L_x is significantly smaller than ξ_τ along lag L_y. This directional dependence is related to the structure of the cloud with regular filaments in the swath direction of the image in Fig. 6.1d. For case C-01 the symmetric 2D auto-correlation

functions allows to use a single de-correlation length independent of direction to characterize the cloud inhomogeneities. For regularly structured clouds such as C-03, however, the 2D de-correlation can be split into a component of the largest variability and a component along the smallest variability of τ. In the example both major axis align with the x and y direction. To estimate the magnitude of the uncertainties and to give quantitative values of ξ_τ for the retrieved fields of τ from the CARRIBA and VERDI campaigns, 1D auto–correlation functions are applied along lag L_x ($\leftrightarrow$, blue) and along lag L_y ($\updownarrow$, red) separately.

Figures 6.1c and 6.1f show the corresponding 1D $P_\tau^2(L_{xy})$ as a function of L_{xy}. For case C-01 (Fig. 6.1a to c), the derived 1D $P_\tau^2(L_{xy})$ are almost similar and $\bar{\xi}_\tau^{\updownarrow} = 634\,\mathrm{m}$ compares well with $\bar{\xi}_\tau^{\leftrightarrow} = 477\,\mathrm{m}$ within the range of standard deviation given in Tab. 6.2. For case C-03 (Fig. 6.1d to f), the 1D $P_\tau^2(L_{xy})$ differ significantly from each other and $\bar{\xi}_\tau^{\updownarrow} = 3\,154\,\mathrm{m}$ is about seven times larger than $\bar{\xi}_\tau^{\leftrightarrow} = 434\,\mathrm{m}$. Thus, for clouds with a prevailing directional structure it is advisable to give variable ξ_τ as a function of observation direction, e.g., by two parameters, $\xi_\tau^{\updownarrow}$ along and $\xi_\tau^{\leftrightarrow}$ across the prevailing cloud structure.

The resulting $\bar{\xi}_\tau^{\leftrightarrow}$ and $\bar{\xi}_\tau^{\updownarrow}$ of all measurement cases from CARRIBA and VERDI are summarized in Tab. 6.2. Additionally, $\bar{\xi}_\tau \pm \sigma_\xi$ are included ($\bar{\xi}_\tau^{\updownarrow} \pm \sigma_\xi, \bar{\xi}_\tau^{\leftrightarrow} \pm \sigma_\xi$). Those values illustrate the pixel by pixel variability for all calculated $P_\tau^2(L_{xy})$ along one direction. Due to the exponential behavior of $P_\tau^2(L_{xy})$ they are asymmetric with respect to $\bar{\xi}_\tau^{\updownarrow}$ and $\bar{\xi}_\tau^{\leftrightarrow}$.

Table 6.2: De–correlation length calculated for the retrieved fields of τ from CARRIBA (C-01 to C-04) and VERDI (V-01 to V-10). Vertical arrows ($\updownarrow$) indicate the calculation of $P_\tau^2(L_{xy})$ and subsequent derivation of ξ_τ along L_y, horizontal arrows ($\leftrightarrow$) along L_x. $\bar{\xi}_\tau$ is the average of all pixels, $\bar{\xi}_\tau - \sigma_\xi$ is the average minus standard deviation, and $\bar{\xi}_\tau + \sigma_\xi$ is the average plus standard deviation.

Parameter	C-01	C-02	C-03	C-04
$\bar{\xi}_\tau^{\updownarrow} - \sigma_\xi$ (km)	0.56	1.41	2.62	0.69
$\bar{\xi}_\tau^{\updownarrow}$ (km)	0.63	1.53	3.15	0.90
$\bar{\xi}_\tau^{\updownarrow} + \sigma_\xi$ (km)	0.75	1.67	3.83	1.24
$\bar{\xi}_\tau^{\leftrightarrow} - \sigma_\xi$ (km)	0.31	0.66	0.26	0.35
$\bar{\xi}_\tau^{\leftrightarrow}$ (km)	0.48	0.76	0.43	0.48
$\bar{\xi}_\tau^{\leftrightarrow} + \sigma_\xi$ (km)	0.88	0.86	0.80	0.76

Parameter	V-01	V-02	V-03	V-04	V-05	V-06	V-07	V-08	V-09	V-10
$\bar{\xi}_\tau^{\updownarrow} - \sigma_\xi$ (km)	0.16	0.19	0.24	0.08	0.11	0.13	0.16	0.12	0.08	0.09
$\bar{\xi}_\tau^{\updownarrow}$ (km)	0.19	0.28	0.25	0.09	0.13	0.21	0.24	0.23	0.11	0.15
$\bar{\xi}_\tau^{\updownarrow} + \sigma_\xi$ (km)	0.26	0.52	0.27	0.11	0.13	0.37	0.48	0.65	0.15	0.27
$\bar{\xi}_\tau^{\leftrightarrow} - \sigma_\xi$ (km)	0.04	0.07	0.06	0.04	0.03	0.03	0.05	0.06	0.02	0.04
$\bar{\xi}_\tau^{\leftrightarrow}$ (km)	0.06	0.10	0.10	0.06	0.05	0.05	0.08	0.09	0.04	0.06
$\bar{\xi}_\tau^{\leftrightarrow} + \sigma_\xi$ (km)	0.10	0.16	0.17	0.10	0.07	0.08	0.15	0.15	0.06	0.09

For CARRIBA, ξ_τ varies in a range from 434 to $3\,154\,\mathrm{m}$, depending on the cloud structure and inhomogeneity. The rather inhomogeneous cases C-01 and C-04 with highly variable τ_{ci}

on small scales yield rapidly decreasing $P_\tau^2(L_{\mathrm{xy}})$ with low $\bar\xi_\tau$. In contrast, the rather homogeneous cases C-02 and C-03 yield slowly decreasing $P_\tau^2(L_{\mathrm{xy}})$ and larger $\bar\xi_\tau$. The differences between $\bar\xi_\tau^{\updownarrow}$ and $\bar\xi_\tau^{\leftrightarrow}$ reach up to 85 %.

For the Arctic stratus fields observed during VERDI, $\bar\xi_\tau^{\updownarrow}$ and $\bar\xi_\tau^{\leftrightarrow}$ range between 35 m and 278 m and are significantly smaller (more inhomogeneous) than those from CARRIBA, although the inhomogeneity parameters from Tab. 6.1 yield similar values. This illustrates that the inhomogeneity parameters ρ_τ, S_τ, and χ_τ are not well suited to compare different types of clouds. A comparison can only indicate differences with regard to the evaluation of the horizontal dependence of cloud inhomogeneities. Comparably to the CARRIBA cases, the differences between $\bar\xi_\tau^{\updownarrow}$ and $\bar\xi_\tau^{\leftrightarrow}$ are significant as well. They reach up to 77 %.

6.3 Power Spectral Density Analysis

Multiple scattering in complex 3D microphysical cloud structures causes a smoothing of the reflected I_λ above clouds (Cahalan and Snider, 1989; Marshak et al., 1995). This effect causes uncertainties in the retrieved fields of τ, when homogeneous plan-parallel clouds are assumed in the retrieval algorithm. This smoothing effect is analyzed using the Fourier transform of the retrieved fields of τ. The application of Fourier transforms for the investigation of cloud inhomogeneities is most widely used in the existing literature (e.g., Cahalan, 1994; Davis et al., 1999; Schroeder, 2004). However, in most studies presented in literature, the 1D Fourier transformation is applied to time series of radiative quantities such as I_λ or γ_λ. Here, a 2D Fourier transformation is applied to spatial 2D cloud scenes. However, in Sect. 4.4 it was shown that features of the scattering phase functions are imprinted in the I_λ measurements of AisaEAGLE. To avoid artifacts in the Fourier transform arising from those features, fields of τ are used for the analysis, since they account for such scattering features.

The Fourier transformation decomposes a periodic function into a sum of sinusoidal base functions. For a given measurement signal, here $\tau(x, y)$, the 2D Fourier transform $\mathcal{F}_\tau(k_{\mathrm{x}}, k_{\mathrm{y}})$ is defined by:

$$\mathcal{F}_\tau(k_{\mathrm{x}}, k_{\mathrm{y}}) = \int_{-\infty}^{\infty} \int_{-\infty}^{\infty} \tau(x, y) e^{-2\pi \mathrm{i}(k_{\mathrm{x}} x + k_{\mathrm{y}} y)} \, \mathrm{d}x \, \mathrm{d}y, \tag{6.7}$$

with:

$$i = \sqrt{-1}. \tag{6.8}$$

Each of the base functions is described by a complex exponential of different frequency. The fields of τ are given as a function of horizontal distances x and y. Therefore, wave numbers $k_{\mathrm{x}} = 1/x$ and $k_{\mathrm{y}} = 1/y$ are used in the base functions.

For the calculation, the **D**iscrete **F**ourier **T**ransform (DFT) is applied. With n and m discrete elements x_{i} and y_{j} (τ of each pixel along and across swath), the 2D DFT is derived by:

$$\mathrm{DFT}(k_{\mathrm{x}}, k_{\mathrm{y}}) = \frac{1}{nm} \sum_{x_{\mathrm{i}}=0}^{n-1} \sum_{y_{\mathrm{j}}=0}^{m-1} \tau(x_{\mathrm{i}}, y_{\mathrm{j}}) \, e^{-2\pi \mathrm{i}(\frac{k_{\mathrm{x}} x_{\mathrm{i}}}{n} + \frac{k_{\mathrm{y}} y_{\mathrm{j}}}{m})}. \tag{6.9}$$

Figures 6.2 and 6.3 present the Fourier transform by the power spectral densities $E(k_x)$ and $E(k_y)$ (in the following called $E(k_{x,y})$), calculated from the complex Fourier coefficients by:

$$E(k_{x,y}) = \mathrm{DFT}^2(k_{x,y}) \qquad (6.10)$$

Figures 6.2a to 6.2c show τ_{ci} fields of three selected clouds (3.5 by 3.5 km) from the cases C-01, C-02, and C-03. C-01 represents an inhomogeneous cirrus without a preferred direction in the cloud structure (Fig. 6.2a). In C-02 a homogeneous cirrus with a slight directional structure (Fig. 6.2b) is selected while in C-03 an inhomogeneous cirrus with a distinct directional structure (Fig. 6.2c) is selected. Figure 6.2d to f show the corresponding 2D power spectral densities $E(k_{x,y})$.
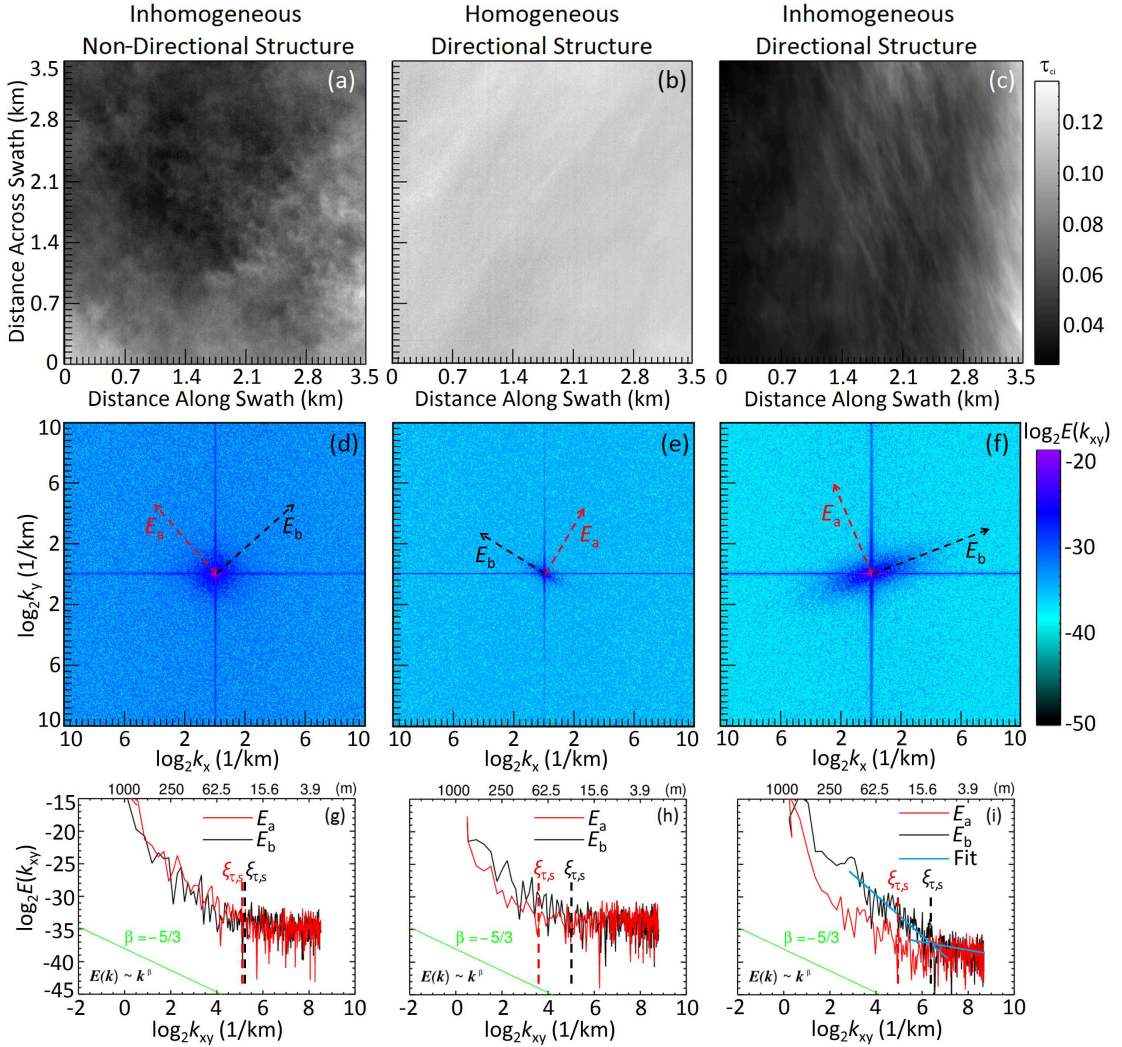
Figure 6.2: AisaEAGLE image (3.5 by 3.5 km), 2D power spectral density $E(k_{x,y})$, and 1D power spectral density $E(k_{x,y})$ along (black arrows, E_a) and across (red arrows, E_b) the prevailing direction of scale invariant areas for **(a),(d),(g)** inhomogeneous cloud without directional structure, **(b),(e),(h)** homogeneous cloud with slight directional structure, and **(c),(f),(i)** inhomogeneous cloud with distinct directional structure. The $\xi_{\tau,s}$ are marked with colored dashed lines.

Largest $E(k_{x,y})$ are found at smallest wave numbers $k_{x,y}$, which are located in the center of the image. The $E(k_{x,y})$ decrease with increasing $k_{x,y}$. Inhomogeneous clouds (Fig. 6.2d and f) show higher values of $E(k_{x,y})$ over a wide range of wave numbers $k_{x,y}$, whereas the larger $E(k_{x,y})$ for homogeneous clouds (Fig. 6.2e) are only located close to the smallest wave numbers $k_{x,y}$. Furthermore, the decrease of $E(k_{x,y})$ is rotational symmetrical for clouds with no preferred directional structure (Fig. 6.2d), but asymmetrical for clouds with a prevailing directional structure (Fig. 6.2e,f).

To study the symmetry, Fig. 6.2g to f show the $E(k_{x,y})$ along (black, E_a) and across (red, E_b) the direction of the longer symmetry axis. For the inhomogeneous case without a prevailing directional structure (C-01), both components E_a and E_a are almost identical. For the homogeneous case with a slight directional structure (C-02), both E_a and E_b are similar over most of the covered range of $k_{x,y}$, except for the smallest wave number $k_{x,y} < 3\,\mathrm{km}^{-1}$. For the inhomogeneous case with a distinct directional structure (C-03), both E_a and E_a are similar only at $k_{x,y} > 7\,\mathrm{km}^{-1}$. The differences in E_a and E_b for the clouds with a prevailing directional structure result from the different $k_{x,y}$, at which the signal turns into white noise (constant $E(k_{x,y})$, independent on $k_{x,y}$). This transition is used to characterize the small-scale break $\xi_{\tau,s}$, which determines the lower size range of the detected cloud inhomogeneities (respectively instruments resolution, if $\xi_{\tau,s}$ is smaller than the pixel size). To derive $\xi_{\tau,s}$, fits are applied to the two scale-invariant regimes of $E(k_{x,y})$ (exemplary shown for E_b in Fig. 6.2i). Subsequently, the small scale break $\xi_{\tau,s}$ is determined by the intersection of those fits. The corresponding $k_{x,y}$ give $\xi_{\tau,s}$. $\xi_{\tau,s}(E_a)$ and $\xi_{\tau,s}(E_b)$ for case C-01 are at about 0.03 km. $\xi_{\tau,s}(E_a)$ and $\xi_{\tau,s}(E_b)$ of Case C-02 are at about 0.09 and 0.03 km, respectively. $\xi_{\tau,s}(E_a)$ from case C-03 is at about 0.03 km, while $\xi_{\tau,s}(E_b)$ is at about 0.01 km, which is already close to the pixel size. Thus, $\xi_{\tau,s}$ yields quantitatively larger values along the prevailing cloud structure than across the prevailing structure.

Marshak et al. (1995) discussed that cloud inhomogeneity and horizontal photon transport are scale–dependent processes. The $E(k_{x,y})$ of cloud optical and microphysical are proportional to $k_{x,y}^{\beta}$. At large scales, the $E(k_{x,y})$ of e.g. I_λ, τ, LWC, or IWC follow Kolmogorov's $\beta = -5/3$ law of energy distribution in a turbulent fluid (Kolmogorov, 1941). For homogeneous clouds without horizontal photon transport, $E(k_{x,y})$ follows $\beta = -5/3$ for all $k_{x,y}$. In that case the variability in the radiation field follows the variability in LWC. Increasing cloud inhomogeneity causes a decrease of β of optical properties for smaller scales (typically $< 1000\,\mathrm{m}$), but not in β of microphysical properties. Due to horizontal photon transport the slope of the optical quantities (I_λ, τ) differs from the slope of the microphysical properties (LWC, IWC). In the following, the horizontal scale, at which the power spectra starts to deviate from the -5/3 law defines the large-scale break $\xi_{\tau,L}$. $\xi_{\tau,L}$ depends on the size of the horizontal cloud structures; more inhomogeneous clouds with larger variability on smaller scales yield smaller $\xi_{\tau,L}$. For scales smaller than $\xi_{\tau,L}$, the radiative smoothing leads to uncertainties in 1D cloud retrievals, which not account for the horizontal photon transport Cahalan (1994); Marshak et al. (1998); Zinner et al. (2006); Varnai and Marshak (2007).

A comparison of the depicted $E(k_{x,y})$ to the -5/3 law in Fig. 6.2g to h shows that the selected cirrus cases do not contain the larger scales, which are necessary to identify $\xi_{\tau,L}$. The depicted $E(k_{x,y})$ belong to $k_{x,y}$ lower than $\xi_{\tau,L}$, which already exhibit a steeper slope

than $\beta = -5/3$. Therefore, the size of the selected areas is suitable to identify quantitative values for $\xi_{\tau,s}$, but for deriving $\xi_{\tau,L}$, larger fields of τ have to be considered. Unfortunately, this is only possible for calculations of the DFT along L_y (across swath). Calculations along L_x (swath) do not cover a sufficiently large distance to derive quantitative values for $\xi_{\tau,L}$. Therefore, the following analysis is performed using 1D DFT along L_y only. To evaluate the resulting 1D Fourier spectra with reduced noise (rn) characteristics, the $E_{rn}(k) \sim k^\beta$ are calculated with the use of octave binning, following the method proposed by Davis et al. (1996), Harris et al. (1997), and Schroeder (2004). Here, for the total number N of $E(k_y)$ the binning of k_y is specified by factors of 2^n with $n = 0,1,...,\log_2(N-2)$. Using those factors, bins for the wave numbers are generated and the corresponding $E(k_y)$ within the particular bin size averaged. In addition to the reduced noise of $E(k_{rn})$ compared to $E(k_y)$ the binning provides a uniformly contribution of all scales to the average values.

Figure 6.3a and b show the 1D DFT calculated across the swath for two typical cases of cirrus (CARRIBA case C-01) and Arctic stratus (VERDI case V-07). The two cases are selected, since they exhibit a similar length L_y. For each line of the τ field (each swath pixel) $E(k_y)$ is calculated and the individual power spectra are overlayed as gray dots in Fig.6.3. The $E(k_{rn})$ derived from the octave binning are included as black squares. They provide the supporting points for the slope fits. A green line indicates the $\beta = -5/3$ law.
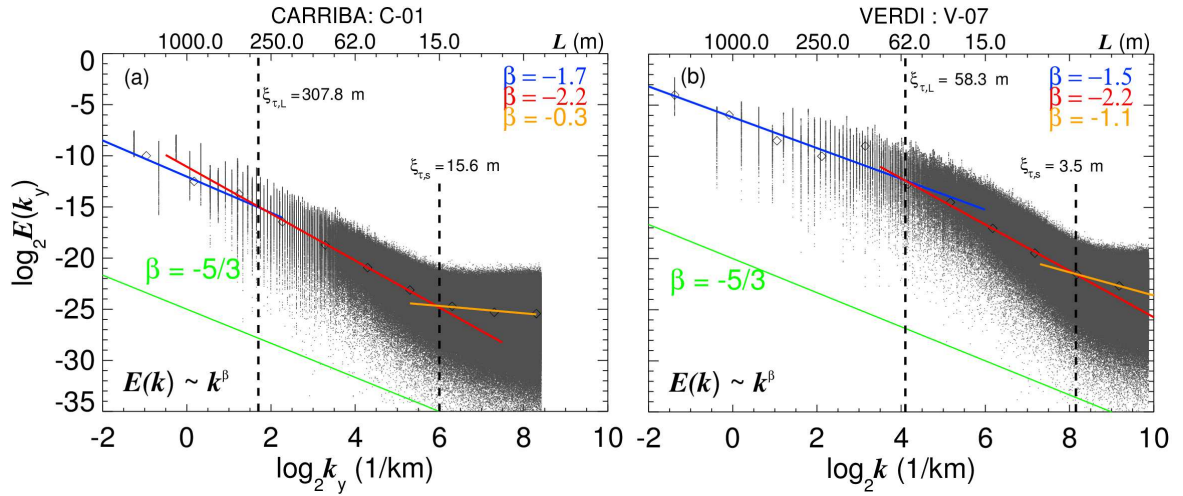
Figure 6.3: 1D power spectral density $E(k_y)$ (gray dots) for each spatial pixel on the swath axis of the τ field from **(a)** case C-01 and **(b)** case V-07. Scale-invariant slopes β are marked with colored solid lines. The $E(k_{rn})$ derived from the octave binning are included as black squares. Scale breaks $\xi_{\tau,L}$ and $\xi_{\tau,s}$ are indicated by dashed lines.

For large scales, the $E_{rn}(k_y)$ (blue fit) approximately follow the $-5/3$ relation in both cases. The large-scale break $(\xi_{\tau,L})$ is evident at the intersection between the blue and the red line. Here, the slope in the $E_{rn}(k_y)$ becomes steeper. For the CARRIBA case $\xi_{\tau,L}$ yields $0.31\,\text{km}$ and the middle scale slope β_m decreases to -2.2. $\xi_{\tau,L}$ for the VERDI case yields $0.06\,\text{km}$ and β_m decreases to 2.2. The middle–scale slope β_m is a function of the inhomogeneity in the measured signals. With increasing inhomogeneity of the optical thickness τ, β_m decreases. Together with the smaller $\xi_{\tau,L}$, this indicates that the stratus cloud of the VERDI case is

more inhomogeneous compared to the cirrus cloud. As discussed above, $\xi_{\tau,\mathrm{s}}$ is observed at the intersection between the fits for the middle (red, β_{m}) and small scales (orange, β_{s}). Due to the analysis of a significant larger distance compared to Fig. 6.2, it is highly uncertain to give quantitative numbers for $\xi_{\tau,\mathrm{s}}$. Therefore, it is indicated only qualitatively.

Table 6.3 summarizes the $\xi_{\tau,\mathrm{L}}$ for all available cloud cases from CARRIBA and VERDI. The values compare well with the de-correlation length ξ_τ derived in Sect. 6.2. Although the exact values of $\xi_{\tau,\mathrm{L}}$ are not equal to ξ_τ, both are in the same size range for each individual case. Similar to ξ_τ given in Tab. 6.2, $\xi_{\tau,\mathrm{L}}$ indicates that C-02 and C-03 are more homogeneous than C-01 and C-04. In general it was found that the cirrus observed during CARRIBA are more homogeneous than the Arctic stratus from VERDI.

Table 6.3: Scale breaks $\xi_{\tau,\mathrm{L}}$ calculated along L_y for the retrieved fields of τ from CARRIBA (C-01 to C-04) and VERDI (V-01 to V-10).

	C-01	C-02	C-03	C-04						
$\xi_{\tau,\mathrm{L}}$ (km)	0.31	1.30	2.83	0.20						

	V-01	V-02	V-03	V-04	V-05	V-06	V-07	V-08	V-09	V-10
$\xi_{\tau,\mathrm{L}}$ (km)	0.16	0.11	0.19	0.17	0.12	0.10	0.06	0.12	0.19	0.13

7 Summary and Conclusions

During the two international field campaigns CARRIBA and VERDI, downward and upward solar spectral radiance ($I_\lambda^\downarrow$, $I_\lambda^\uparrow$) were measured with high spatial resolution ($< 10\,\mathrm{m}$), using the imaging spectrometer AisaEAGLE. The instrument was carefully characterized and calibrated in the laboratory and the procedure of data evaluation (dark current correction, calibrations, smear correction) was described. It was shown that the dark current and smear correction should always be taken into account (calibration included). Furthermore, based on the given measurement geometry the scattering angle ϑ of the incident I_λ were calculated and allocated to each spatial pixel.

The measured fields of $I_\lambda^\downarrow$ and $I_\lambda^\uparrow$ from CARRIBA and VERDI were used to retrieve fields of τ with high spatial resolution ($< 10\,\mathrm{m}$). To derive the fields of τ, different methods for CARRIBA and VERDI were derived and applied. For the cirrus observed during CARRIBA, the most probable crystal shape was derived. For the Arctic stratus observed during VERDI, the sea-ice albedo complicated the retrievals of τ_{st}. The influence of the highly reflecting sea ice as well as large albedo contrasts on the retrieval of τ_{st} were investigated.

The derived fields of τ from CARRIBA and VERDI were used to quantify horizontal cloud inhomogeneities. Parts of this chapter were already published in Schäfer et al. (2013) and Schäfer et al. (2015).

7.1 Subtropical Cirrus Optical Thickness Retrieval from Ground–Based Observations

The cirrus optical thickness τ_{ci} was retrieved from ground–based AisaEAGLE $I_\lambda^\downarrow$ measurements. Based on four cases collected during CARRIBA on Barbados in 2011, the feasibility of retrieving τ_{ci} at high spatial resolution was demonstrated. A preliminary characterization of the cirrus inhomogeneity using the average and standard deviation, as well as frequency distributions was performed. The cirrus observed on 16 and 18 April 2011 was quite homogeneous with mean τ_{ci} of 0.28 and 0.20 and coefficients of variation of 0.09 and 0.03. On 9 and 23 April 2011 rather inhomogeneous cirrus with mean τ_{ci} of 0.41 and 0.05 and coefficients of variation of 0.17 and 0.04 was observed.

The sensitivity of the retrieval method with respect to surface albedo, effective radius, cloud altitude, and ice-crystal shape was characterized by varying the model input parameters. Largest sensitivities of the retrieved τ_{ci} have been found with respect to the surface albedo and the ice-crystal shape with up to $30\,\%$ and $90\,\%$ differences. The sensitivities of the

retrieved τ_{ci} with respect to effective radius ($\leq 5\%$) and cloud altitude ($\leq 0.5\%$) are comparably small. This indicates that accurate knowledge of the surface albedo and ice-crystal shape is required to reliably retrieve cirrus optical thickness with AisaEAGLE. However, the determination of the ice-crystal shape is complicated without in situ measurements inside the cirrus. AisaEAGLE measures radiance as a function of a wide range of scattering angles. Therefore, it provides information about the scattering phase function. An evaluation of ice crystal shape is obtained by comparing the radiance measured by AisaEAGLE to simulations and all-sky images. It is possible to distinguish between hexagonal ice crystals that produce the typical $22°$ halo and irregular ice crystals that do not. The shape retrieval is limited to a narrow range of scattering angles, which does not always cover the halo.

Therefore, the optimum way to operate AisaEAGLE in a ground-based application with a large coverage of scattering angles is to adjust the sensor line along the azimuthal direction of the Sun. In this way, the maximum possible range of the scattering phase function is detected. However, due to a variable wind direction the clouds may not head perpendicular across the sensor line, which causes then a spatial distortion of the cloud shape. For slow moving cirrus and the assumption that the crystal shape stays constant over the time period of measurements, two measurements can be combined; using at first an orientation of the sensor line along the azimuthal direction of the Sun to detect the scattering phase function and varying afterwards the orientation of the sensor line perpendicular to the heading of the cirrus. For fast moving cirrus, a compromise has to be made between the maximum possible range of detectable scattering angles or measurements without spatial distortion of the cloud field.

7.2 Arctic Stratus Cloud Retrieval from Airborne Observations

During VERDI, carried out in Inuvik, Canada in 2012, the AisaEAGLE measurements of $I_\lambda^\uparrow$ were performed from an aircraft. In combination with the nadir pointing SMART-Albedometer, the reflectivity γ_λ was derived. Measurements above clouds in situations with heterogeneous surface albedo were analyzed in order to retrieve τ_{st}. Due to the high contrast in the surface albedo of sea ice and open water, the data showed a distinct difference between γ_λ above water and sea-ice surfaces. This transition was used to establish a sea–ice mask. Threshold values for γ_λ derived from both measurements and radiative transfer simulations are in good agreement.

In the vicinity of ice edges, γ_λ is reduced/enhanced above the bright sea ice/dark ocean surface. This is related to 3D effects, which result from isotropic reflection on the bright sea ice, which causes horizontal photon transport, before the radiation is scattered by cloud particles into the direction of observation. To quantify the uncertainties of the cloud retrieval in such areas of open water close to ice floes, γ_λ measurements from the VERDI campaign were analyzed using 3D radiative transfer simulations for a cloudless case and clouds of $\tau_{st} = 1/5/10$ located above various, idealized surface albedo fields. Two distances ΔL_{HPT} and ΔL were defined to characterize the extent of the horizontal photon transport (ΔL_{HPT}) and to estimate the distance to the ice edge (ΔL) within which the retrieval of τ_{st} and r_{eff} is biased stronger by the 3D effects than by measurement uncertainties.

From the measurement cases ($\tau_{\mathrm{st}} = 5$, $h_{\mathrm{cloud}} = 0$–$200\,\mathrm{m}$), a distance ΔL of $400\,\mathrm{m}$ was derived. Radiative transfer simulations, adapted to the observed cloud and sea-ice situation, confirmed this value. For the case of the infinitely straight ice edge, a distance $\Delta L_{\mathrm{HPT}} = 100\,\mathrm{m}/250\,\mathrm{m}/300\,\mathrm{m}$ was found for $\tau_{\mathrm{st}} = 1/5/10$. The increase of ΔL_{HPT} shows that the horizontal photon transport is increasing with increasing τ_{st}. However, the minimum distance ΔL to the ice edge, where a 1D cloud retrieval can be applied, is decreasing with increasing τ_{st} ($\Delta L = 600\,\mathrm{m}/400\,\mathrm{m}/250\,\mathrm{m}$ at $\tau_{\mathrm{st}} = 1/5/10$) due to the stronger impact of measurement uncertainties in the case of thicker clouds (higher γ_λ).

The simulations did not show significant differences of ΔL_{HPT} and ΔL assuming various r_{eff} between 10–$30\,\mu\mathrm{m}$. Besides cloud properties, the influence of the magnitude of the albedo contrast was tested. Varying the simulated surface albedo of the bright sea ice and dark ocean water by $\pm 6\,\%$, ΔL_{HPT} and ΔL were found to vary by $< 1\,\%$, which is less than the measurement uncertainty of $6\,\%$. This indicates that ΔL_{HPT} and ΔL are robust measures to quantify the horizontal extent of the 3D radiative effect at various albedo contrasts.

The cloud altitude and cloud geometrical thickness significantly influence ΔL. The distance ΔL increases linearly with increasing cloud base altitude (for $\tau_{\mathrm{st}} = 5$ from 800 to $3200\,\mathrm{m}$ for a $500\,\mathrm{m}$ thick cloud with cloud base at 0 and $1500\,\mathrm{m}$). The same increase of ΔL holds for an increasing cloud geometrical thickness (for $\tau_{\mathrm{st}} = 5$ from 300 to $2000\,\mathrm{m}$ for a 200 and $1500\,\mathrm{m}$ thick cloud). Therefore, the cloud base altitude and geometrical thickness have to be known while performing 3D radiative transfer simulations of clouds above ice edges.

To investigate changes in the 3D radiative effect due to variations in the ice-edge length or sea-ice area, area-averaged γ_λ were calculated for different idealized cases of sea-ice distributions. A larger enhancement of the area-averaged γ_λ was found for longer ice-edge lengths. Changes in the sea-ice area are of less importance. Placing the ice floes directly next to each other, an enhancement of the area-averaged γ_λ was found as well, although the sea-ice area and ice-edge length remained the same.

For the direct comparison of simulation and measurement, an observed ice-floe field was modeled. The frequency distributions of observations and simulations agree within the measurement uncertainties. The area-averaged γ_λ showed stronger 3D effects for the real case compared to the idealized cases simulated before. A quantification of the 3D radiative effect in clouds above ice edges is only simulated if realistic surface albedo fields are applied. However, a parameterization of the influence of individual parameters is only possible by using such simplified surface albedo fields.

The results from the simulations suggest that applying a 1D cloud retrieval to airborne measurements taken over ocean areas located close to sea ice edges will result in an overestimation of τ_{st} and r_{eff} and the overestimation will increase with proximity to the ice edge. This overestimation was calculated for a liquid water cloud with $\tau_{\mathrm{st}} = 10.0$ and $r_{\mathrm{eff}} = 15\,\mu\mathrm{m}$. In that case, the overestimation of the retrieved τ_{st} reaches up to a distance of $1.5\,\mathrm{km}$ from the ice edge, with a maximum overestimation of $90\,\%$ directly beside the ice edge. For r_{eff}, an overestimation of $30\,\%$ was found in the direct vicinity of the ice edge. 3D influences on the retrieval of r_{eff} are observable up to a distance of $1\,\mathrm{km}$ from the ice edge. This is

slightly lower compared to the distance where τ_st is biased, which indicates that the 3D effect depends on wavelength.

An important implication from Chapter 5 is that only γ_λ measurements far away from any ice edge were used for a subsequent retrieval of τ_st. Thus, with the help of the distance ΔL, ten sections of AisaEAGLE radiance measurements with average swath of 1.3 km and lengths of 4 to 26 km were identified, which were not biased by a highly reflecting sea-ice albedo or by large albedo contrasts. The average of τ_st of all cases gave values of $3 < \bar\tau_\mathrm{st} < 14$ with most $\bar\tau_\mathrm{st}$ between 3 to 7 and σ_τ in the range of 15 to 34 % of $\bar\tau_\mathrm{st}$. A sensitivity study applied to the retrieval method of τ_st gave uncertainties in the range of 6.2 to 6.5 %, mostly related to the uncertainty in the radiometric calibration. Thus, sufficiently large areas of the clouds were covered to provide good statistics on the evaluation of τ_st with regard to the evaluation of cloud inhomogeneities.

7.3 Cloud Inhomogeneity Analysis

The investigation of cloud inhomogeneity was performed for the retrieved τ from four cirrus cases collected during CARRIBA and from ten Arctic stratus cases collected during VERDI. The cloud inhomogeneity was analyzed by three common 1D inhomogeneity parameters ρ_τ, S_τ, and χ_τ, with auto–correlation functions, and Fourier analysis.

The results from the calculated inhomogeneity parameters ρ_τ and S_τ are in agreement with values given in the literature for similar cloud types. The calculated ρ_τ are in the range of 0.17–0.91 for CARRIBA and 0.15–0.34 for VERDI. The literature values are in the range of 0.07–0.78 (except C-04, $\rho_\tau = 0.91$). The inhomogeneity parameter S_τ exhibits values of 0.08 to 0.48 for CARRIBA and 0.07 to 0.20 for VERDI. Literature values are in the range of 0.03 to 0.3. For χ_τ, the literature estimates values between ≈ 0.65 and 0.8. Here, the difference to the results from CARRIBA and VERDI is larger. All values except for C-04 ($\chi_\tau = 0.63$) are in the range between 0.92 and 0.99. A further intercomparison between CARRIBA and VERDI showed that all three inhomogeneity parameters gave values of similar magnitude for both cloud cases; cirrus and Arctic stratus.

The analysis using auto–correlation functions $P_\tau(L_\mathrm{xy})$ showed that an intercomparison of cirrus inhomogeneities with inhomogeneities in Arctic stratus are not suitable, using the inhomogeneity parameters ρ_τ, S_τ, and χ_τ. For both cloud cases the inhomogeneity parameters gave similar values, but significant differences resulting from the analysis of $P_\tau(L_\mathrm{xy})$, which additionally contain information on the horizontal structure of cloud inhomogeneities. Therefore, to compare the inhomogeneities of different cloud types, their horizontal structure has to be taken into account. From the squared auto–correlation functions $P_\tau^2(L_\mathrm{xy})$ the de–correlation length ξ_τ was derived, which is a measure of the size range of the cloud inhomogeneities. The 2D analysis of $P_\tau^2(L_\mathrm{xy})$ revealed that ξ_τ is a function of the directional structure of the cloud inhomogeneities. Without knowledge about the directional structure of cloud inhomogeneities, no universally valid value for ξ_τ can be derived from the retrieved fields of τ. The differences in ξ_τ as derived from a 1D auto–correlation analysis along and

across the prevailing structure of cloud inhomogeneities reached up to 85 and 77 % for CAR-RIBA and VERDI. Thus, the directional cloud structure has to be taken into account for a quantification of cloud inhomogeneities. The absolute values of ξ_τ were in the range of 0.43 to 3.15 km for CARRIBA and 0.04 to 0.28 km for VERDI.

Due to a complex 3D microphysical cloud structure, multiple scattering causes a smoothing of the reflected I_λ field of the cloud. This generates a smoothing effect of the retrieved fields of τ, which is evident from scale analysis. This effect was quantified using 2D Fourier transformation applied to the retrieved fields of τ. From the resulting power spectral densities $E(k_{x,y})$, evidence of 3D radiative effects were found for both cloud types, cirrus and Arctic stratus. For larger scales, the $E(k_{x,y})$ followed Kolmogorov's -5/3 law. Approaching smaller scales, the slope became steeper indicating radiative smoothing until it turned into white noise for scales smaller than the lower size of cloud inhomogeneities. From the intersection of fits of the three slope regimes, the small-scale break $\xi_{\tau,s}$ (between small- and middle-scale slopes) and the large-scale break $_{\tau,L}$ (between middle- and large-scale slopes) were derived. Similarly to the analysis using auto–correlation functions, $\xi_{\tau,s}$ depends on the directional structure of the cloud inhomogeneities. $\xi_{\tau,s}$ determines the smallest resolved size of cloud inhomogeneities (0.01 to 0.09 km in the evaluated cases). Due to a too small swath width, a similar analysis for $\xi_{\tau,L}$ could not be performed. However, the calculated $\xi_{\tau,L}$ along the image are comparable to the results derived from the analysis of $P_\tau(L_{xy})$. $\xi_{\tau,L}$ for CARRIBA was in the range of 0.20 to 2.83 km. For VERDI a range of 0.06 to 0.19 km was covered by $\xi_{\tau,L}$.

In early studies, by e.g. Marshak et al. (1998) or Schroeder (2004), the scale dependence of cloud radiation measurements was analyzed along one direction (time series) using 1D DFT. However, the resulting $E(k)$ are only valid for the particular observation direction along the given path. Due to prevailing wind directions, clouds tend to evolve directional structures. In such cases, the calculated $E(k)$, β, and $\xi_{\tau,s}$ will only be valid for the whole cloud if the cloud structure exhibits a non-directional character (compare Fig. 6.2d to f). In all other cases, significant differences are expectable. Therefore, the directional structure of cloud inhomogeneities has always to be taken into account. Imaging spectrometers such as AisaEAGLE help to identify and analyze the prevailing directional structure of cloud inhomogeneities.

7.4 Perspectives

The assessment of the crystal shape is restricted to the narrow FOV (36.7°) of the AisaEAGLE lens. The detected ϑ-range will be increased using a wide-angle lens (58°) and a scanning version of AisaEAGLE, installed on an astrophysical mount. The additional angular information will allow to develop a cirrus retrieval technique considering the crystal shape. This will significantly decrease the retrieval uncertainty. Furthermore, a scanning version of AisaEAGLE will reduce spatial distortions in the images, because the scans are then not anymore restricted to the heading of the clouds.

Up to now, the spectral range of the collected fields of I_λ was restricted to the visible wavelength range ($400\,\text{nm} \leq \lambda \leq 1\,000\,\text{nm}$). Therefore, a retrieval of r_{eff} could not be performed. In future studies, this wavelength range will be extended to the near-infrared wavelength region ($1\,000\,\text{nm} \leq \lambda \leq 2\,500\,\text{nm}$) using collocated measurements with the imaging spectrometer AisaHAWK. Those measurements will also cover absorbing wavelengths, which are sensitive to r_{eff}. Furthermore, the extended wavelength range will allow to adopt the multispectral cloud retrieval from Brückner et al. (2014) to the imaging spectrometer measurements. This will avoid ambiguities in the simulations.

The cloud retrievals from the VERDI data were restricted to measurements over open ocean with a sufficiently large distance to the next ice edge. Therefore, only a limited number of cases was available, for which a retrieval of τ_{st} could be applied. In April 2014, the international measurement campaign RACEPAC (**R**adiation-**A**erosol-**C**loud **ExP**eriment in the **A**rctic **C**ircle) was carried out in Inuvik, Canada. Here, similar measurements compared to VERDI were performed using the AWI aircraft Polar 5 and 6. While Polar 6 performed in situ measurements inside the clouds, collocated radiation measurements were performed with Polar 5. Thus, more data are available to investigate inhomogeneities of Arctic stratus. Furthermore, single-particle imaging probes such as SID-3 (**S**mall **I**ce **D**etector) or HALO-Holo (**Holo**graphic single-particle imager, intially designed for **H**igh **A**ltitude and **LO**ng range research aircraft) were installed aboard P 6, which allow comparisons to retrieved crystal shapes. In addition, during the project AC^3 (**A**rcti**C** **A**mplification: **C**limate Relevant **A**tmospheric and Surfa**C**e Processes and Feedback Mechanisms), more investigations with regard to cloud inhomogeneities in Arctic stratus will be performed. A series of airborne, ship- and ground-based measurements are planned. Here, the findings from VERDI and RACEPAC with regard to 3D radiative effects, which are caused by an inhomogeneous surface albedo, will be further investigated and additionally linked to satellite observations.

So far, the investigations were performed for cirrus and Arctic stratus. Different clouds will exhibit different structures and magnitudes of inhomogeneities. Extending the investigations to a wider field of different cloud types will increase insights to effects related to cloud inhomogeneities. Accordingly, measurements of cloud sides from deep convective cumulus using airborne visible and near-infrared imaging spectrometers such as AisaEAGLE and AisaHAWK were recently performed during the international field campaign ACRIDICON-CHUVA (**A**erosol, **C**loud, Precipitation, and **R**adiation **I**nteractions and **D**ynam**I**cs of **CON**vective Cloud Systems - **C**loud processes of t**H**e main precipitation systems in Brazil: A contrib**U**tion to cloud resol**V**ing modeling and to the GPM (Glob**A**l Precipitation Measurement)) in Manaus, Brazil in 2014 (Wendisch et al., 2016). Here, due to the convective character and different phases, larger 3D effects are expected.

Bibliography

Anderson, G., Clough, S., Kneizys, F., Chetwynd, J., and Shettle, E.: AFGL Atmospheric Constituent Profiles (0–120 km), Tech. Rep. AFGL-TR-86-0110, AFGL (OPI), Hanscom AFB, MA 01736, 1986.

Anger, C., Mah, S., and Babey, S.: Technological enhancements to the Compact Airborne Spectrographic Imager (CASI), in Proceedings of the Second International Airborne Remote Sensing Conference and Exhibition, 12-15 September, Strasbourg, France, pp. 205–214, 1994.

Armstrong, E. and Vazquez-Cuervo, J.: A new global satellite-based sea-surface temperature climatology, Geophys. Res. Lett., 28, 4199–4202, 2001.

Baran, A. J.: From the single-scattering properties of ice crystals to climate prediction: A way forward, Atmos. Res., 112, 45–69, 2012.

Baum, B. A., Heymsfield, A. J., Yang, P., and Bedka, S. T.: Bulk scattering properties for the remote sensing of ice clouds. Part I: Microphysical data and models, J. Appl. Meteor., 44, 1885–1895, 2005a.

Baum, B. A., Yang, P., Heymsfield, A. J., Platnick, S., King, M. D., Hu, Y. X., and Bedka, S. T.: Bulk scattering properties for the remote sensing of ice clouds. Part II: Narrowband models, J. Appl. Meteor., 44, 1896–1911, 2005b.

Baum, B. A., Yang, P., Nasiri, S., Heidinger, A. K., Heymsfield, A., and Li, J.: Bulk scattering properties for the remote sensing of ice clouds. Part III: High-resolution spectral models from 100 to 3250 cm^{-1}, J. Appl. Meteor., 46, 423–434, 2007.

Bierwirth, E., Ehrlich, A., Wendisch, M., Gayet, J.-F., Gourbeyre, C., Dupuy, R., Herber, A., Neuber, R., and Lampert, A.: Optical thickness and effective radius of Arctic boundary-layer clouds retrieved from airborne nadir and imaging spectrometry, Atmos. Meas. Tech., 6, 1189–1200, 2013.

Bohren, C. F. and Clothiaux, E. E.: Fundamentals of Atmospheric Radiation, Wiley-VCH Verlag GmbH & Co. KGaA, Weinheim, 2006.

Bohren, C. F. and Huffman, D. R.: Absorption and Scattering of Light by Small Particles, Wiley-Interscience, New York, 1998.

Bowker, D., Davis, R., Myrick, D., Stacy, K., and Jones, W.: Spectral reflectances of natural targets for use in remote sensing studies, NASA RP-1139, NASA Langley Research Center, Hampton (VA), USA, 1985.

Brenguier, J.-L., Burnet, F., and Geoffroy, O.: Cloud optical thickness and liquid water path. Does the k coefficient vary with droplet concentration?, Atmos. Chem. Phys., 11, 9771–9786, doi:10.5194/acp–11–9771–2011, 2011.

Brückner, M., Pospichal, B., Macke, A., and Wendisch, M.: A new multispectral cloud retrieval method for ship-based solar transmissivity measurements, J. Geophys. Res., 119, 11.338–11.354, 2014.

Cahalan, R.: Bounded cascade clouds: albedo and effective thickness, Nonlin. Proc. Geophys., 1, 1994.

Cahalan, R. and Snider, J.: Marine stratocumulus structure, Remote Sens. Environ., 28, 95–107, 1989.

Chandrasekhar, S.: Radiative Transfer, Oxford University Press, London, UK, 1950.

Chepfer, H., Goloub, P., Riedi, J., De Haan, J. F., Hovenier, J., and Flamant, P.: Ice crystal shapes in cirrus clouds derived from POLDER/ADEOS-1, J. Geophys. Res., 106, 7955–7966, 2001.

Chepfer, H., Minnis, P., Young, D., Nguyen, L., and Arduini, R. F.: Estimation of cirrus cloud effective ice crystal shapes using visible reflectances from dual-satellite measurements, J. Geophys. Res., 107, 4730, 2002.

Choi, Y.-S. and Ho, C.-H.: Radiative effect of cirrus with different optical properties over the tropics in MODIS and CERES observations, Geophys. Res. Lett., 33, doi:10.1029/2006GL027 403, 2006.

Comstock, J. M., d'Entremont, R., DeSlover, D., Mace, G. G., Matrosov, S. Y., McFarlane, S. A., Minnis, P., Mitchell, D., Sassen, K., Shupe, M. D., Turner, D. D., and Wang, Z.: An intercomparison of microphysical retrieval algorithms for upper-tropospheric ice clouds, Bull. Amer. Meteor. Soc., 88, 191–204, 2007.

Cracknell, A. P.: Advanced very high resolution radiometer AVHRR, CRC Press, 1997.

Davis, A., Marshak, A., Wiscombe, W., and Cahalan, R.: Scale invariance in liquid water distributions in marine stratocumulus. Part I: Spectral properties and stationarity issues, J. Atmos. Sci., 53, 1538–1558, 1996.

Davis, A., Cahalan, R., Spinhirne, D., McGill, M., and Love, S.: Off-beam Lidar: an emerging technique in cloud remote sensing based on radiative green-function theory in the diffusion domain, Phys. Chem. Earth, 24, 177–185, 1999.

Edwards, J., Havemann, S., Thelen, J.-C., and Baran, A.: A new parametrization for the radiative properties of ice crystals: Comparison with existing schemes and impact in a GCM, Atmos. Res., 83, 19 – 35, 2007.

Ehrlich, A., Bierwirth, E., Wendisch, M., Herber, A., and Gayet, J. F.: Airborne hyperspectral observations of surface and cloud directional reflectivity using a commercial digital camera, Atmos. Chem. Phys., 12, 3493–3510, 2012.

Eichler, H., Ehrlich, A., Wendisch, M., Mioche, G., Gayet, J.-F., Wirth, M., Emde, C., and Minikin, A.: Influence of ice crystal shape on retrieval of cirrus optical thickness and effective radius: A case study, J. Geophys. Res., 114, D19203, 2009.

Ewald, F., Kölling, T., Baumgartner, A., Zinner, T., and Mayer, B.: Design and characterization of specMACS, a multipurpose hyperspectral cloud and sky imager, Atmos. Meas. Tech. Discuss., 8, 9853–9925, 2015.

Feister, U. and Grewe, R.: Spectral albedo measurements in the UV and visible region over different types of surfaces, Photochem. Photobiol., 62, 736–744, 1995.

Finger, F., Werner, F., Klingebiel, M., Ehrlich, A., Jäkel, E., Voigt, M., Borrmann, S., Spichtinger, P., and Wendisch, M.: Spectral optical layer properties of cirrus from collocated airborne measurements Ű a feasibility study, Atmos. Chem. Phys. Discuss., 15, 19 045–19 077, 2015.

Francis, P., Hignett, P., and Macke, A.: The retrieval of cirrus cloud properties from aircraft multi-spectral reflectance measurements during EUCREX '93, Quart. J. Roy. Meteor. Soc., 124, 1273–1291, 1998.

Fu, Q. and Liou, K.: Parameterization of the radiative properties of cirrus clouds, J. Atmos. Sci., 50, 2008–2025, 1993.

Garrett, T. J., Gerber, H., Baumgardner, D. G., Twohy, C. H., and Weinstock, E. M.: Small, highly reflective ice crystals in low-latitude cirrus, Geophys. Res. Lett., 30, doi:10.1029/2003GL018 153, 2003.

Geleyn, J. F. and Hollingsworth, A.: An economical, analytical method for the computation of the interaction between scattering and line absorbtion of radiation, Contr. Atmos. Phys., 52, 1–16, 1979.

Grenfell, T. C. and Warren, S. G.: Representation of a nonspherical ice particle by a collection of independent spheres for scattering and absorption of radiation, J. Geophys. Res., 104, 31.697–31.709, 1999.

Grosvenor, D. P. and Wood, R.: The effect of solar zenith angle on MODIS cloud optical and microphysical retrievals within marine liquid water clouds, Atmos. Chem. Phys., 14, 7291–7321, 2014.

Gueymard, C. A.: The sun's total and spectral irradiance for solar energy applications and solar radiation models, Sol. Energy, 76, 423–453, 2004.

Hanus, J., Malenovsky, Z., Homolova, L., Veroslav, K., Petr, L., and Pavel, C.: PPotential of the VNIR Airborne hyperspectral system AISA Eagle, in: Symposium GIS Ostrava, (CZ), 2008.

Harris, D., Seed, A., Menabde, M., and Austin, G.: Factors affecting multiscaling analysis of rainfall time series, Nonlin. Proc. Geophys., 4, 137–156, 1997.

Hess, M., Koelemeijer, R., and Stammes, P.: Scattering matrices of imperfect hexagonal ice crystals, J. Quant. Spectrosc. Radiat. Transfer, 60, 301–308, 1998.

Hill, P. G., Hogan, R. J., Manners, J., and Petch, J. C.: Parametrizing the horizontal inhomogeneity of ice water content using CloudSat data products, Q. J. R. Meteorol. Soc., 138, 1784–1793, 2012.

Hogan, R. and Illingworth, A.: Deriving cloud overlap statistics from radar, Q. J. R. Meteorol. Soc., 126, 2903–2909, 2000.

Huang, D. and Liu, Y.: Anovel approach for introducing cloud spatial structure into cloud radiative transfer parameterizations, Environ. Res. Lett., 9, 124 022, 2014.

IPCC: Climate Change 2013: The Physical Science Basis, Cambridge University Press, 2013.

Iwabuchi, H.: Effects of cloud horizontal inhomogeneity on optical remote sensing of cloud parameters, Ph.D. thesis, Center for Atmospheric and Oceanic Studies, Graduate School of Science, Tokohu University, 2000.

Iwabuchi, H.: Efficient Monte Carlo methods for radiative transfer modeling, J. Atmos. Sci., 63, 2324–2339, 2006.

Iwabuchi, H. and Hayasaka, T.: Effects of cloud horizontal inhomogeneity on the optical thickness retrieved from moderate-resolution satellite data, J. Atmos. Sci., 59, 2227–2242, 2002.

Iwabuchi, H. and Kobayashi, H.: Modeling of radiative transfer in cloudy atmospheres and plant canopies using Monte Carlo methods, Tech. Rep., 8, 199 pp., 2008.

Jäkel, E., Wendisch, M., and Mayer, B.: Influence of spatial heterogeneity of local surface albedo on the area-averaged surface albedo retrieved from airborne irradiance measurement, Atmos. Meas. Tech., 6, 527–537, 2013.

Key, J. R., Yang, P., Baum, B. A., and Nasiri, S. L.: Parameterization of shortwave ice cloud optical properties for various particle habits, J. Geophys. Res., 107, 4181, 2002.

King, M., Menel, W., Kaufman, Y., Tanre, D., Gao, B.-C., Platnick, S., Ackerman, S., Remer, L., Pincus, R., and Hubanks, P.: Cloud and aerosol properties, precipitable water, and profiles of temperature and water vapor from MODIS, IEEE Trans. Geosci. Remote Sens., 41, 442–458, 2003.

Klingebiel, M., de Lozar, A., Molleker, S., Weigel, R., Roth, A., Schmidt, L., Meyer, J., Ehrlich, A., Neuber, R., Wendisch, M., and Borrmann, S.: Arctic low-level boundary layer clouds: in situ measurements and simulations of mono- and bimodal supercooled droplet size distributions at the top layer of liquid phase clouds, Atmos. Chem. Phys., 15, 617–631, 2015.

Kolmogorov, A.: Die Energiedissipation für lokalisotrope Turbulenz, Dokl. Akad. Nauk SSSR, 32, 16–18, Nachdruck in: H. Goering Hrsg., 1958: Statistische Theorie der Turbulenz., Akademie–Verlag, Berlin, 71–76., 1941.

Krijger, J. M., Tol, P., Istomina, L. G., Schlundt, C., Schrijver, H., and Aben, I.: Improved identification of clouds and ice/snow covered surfaces in SCIAMACHY observations, Atmos. Meas. Technol., 4, 2213–2224, 2011.

Kristjansson, J., Edwards, J., and Mitchell, D.: Impact of a new scheme for optical properties of ice crystals on climate of two GCMs, J. Geophys. Res., 105, 10 063–10 079, 2000.

Lindsay, R. W. and Rothrock, D. A.: Arctic Sea-ice Albedo From AVHRR, J. Climate, 7, 1737–1749, 1994.

Liou, K.-N.: Influence of cirrus clouds on weather and climate processes: A global perspective, Mon. Wea. Rev., 114, 1167–1199, 1986.

Loeb, N. and Davies, R.: Observational evidence of plane parallel model biases: Apparent dependence of cloud optical depth on solar zenith angle, J. Geophys. Res., 101, 1621–1634, 1996.

Loeb, N. G., Wielicki, B. A., Doelling, D. R., Smith, G. L., Keyes, D. F., Kato, S., Manalo-Smith, N., and Wong, T.: Toward optimal closure of the earth's top-of-atmosphere radiation budget, Journal of Climate, 22, 748–766, 2009.

Lyapustin, A.: Three-dimensional effects in the remote sensing of surface albedo, IEEE Trans. Geosci. Remote Sens., 39, 254–263, 2001.

Lyapustin, A. and Kaufman, Y.: Role of adjacency effect in the remote sensing of aerosol, J. Geophys. Res., 106, 11 909–11 916, 2001.

Lynch, D., Sassen, K., Starr, D., and Stephens, G., eds.: Cirrus, Oxford University Press, 2002.

Macke, A.: Scattering of light by polyhedral ice crystals, Appl. Opt., 32, 2780–2788, 1993.

Macke, A., Francis, P. N., McFarquar, G. M., and Kinne, S.: The role of ice particle shapes and size distributions in the single scattering properties of cirrus clouds, J. Atmos. Sci., 55, 2.874–2.883, 1998.

Malkus, J. S.: Some results of a trade–cumulus cloud investigation, J. Atmos. Sci., 11, 220–237, 1954.

Malkus, J. S.: On the Maintenance of the Trade Winds, Tellus, 8, 335–350, http://dx.doi.org/10.1111/j.2153-3490.1956.tb01231.x, 1956.

Malkus, J. S.: On the structure of the trade wind moist layer, Pap. Phys. Oceanogr. Meteorol., 12, 1–47, 1958.

Marshak, A., Davis, A., Wiscombe, W., and Cahalan, R.: Radiative smoothing in fractal clouds, J. Geophys. Res., 100, 26 247–26 261, 1995.

Marshak, A., Davis, A., Cahalan, R., and Wiscombe, W.: Nonlocal independent pixel approximation: Direct and inverse problems, IEEE Trans. Geosci. Remote Sens., 36, 192–204, 1998.

Marshak, A., Wen, G., Coakley, J. A., Remer, L. A., Loeb, N. G., and Cahalan, R. F.:
  A simple model for the cloud adjacency effect and the apparent blueing of aerosols near
  clouds, J. Geophys. Res., 113, D14S17, 2008.

Matsumoto, T., Russell, P., Mina, C., van Ark, W., and Banta, V.: Airborne tracking
  sunphotometer, J. Atmos. Oceanic Technol., 4, 336–339, 1987.

Mayer: Book Review: Barry, R.G., The Late R. Chorley: Atmosphere, Weather and Climate.
  Eighth Edition., Meteor. Z., 14, 79–80, 2005.

Mayer, B. and Kylling, A.: Technical note: The *libRadtran* software package for radiative
  transfer calculations - description and examples of use, Atmos. Chem. Phys., 5, 1855–1877,
  2005.

McBride, P. J., Schmidt, K. S., Pilewskie, P., Kittelman, A. S., and Wolfe, D. E.: A spec-
  tral method for retrieving cloud optical thickness and effective radius from surface-based
  transmittance measurements, Atmos. Chem. Phys., 11, 7235–7252, 2011.

McFarlane, S. A. and Marchand, R. T.: Analysis of ice crystal habits derived from MISR
  and MODIS observations over the ARM Southern Great Plains site, J. Geophys. Res., 113,
  D07 209, 2008.

Mie, G.: Beiträge zur Optik trüber Medien, speziell kolloidaler Metallösungen, Annalen der
  Physik, Vierte Folge, 25, 377–445, 1908.

Nakajima, T. and King, M.: Determination of the optical thickness and effective particle
  radius of clouds from reflected solar radiation measurements. Part I: Theory, J. Atmos.
  Sci., 47, 1878–1893, 1990.

Oreopoulos, L. and Cahalan, R. F.: Cloud Inhomogeneity from MODIS, J. Climate, 18,
  5110–5124, 2005.

Oreopoulos, L., Cahalan, R., Marshak, A., and Wen, G.: A new normalized difference cloud
  retrieval technique applied to Landsat radiances over the Oklahoma ARM site, J. Appl.
  Meteorol., 39, 2305–2321, 2000.

Petty, G.: A First Course in Atmospheric Radiation, 2nd Edition, Sundog Publishing, Madi-
  son, Wisconsin, 2006.

Pierluissi, J. and Peng, G.-S.: New molecular transmission band models for LOWTRAN,
  Opt. Eng., 24, 541–547, 1985.

Pilewskie, P., Pommier, J., Bergstrom, R., Gore, W., Howard, S., Rabbette, M., Schmid, B.,
  Hobbs, P. V., and Tsay, S. C.: Solar spectral radiative forcing during the Southern African
  Regional Science Initiative, J. Geophys. Res., 108, doi:10.1029/2002JD002 411, 2003.

Platnick, S.: Approximations for horizontal photon transport in cloud remote sensing prob-
  lems, J. Quant. Spectrosc. Radiat. Transfer, 68, 75–99, 2001.

Platnick, S., King, M., Ackerman, S., Menzel, W., Baum, B., Riedi, J., and Frey, R.: The MODIS cloud products: Algorithms and examples from TERRA, IEEE Trans. Geosci. Remote Sens., 41, 459–473, 2003.

Platnick, S., King, M. D., Wind, B., and Gray, M.: An initial analysis of pixel-level uncertainty in global MODIS cloud optical thickness and effective particle size retrievals, Proc. SPIE, 30, 5652, 2004.

Ricchiazzi, P. and Gautier, C.: Investigation of the effect of surface heterogeneity and topography on the radiation environment of Palmer Station, Antarctica, with a hybrid 3-D radiative transfer model, J. Geophys. Res., 103, 6161–6178, 1998.

Rossow, W. and Schiffer, R.: Advances in understanding clouds from ISCCP, Bull. Amer. Meteorol. Soc., 80, 2261–2287, 1999.

Rothrock, D. A. and Thorndike, A. S.: Measuring the sea ice floe size distribution, J. Geophys. Res., 89, 6477–6486, 1984.

Sassen, K. and Benson, S.: A midlatitude cirrus cloud climatology from the facility for atmospheric remote sensing. Part II: Microphysical properties derived from lidar depolarization, J. Atmos. Sci., 58, 2102–2112, 2001.

Sassen, K. and Campbell, J.: A midlatitude cirrus cloud climatology from the facility for atmospheric remote sensing. Part I: Macrophysical and synoptic parameters, J. Atmos. Sci., 58, 481–496, 2001.

Sassen, K. and Comstock, J.: A midlatitude cirrus cloud climatology from the facility for atmospheric remote sensing. Part III: Radiative properties, J. Atmos. Sci., 58, 2113–2127, 2001.

Schäfer, M., Bierwirth, E., Ehrlich, A., Heyner, F., and Wendisch, M.: Retrieval of cirrus optical thickness and assessment of ice crystal shape from ground-based imaging spectrometry, Atmos. Meas. Tech., 6, 1855–1868, 2013.

Schäfer, M., Bierwirth, E., Ehrlich, A., Jäkel, E., and Wendisch, M.: Airborne observations and simulations of three-dimensional radiative interactions between Arctic boundary layer clouds and and ice floes, Atmos. Chem. Phys., 15, 8147–8163, 2015.

Schmidt, K. S., Venema, V., Di Giuseppe, F., Scheirer, R., Wendisch, M., and Pilewskie, P.: Reproducing cloud microphysical and irradiance measurements using three 3D cloud generators, Quart. J. Roy. Meteor. Soc., 133, 765–780, 2007.

Schroeder, M.: Multiple scattering and absorption of solar radiation in the presence of three-dimensional cloud fields, Ph.D. thesis, Fachbereich Geowissenschaften der Freien Universität Berlin, 2004.

Shettle, E.: Comments on the use of LOWTRAN in transmission calculations for sites with the ground elevated relative to sea level, Appl. Opt., 28, 1451–1452, 1989.

Shonk, J. K. P. and Hogan, R. J.: Tripleclouds: an efficient method for representing cloud inhomogeneity in 1D radiation schemes by using three regions at each height, J. Clim., 21, 2352–2370, 2008.

Shonk, J. K. P., Hogan, R. J., and Manners, J.: Impact of improved representation of horizontal and vertical cloud structure in a climate model, J. Clim., 38, 2365–2376, 2011.

Shupe, M. D., Walden, V. P., Eloranta, E., Uttal, T., Campbell, J., Starkweather, S. M., and Shiobara, M.: Clouds at Arctic atmospheric observatories. Part I: Occurrence and macrophysical properties, J. Appl. Meteorol. Clim., 50, 626–644, 2011.

Siebert, H., Bethke, J., Bierwirth, E., Conrath, T., Dieckmann, K., Ditas, F., Ehrlich, A., Farrell, D., Hartmann, S., Izaguirre, M. A., Katzwinkel, J., Nuijens, L., Roberts, G., Schäfer, M., Shaw, R. A., Schmeissner, T., Serikov, I., Stevens, B., Stratmann, F., Wehner, B., Wendisch, M., Werner, F., and Wex, H.: The fine–scale structure of the trade wind cumuli over Barbados – An introduction to the CARRIBA project, Atmos. Chem. Phys., 13, 10 061–10 077, 2013.

Slingo, A.: Sensitivity of the earths radiation budget to changes in low clouds, Nature, 343, 49–51, 1990.

Stachlewska, I. S., Neuber, R., Lapmpert, A., Ritter, C., and Wehrle, G.: AMALi – the Airborne Mobile Aerosol Lidar for Arctic research, Atmos. Chem. Phys., 10, 2947–2963, 2010.

Stephens, G.: Cloud feedbacks in the climate system: A critical review, J. Climate, 18, 237–273, 2005.

Stevens, B., Farrell, D., Hirsch, L., Jansen, F., Nuijens, L., Serikov, I., Brügmann, B., Forde, M., Linne, H., Lonitz, K., and Prospero, J.: Observatory – Anchoring investigations of clouds and circulation on the edge of the ITCZ, Bull. Amer. Meteor. Soc., 2015.

Stocker, T. F., Qin, D., Plattner, G. K., Tignor, M., Allen, S. K., Boschung, J., Nauels, A., Xia, Y., Bex, V., and Midgley, P. M., eds.: Climate Change 2013: The Physical Science Basis. Working Group I Contribution to the Fifth Assessment Report of the Intergovernmental Panel on Climate Change, Cambridge University Press, UK, 2013.

Szczap, F., Isaka, H., Saute, M., and Guillemet, B.: Effective radiative properties of bounded cascade nonabsorbing clouds: Definition of the equivalent homogeneous cloud approximation, J. Geophys. Res., 105, 20 617–20 633, 2000.

Takano, Y. and Liou, K.-N.: Solar radiative transfer in cirrus clouds. Part I: Single-scattering and optical properties of hexagonal ice crystals, J. Atmos. Sci., 46, 1–19, 1989.

Varnai, T. and Marshak, A.: View angle dependence of cloud optical thicknesses retrieved by Moderate Resolution Imaging Spectroradiometer (MODIS), J. Geophys. Res., 112, D06 203, 2007.

Wendisch, M. and Yang, P.: Theory of Atmospheric Radiative Transfer - A Comprehensive Introduction, Wiley-VCH Verlag GmbH & Co. KGaA, Weinheim, Germany, ISBN: 978-3-527-40836-8, 2012.

Wendisch, M., Müller, D., Schell, D., and Heintzenberg, J.: An airborne spectral albedometer with active horizontal stabilization, J. Atmos. Oceanic Technol., 18, 1856–1866, 2001.

Wendisch, M., Pilewskie, P., Jäkel, E., Schmidt, S., Pommier, J., Howard, S., Jonsson, H. H., Guan, H., Schröder, M., and Mayer, B.: Airborne measurements of areal spectral surface albedo over different sea and land surfaces, J. Geophys. Res., 109, D08 203, 2004.

Wendisch, M., Pilewskie, P., Pommier, J., Howard, S., Yang, P., Heymsfield, A. J., Schmitt, C. G., Baumgardner, D., and Mayer, B.: Impact of cirrus crystal shape on solar spectral irradiance: A case study for subtropical cirrus, J. Geophys. Res., 110, D03 202, 2005.

Wendisch, M., Yang, P., and Pilewskie, P.: Effects of ice crystal habit on thermal infrared radiative properties and forcing of cirrus, J. Geophys. Res., 112, D03 202, 2007.

Wendisch, M., Yang, P., and Ehrlich, A.: Amplified climate changes in the Arctic: Role of clouds and atmospheric radiation, vol. 132, chap. 1, pp. 1–34, Sitzungsberichte der Sächsischen Akademie der Wissenschaften zu Leipzig, Mathematisch-Naturwissenschaftliche Klasse, S. Hirzel Verlag, 2013.

Wendisch, M., Poschl, U., Andreae, M., Machado, L., Albrecht, R., Schlager, H., Rosenfeld, D., Martin, S., Abdelmonem, A., Afchine, A., Araujo, A., Artaxo, P., Aufmhoff, H., Barbosa, H., Borrmann, S., Braga, R., Buchholz, B., Cecchini, M. Costa, A., Curtius, J., Dollner, M., Dorf, M., Dreiling, V., Ebert, V., Ehrlich, A., Ewald, F., Fisch, G., Fix, A., Frank, F., Fuetterer, D., Heckl, C., Heidelberg, F., Hueneke, T., Jaekel, E., Jaervinen, E., Jurkat, T., Kanter, S., Kaestner, U., Kenntner, M., Kesselmeier, J., Klimach, T., Knecht, M., Kohl, R., Koelling, T., Kraemer, M., Krueger, M., Krisna, T., Lavric, J., Longo, K., Mahnke, C., Manzi, A., Mayer, B., Mertes, S., Minikin, A., Molleker, S., Muench, S., Nillius, B., Pfeilsticker, K., Poehlker, C., Roiger, A., Rose, D., Rosenow, D., Sauer, D., Schnaiter, M., Schneider, J., Schulz, C., de Souza, R., Spanu, A., Stock, P., Vila, D., Voigt, C., Walser, A., Walter, D., Weigel, R., Weinzierl, B., Werner, F., Yamasoe, M., Ziereis, H., Zinner, T., and Zoeger, M.: The ACRIDICON-CHUVA campaign: Studying tropical deep convective clouds and precipitation over Amazonia using the new German research aircraft HALO, Bull. Amer. Meteor. Soc., in press, 2016.

Werner, F., Siebert, H., Pilewskie, P., Schmeissner, T., Shaw, R. A., and Wendisch, M.: New airborne retrieval approach for trade wind cumulus properties under overlying cirrus, J. Geophys. Res.-Atmos., 118, 3634–3649, `http://dx.doi.org/10.1002/jgrd.50334`, 2013.

Werner, F., Ditas, F., Siebert, H., Simmel, M., Wehner, B., Pilewskie, P., Schmeissner, T., Shaw, R. A., Hartmann, S., Wex, H., Roberts, G. C., and Wendisch, M.: Twomey effect observed from collocated microphysical and remote sensing measurements over shallow cumulus, J. Geophys. Res., 119, 1534–1545, `http://dx.doi.org/10.1002/2013JD020131`, 2014.

Wood, R. and Hartmann, D. L.: Spatial variability of liquid water path in marine low cloud: The importance of mesoscale cellular convection., J. Climate, 19, 1748–1764, 2006.

Yang, H. Y., Dobbie, S., Herbert, R., Connolly, P., Gallagher, M., Ghosh, S., Al-Jumur, S. M. R. K., and Clayton, J.: The effect of oberserved vertical structure, habits, and size distribution on the solar radiative properties and cloud evolution of cirrus clouds, Quart. J. R. Met. Soc., 138, 1221–1232, 2012.

Yang, P. and Liou, K.: Light scattering by nonspherical particles: Theory, measurements, and applications, chap. Finite difference time domain method for light scattering by non-spherical and inhomogeneous particles, Academic Press, 2000.

Yang, P., Liou, K. N., Wyser, K., and Mitchell, D.: Parameterization of the scattering and absorption properties of individual ice crystals, J. Geophys. Res., 105, 4.699–4.718, 2000.

Yang, P., Wei, H. L., Huang, H. L., Baum, B. A., Hu, Y. X., Kattawar, G. W., Mishchenko, M. I., and Fu, Q.: Scattering and absorption property database for nonspherical ice particles in the near- through far-infrared spectral region, Appl. Opt., 44, 5512–5523, 2005.

Yang, P., Zhang, L., Hong, G., Nasiri, S. L., Baum, B. A., Huang, H. L., King, M. D., and Platnick, S.: Differences between collection 4 and 5 MODIS ice cloud optical/microphysical products and their impact on radiative forcing simulations, IEEE Trans. Geosci. Remote Sens., 45, 2886–2899, 2007.

Yang, P., Bi, L., Baum, B. A., Liou, K. N., Kattawar, G. W., Mishchenko, M. I., and Cole, B.: Spectrall consistent scatterin, absorption, and polarization properties of atmospheric ice crystals at wavelengths from 0.2 to 100 μm, J. Atmos. Sci., 70, 330–347, 2013.

Yi, B., Yang, P., Baum, B. A., L'Ecuyer, T., Oreopoulos, L., Mlawer, E. J., Heymsfield, A. J., and Liou, K.-N.: Influence of ice particle surface roughening on the global cloud radiative effect, J. Atmos. Sci., 70, 2794–2807, 2013.

Zinner, T., Mannstein, H., and Tafferner, A.: Cb-TRAM: Tracking and monitoring severe convection from onset over rapid development to mature phase using multi-channel Meteosat-8 SEVIRI data, Meteorology and Applied Physics, submitted, 2006.

Zinner, T., Wind, G., Platnick, S., and Ackerman, A. S.: Testing remote sensing on artificial observations: Impact of drizzle and 3-D cloud structure on effective radius retrievals, Atmos. Chem. Phys., 10, 9535–9549, 2010.

Zuidema, P. and Evans, K.: On the validity of the independent pixel approximation for boundary layer clouds observed during ASTEX, J. Geophys. Res., 103, 6059–6074, 1998.

List of Greek Symbols

α	rad or $^\circ$	Angle between Particular Applied Directions
$\alpha_{\lambda,\mathrm{surf}}$	-	Spectral Surface Albedo
β	rad or $^\circ$	Diffraction Angle
β_i	rad or $^\circ$	Viewing Zenith of Spatial Pixel i
β_l	-	Large-Scale Slope
β_m	-	Middle-Scale Slope
β_s	-	Small-Scale Slope
γ_λ	-	Spectral Reflectivity
$\bar{\gamma}_\lambda$	-	Mean Spectral Reflectivity
$\gamma_{\lambda,\mathrm{ice}}$	-	Spectral Reflectivity Above Bright Sea Ice
$\gamma_{\lambda,\mathrm{water}}$	-	Spectral Reflectivity Above Dark Ocean Water
$\gamma_{\lambda,\mathrm{thresh}}$	-	Spectral Reflectivity Threshold
ϑ	rad or $^\circ$	Scattering Angle
θ	rad or $^\circ$	Atmospheric Zenith Angle
θ_0	rad or $^\circ$	Solar Zenith Angle
λ	m	Wavelength
μ	-	Zenith Distance
μ_0	-	Solar Zenith Distance
μ'	-	Cosine of Direction of Incident Radiation
ξ_τ	m	De–Correlation Length
$\xi_{\tau,\mathrm{L}}$	m	Large-Scale Break
$\xi_{\tau,\mathrm{s}}$	m	Small-Scale Break
ρ_i	g m^{-3}	Density of Solid Ice
ρ_λ	-	Spectral Cloud Albedo
ρ_τ	-	Inhomogeneity Parameter
ρ_w	g m^{-3}	Density of Liquid Water
σ	variable	Standard Deviation
τ	-	Cloud Optical Thickness
τ_aer	-	Aerosol Optical Thickness
τ_ci	-	Cirrus Optical Thickness
$\bar{\tau}_\mathrm{ci}$	-	Mean Cirrus Optical Thickness
$\tau_\mathrm{ci,BM}$	-	Cirrus Optical Thickness of Benchmark Retrieval
τ_st	-	Optical Thickness of Arctic Stratus
$\bar{\tau}_\mathrm{st}$	-	Mean Optical Thickness of Arctic Stratus
$\tau_\mathrm{st,BM}$	-	Optical Thickness of Arctic Stratus of Benchmark Retrieval
φ	rad or $^\circ$	Atmospheric Azimuth Angle

φ_0	rad or °	Solar Azimuth Angle
φ'	rad or °	Azimuth Angle of Incident Radiation
φ_{sen}	rad or °	Sensor Azimuth Angle
Φ_λ	$\mathrm{J\,s^{-1}\,nm^{-1}}$	Spectral Radiant Energy Flux
Φ_{abs}	$\mathrm{J\,s^{-1}\,nm^{-1}}$	Absorbed Radiant Energy Flux
Φ_{ext}	$\mathrm{J\,s^{-1}\,nm^{-1}}$	Extinguished Radiant Energy Flux
Φ_{sca}	$\mathrm{J\,s^{-1}\,nm^{-1}}$	Scattered Radiant Energy Flux
χ_τ	-	Inhomogeneity Parameter
$\tilde{\omega}$	-	Single–Scattering Albedo
Ω	sr	Solid Angle

List of Latin Symbols

A_D	m^2	Projected Area of an Ice Crystal
$A_{\Delta h}$	-	Fit Parameter
A_i	m^2	Ice Floe Area of Scenario i
$B_{\Delta h}$	m	Fit Parameter
b_ext	m^{-1}	Spectral Volumetric Extinction Coefficient
b_sca	m^{-1}	Spectral Volumetric Scattering Coefficient
C	m	Fit Parameter
C_abs	m^2	Absorption Cross Section
C_ext	m^2	Extinction Cross Section
C_sca	m^2	Scattering Cross Section
$\text{d}^2 A$	m^2	Infinitesimal Area Element
$\text{d}^2 \Omega$	sr	Differential Solid Angle
d	m	Groove Spacing
D	m	Diameter of Cloud Particle
ΔL	m	Critical Horizontal Distance to the Ice Edge
ΔL_HPT	m	Critical Horizontal Distance to the Ice Edge related to the Horizontal Photon Transport
$E(k_\text{x,y})$	-	Power Spectral Density
E_rn	-	Power Spectral Density with Reduced Noise Characteristics
E_rad	J	Radiant Energy
f	-	Function
f_c	W m^{-2} nm^{-1} sr^{-1}	Absolute Calibration Factors from Integrating Sphere
F_λ	W m^{-2} nm^{-1}	Spectral Irradiance
F_inc	W m^{-2} nm^{-1}	Incident Irradiance
$F_\lambda^\downarrow$	W m^{-2} nm^{-1}	Downward Spectral Irradiance
$F_\lambda^\uparrow$	W m^{-2} nm^{-1}	Upward Spectral Irradiance
h_cloud	m	Cloud Base Altitude
I_λ	W m^{-2} nm^{-1} sr^{-1}	Spectral Radiance
$I_\lambda^\downarrow$	W m^{-2} nm^{-1} sr^{-1}	Downward Spectral Radiance
$I_\lambda^\uparrow$	W m^{-2} nm^{-1} sr^{-1}	Upward Spectral Radiance
I_diff	W m^{-2} nm^{-1} sr^{-1}	Diffuse Solar Radiance
I_dir	W m^{-2} nm^{-1} sr^{-1}	Direct Solar Radiance
J_diff	W m^{-2} nm^{-1} sr^{-1}	Diffuse Source Term
J_dir	W m^{-2} nm^{-1} sr^{-1}	Direct Source Term
$k_\text{x,y}$	m^{-1}	Wavenumber
l_i	m	Ice Edge Length of Scenario i

l_{pix}	m	Spatial Pixel Resolution Across Swath Direction
$L_{\mathrm{x,y}}$	-	Lag
m	-	Number of Elements
M	-	Defraction Order
n	-	Number of Elements
$\widehat{n}$	-	Unit Vector
n_{pix}	-	Spatial Pixel Number
$\frac{\mathrm{d}N}{\mathrm{d}D}(D)$	m^{-1}	Number Size Distribution
p	hPa	Mean Surface Pressure
$P_{\tau}(L_{\mathrm{x,y}})$	-	Spatial Auto-Correlation Function
r_{eff}	µm	Effective Radius
r_{floe}	m	Radius of Ice Floe
$R_{\mathrm{3D/IPA}}$	-	Ration between 3D and IPA Simulations
R_{ice}	-	Ration between 3D and IPA Simulations over Sea Ice only
R_{total}	-	Ration between 3D and IPA Simulations over Total Domain
R_{water}	-	Ration between 3D and IPA Simulations over Water only
$\widehat{s}$	-	Direction of Propagation
s	m	Swath
S_{τ}	-	Inhomogeneity Parameter
S_0	$\mathrm{W\,m}^{-2}\,\mathrm{nm}^{-1}$	Extraterrestrial Irradiance
S_{c}		Smear-Corretion Factor
S_{cal}	ADU	Measurement Signal During Calibration
S_{dark}	ADU	Measured Dark Raw Signal
S_{lum}	ADU	Measured Illuminated Raw Signal
S_{meas}	ADU	Raw Measurement Signal
s_{pix}	m	Spatial Pixel Resolution Along Swath Direction
t	s	Time
t_{int}	s	Integration Time
$t_{\mathrm{read-out}}$	s	Read-Out Time
v	$\mathrm{m\,s}^{-1}$	Mean Horizontal Wind
$v_{\mathrm{cloud,\ aircraft}}$	$\mathrm{m\,s}^{-1}$	Velocity of Cloud or Aircraft
V_{D}	m^3	Volume of an Ice Crystal
x	m	Distance
x_i	-	Sampling Frequency
y_i	-	Sampling Frequency
z_{ct}	m	Cloud Top Altitude
z_{surf}	m	Surface Altitude
$\mathcal{F}$	-	Fourier Transform
$\mathcal{P}$	-	Phase Function
$\overrightarrow{CD}$	-	Vector of Incident Radiation between Cloud and Detector
$\overrightarrow{SC}$	-	Vector of Incident Radiation between Sun and Cloud

DFT	-	Discrete Fourier Transform
FOV	rad or °	Field of View
FOV$_{\text{pix}}$	rad or °	Field of View of Single Pixel
FWHM	m	Full Width at Half Maximum
IWC	g m^{-3}	Ice Water Content
LWC	g m^{-3}	Liquid Water Content
SNR	-	Signal to Noise Ratio
RH	%	Relative Humidity

List of Abbrevations

1D	One–dimensional
2D	Two–dimensional
3D	Three–dimensional
AB	Airborne
AC^3	ArctiC Amplification: Climate Relevant Atmospheric and SurfaCe Processes, and Feedback Mechanisms
ACRIDICON	Aerosol, Cloud, Precipitation, and Radiation Interactions and DynamIcs of CONvective Cloud Systems
ADU	Analog Digital Units
AMALi	Airborne Mobile Aerosol LiDAR
AVHRR	Advanced Very High Resolution Radiometer
ARL	Air Resources Laboratory
AWI	Alfred Wegener Institute Helmholtz Centre for Polar and Marine Research
BCO	Barbados Cloud Observatory
CARRIBA	Clouds, Aerosol, Radiation, and tuRbulence in the trade wind regime over BArbados
CASI	Compact Airborne Spectrographic Imager
CCD	Charge-Coupled Device
CHUVA	Cloud processes of tHe main precipitation systems in Brazil: A contribUtion to cloud resolVing modeling and to the GPM
COS	Cloud Overlap Schemes
DFT	Discrete Fourier Transformation
DISORT	DIScrete Ordinate Radiative Transfer Solver
ECMWF	European Centre for Medium-Range Weather Forecasts
FOV	Field Of View
FPS	Frames Per Second
FWHM	Full Width at Half Maximum
GCM	General Circulation Model
GPM	Global Precipitation Measurement
GPS	Global Positioning System
HALO	High Altitude and LOng range research aircraft
HDRF	Hemispherical-Directional Reflectance Function
HEY	Hong, Emde, Yang
HPT	Horizontal Photon Transport
HYSPLIT	HYbrid Single-Particle Lagrangian Integrated Trajectory

INS	Inertial Navigation System
IPA	Independent Pixel Approximation
IPCC	Intergovernmental Panel on Climate Change
IWC	Ice Water Content
LES	Large-Eddy Simulation
libRadtran	library for radiative transfer
LiDAR	Light Detection And Ranging
LIM	Leipzig Institute for Meteorology
LOWTRAN	LOW Resolution TRANsmission Model parametrization
LUT	Lookup Tables
LWC	Liquid Water Content
MAS	MODIS Airborne Simulator
MCARaTS	Monte Carlo Atmospheric Radiative Transfer Solver
MISR	Multiangle Imaging SpectroRadiometer
MODIS	MODerate-Resolution Imaging Spectrometer
NISE	Near Real-Time Ice and Snow Extent
NOAA	National Oceanic and Atmospheric Administration
OPAC	Optical Properties of Aerosols and Clouds
RACEPAC	Radiation-Aerosol-Cloud ExPeriment in the Arctic Circle
RGB	red, green, blue
RH	Relative Humidity
RTE	Radiative Transfer Equation
SBDART	Santa Barbara DISORT Atmospheric Radiative Transfer
SID	Small Ice Detector
SMART	Spectral Modular Airborne Radiation measurement sysTem
SNR	Signal–To–Noise Ratio
SoRPIC	Solar Radiation and Phase discrimination of ArctIc Clouds
specMACS	spectrometer of the Munich Aerosol Cloud Scanner
SSFR	Solar Spectral Flux Radiometers
UTC	Coordinated Universal Time
VERDI	VERtical Distribution of Ice in Arctic clouds

List of Figures

List of Tables

Acknowledgements

Curriculum Vitae

Name	Michael Schäfer
Date of birth	27 February 1985
Place of birth	Schönebeck/ Elbe, Sachsen–Anhalt
Citizenship	German
Current address	Gorkistr. 120
	04347 Leipzig, Germany
	Email: micha.meteorologe (at) web.de

Education

1991 – 1995	Basic Primary School, Biere
1995 – 1997	Secondary School, Welsleben
1997 – 2004	Dr.–Tolberg–Grammar School, Schönebeck/ Elbe
	Degree: Abitur
10/2005 – 02/2011	Meteorology at the University of Leipzig, Germany
	Degree: Diploma
01/2012 – present	PhD student at the University of Leipzig, Germany

Employments

09/2003–09/2004	Assistant employee at Erdgas Mittelsachsen GmbH, Schönebeck/ Elbe
10/2004–06/2005	Basic military service
12/2008–03/2011	Student assistant at Leibniz Institute for Tropospheric Research, Leipzig, Germany
04/2011–12/2011	Research assistant at Leibniz Institute for Tropospheric Research, Leipzig, Germany
01/2012 – present	Scientific employee at University of Leipzig, Germany